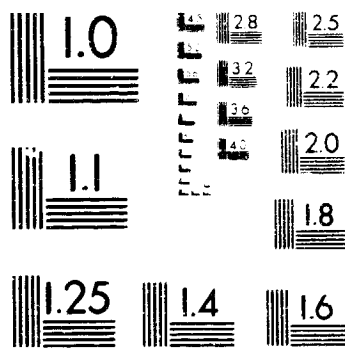# 1 OF 2

N94-35498 UNCLAS

MICROCOPY RESOLUTION TEST CHART
NATIONAL BUREAU OF STANDARDS
STANDARD REFERENCE MATERIAL 1010a
ANSI and ISO TEST CHART No. 2

DEVELOPMENT AND APPLICATION OF

COMPUTATIONAL AEROTHERMODYNAMICS FLOWFIELD COMPUTER CODES

Ethiraj Venkatapathy

Eloret Institute
3788 Fabian Way
Palo Alto, CA 94303

NASA

National Aeronautics and
Space Administration

Ames Research Center
Moffett Field, California 94035

DEVELOPMENT AND APPLICATION OF
COMPUTATIONAL AEROTHERMODYNAMICS FLOWFIELD COMPUTER CODES

Ethiraj Venkatapathy

NASA

1. Report No.	2. Government Accession No.	3. Recipient's Catalog No.
4. Title and Subtitle Development and Application of Computational Aerothermodynamics Flowfield Computer Codes		**5. Report Date** 14 July 1994
		6. Performing Organization Code
7. Author(s) Ethiraj Venkatapathy		**8. Performing Organization Report No.**
		10. Work Unit No
9. Performing Organization Name and Address Eloret Institute 3788 Fabian Way Palo Alto CA 94303		**11. Contract or Grant No.** NCC2-420
		13. Type of Report and Period Covered 9/1/86 to 1/31/94
12. Sponsoring Agency Name and Address National Aeronautics and Space Administration, Washington, D.C. 20456		**14. Sponsoring Agency Code**

15. Supplementary Notes

Point of Contact: Dr. Ethiraj Venkatapathy
c/o 230-2, NASA Ames Research Center, Moffett Field, CA 94035

16. Abstract

Research was performed in the area of computational modeling and application of hypersonic, high-enthalpy, thermo-chemical nonequilibrium flow (Aerothermodynamics) problems. A number of computational fluid dynamic (CFD) codes were developed and applied to simulate high altitude rocket-plume, the Aeroassist Flight Experiment (AFE), hypersonic base flow for planetary probes, the single-expansion ramp model (SERN) connected with the National Aerospace Plane, hypersonic drag devices, hypersonic ramp flows, ballistic range models, shock tunnel facility nozzles, transient and steady flows in the shock tunnel facility, arc-jet flows, thermochemical nonequilibrium flows around simple and complex bodies, axisymmetric ionized flows of interest to re-entry, unsteady shock induced combustion phenomena, high enthalpy pulsed facility simulations, and unsteady shock boundary layer interactions in shock tunnels. Computational modeling involved developing appropriate numerical schemes for the flows on interest and developing, applying, and validating appropriate thermochemical processes. As part of improving the accuracy of the numerical predictions, adaptive grid algorithms were explored, and a user-friendly, self-adaptive code (SAGE) was developed. Aerothermodynamic flows of interest included energy transfer due to strong radiation, and a significant level of effort was spent in developing computational codes for calculating radiation and radiation modeling. In addition, computational tools were developed and applied to predict the radiative heat flux and spectra that reach the model surface.

17. Key Words (Suggested by Author(s)) Arc-jet flows Shock layer radiation SAGE code Nonequilibrium thermochemical flow	**18. Distribution Statement** Unclassified, Unlimited

19. Security Classif. (of this report) Unclassified	**20. Security Classif. (of this page)** Unclassified	**21. No. of Pages**	**22. Price**

DEVELOPMENT AND APPLICATION OF COMPUTATIONAL AEROTHERMODYNAMICS FLOWFIELD COMPUTER CODES

Submitted to

National Aeronautics and Space Administration
Ames Research Center
Moffett Field, California 94035

Aerothermodynamics Branch
Dr. Thomas A. Edwards, Chief

Thermosciences Division
Dr. James O. Arnold, Chief
Dr. George S. Deiwert, Technical Officer

Prepared by

ELORET INSTITUTE
3788 Fabian Way
Palo Alto, CA 94303
Phone: 415 493-4764
Telefax: 415-424-9876

Dr. Klaus Heinemann, President and Grant Administrator
Dr. Ethiraj Venkatapathy, Principal Investigator

14 July, 1994

The following scientific papers resulted from work under Cooperative Agreement NCC2-420. They were discussed in, and appended to, prior periodic reports and are therefore not appended here.

(1) W.J. Feiereisen and E. Venkatapathy, "*Computations of Ideal and Real Gas High Altitude Plume Flows,*" AIAA-Paper 88-2636.

(2) E. Venkatapathy and W.J. Feiereisen, "*3-D Plume Flow Computations with an Upwind Solver,*" AIAA-Paper 88-3158.

(3) E. Venkatapathy, W.J. Feiereisen, and S. Obayashi, "*Computational Studies of Hard-Body and 3-D Effects in Plume Flows,*" AIAA-Paper 89-0129.

(4) S.M. Ruffin, E. Venkatapathy, E.R. Keener, and N. Nagaraj, "*Computational Design Aspects of a NASP Nozzle/Afterbody Experiment,*" AIAA-Paper 89-0446.

(5) E. Venkatapathy, S.M. Ruffin, S.-H. Lee, G.S. Deiwert, and W. Feiereisen, "*Development and Applications of a Nozzle/ Afterbody Flow Solver,*" NASP report, 10/1989.

(6) G.S. Deiwert, E. Venkatapathy, C. Davies, J. Djomehri, and K. Abrahamson, "*Application of a Self-Adaptive Grid Method to Complex Flows,*" NASA Technical Memorandum 102223.

(7) C. Davies and E. Venkatapathy, "*A Simplified Self-Adaptive Grid Method, SAGE,*" NASA Technical Memorandum 102198.

(8) S.-H. Lee, D.W. Bogdanoff, J.A. Cavolowsky, and Ch. Park, "*Nonequilibrium H_2-Air Reactions in Shock Tunnel Nozzle,*" AIAA-Paper 90-1751.

(9) T. Gökcen and Ch. Park, "*The Coupling of Radiative Transfer to Quasi 1-D Flows with Thermochemical Nonequilibrium,*" AIAA-Paper 91-0570.

(10) E. Venkatapathy and W. Feiereisen, "*Computational Analysis of Plume Induced Separation,*" AIAA-Paper 91-0711.

(11) D. S. Babikian, "*Predicting the Radiation from the Wake of the Aeroassisted Flight Experiment Vehicle,*" presented at the AIAA 30th Aerospace Sciences Meeting, Reno, 1/1992.

(12) P.L. Führer, D.K. Edwards, and D.S. Babikian, "*Computational Methodology for Radiation Heat Transfer in the Flowfield of an AOTV,*" AIAA-Paper 91-1407.

(13) A.W. Strawa, Ch. Park, W.C. Davy, R.A. Craig, D.S. Babikian, D.K. Prabhu, and E. Venkatapathy, "*Radiometric Investigation of the Wake Flow of the Forthcoming Aeroassist Flight Experiment,*" AIAA-Paper 91-1408.

(14) L.A. Yates and E. Venkatapathy, *"Trim Angle Measurements in Fre-Flight Facilities,"* AIAA-Paper 91-1632.

(15) S. Tokarcik, E. Venkatapathy, G. Candler, and G. Palmer, *"Computational Flow Predictions for Hypersonic Drag Devices,"* AIAA-Paper 91-3303.

(16) C.B. Davies and E. Venkatapathy, *"Application of a Solution Adaptive Grid Scheme, SAGE, to Complex 3-D Flows,"* AIAA-Paper 91-1594-CP.

(17) T. Gökcen, *"The coupling of Radiation to Blunt Body Flows in Thermochemical Nonequilibrium,"* presented at 23rd AIAA Plasma Dynamics and Lasers Conf., Nashville, 7/1992.

(18) S.-H. Lee, M. Loomis, and Ch. Park, *"Thermochemical Relaxation in High Enthalpy Nozzle Flows,"* presented at AIAA 17th Ground Testing Conf., Nashville, 7/1992.

(19) G. Palmer and E. Venkatapathy, *"Effective Treatments of the Singular Line Boundary Problem for Three-Dimensional Grids,"* AIAA-Paper 92-0545.

(20) S.M. Ruffin, E. Venkatapathy, S.-H. Lee, E.R. Keener, and F.S. Spaid, *"Single Expansion Ramp Nozzle Simulations,"* AIAA, 1992.

(21) I.D. Boyd and T. Gökcen, *"Evaluation of Thermochemical Models for Particle and Continuum Simulations of Hypersonic Flow,"* AIAA 27th Thermophysics Conf., Nashville, TN, 1992, AIAA-paper 92-2971, and Journal of Thermophysics and Heat Transfer 7,3 (1993) 406.

(22) J.-L. Cambier, S. Tokarcik, and D.K. Prabhu, *"Numerical Simulations of Unsteady Flow in a Hypersonic Shock Tunnel Facility,"* AIAA 27th Thermophysics Conference, Nashville, TN, 1992, AIAA-Paper 92-4029.

(23) I.D. Boyd and E.E. Whiting, *"Decoupled Predictions of Radiative Heating in Air Using a Particle Simulation Method,"* AIAA 23rd Plasmadynamics & Lasers Conf., Nashville, TN, 1992, AIAA-Paper 92-2954.

(24) G. Wilson, *"Time-Dependent Quasi-One-Dimensional Simulations of High-Enthalpy Pulse Facilities,",* AIAA 4th Int. Aerospace Planes Conf., Orlando, FL, 1992, AIAA-Paper 92-5096.

(25) S.-H. Lee and Chul Park, *"Validation of Three-Temperature Nozzle Flow Code NOZ3T,"* submitted for publication.

(26) S. Tokarcik, E. Venkatapathy, and M. Tauber, *"Computational Study of a Lunar Return Aerobrake Concept,"* Abstract for 31st Aerospace Sciences Meeting, Reno, NV. 1993.

(27) S. (Tokarcik) Polsky, E. Venkatapathy, and M. Tauber, *"Computational Study of a Lunar Return Aerobrake Concept,"* 31st Aerospace Sciences Meeting, Reno, NV. 1993 AIAA-Paper 93-0037.

(28) G. Wilson, S.P. Sharma, and W.D. Gillespie, *"Time-Dependent Simulations of Reflected-Shock/Boundary Layer Interaction,"* 31st Aerospace Sciences Meeting, Reno, NV. 1993 AIAA-Paper 93-0480.

(29) S. Tokarcik and J.-L. Cambier, *"Numerical Study of the Transient Flow in the Driven Tube and the Nozzle Section of a Shock Tunnel,"* AIAA Paper 93-2018.

(30) G.J. Wilson and M.A. Sussman, *"Computation of Unsteady Shock-Induced Combustion Using Logarithmic Species Conservation Equatior ,"* AIAA Journal Vol.31, 1993, 294.

(31) S. Tokarcik and E. Venkatapathy, *"Hypersonic Aerodynamic Decelerators Design Using CFD: Part II - Turbulent Computations,"* AIAA Paper 93-1230.

(32) D.A. Levin, G.V. Candler, R.J. Collins, C.L. Howlett, E.E. Whiting and Ch. Park, *"Comparison of Theory with Atomic Oxygen 1304 A Radiation Data from the Bow Shock Ultraviolet 2 Rocket Flight,"* Abstract for 28th AIAA Thermophysics Conf., 1993.

(33) N.K.J.M. Gopaul, D. Babikian, and Ch. Park, *"Measurement and Analysis of NO Radiation in an Arc-Jet Flow,"* Abstract for 28th AIAA Thermophysics Conf., 1993.

The following papers were prepared since the last submittal of a periodic report on this Cooperative Agreement, and copies are attached to this report:

(34) G. Palumbo, R. Craig, and A. Carrasco, *"Spectral Measurements of Shock Layer Radiation in an Arc-Jet Wind Tunnel,"* ISA 1993, Paper #93-145.

(35) C.R. Bobba, R.K. Rout, J.L. Younghans, and E. Venkatapathy, *"Application and Validation of the FL3D Solver to Propulsion Flows,"* AIAA Paper 94-0656 (Reno, 1/94).

(36) C.R. Bobba, R.K. Rowe, R.K. Rout, and E. Venkatapathy, *"Computational Analysis of a 2DCD Nozzxle Flow with the FL3D Solver,"* AIAA Paper 94-0019 (Reno, 1/94)

(37) G.J. Wilson, S.P. Sharma, and W.D. Gillespie, *"Time-Dependent Simulation of Reflected-Shock/Boundary Layer Interaction in Shock Tubes,"* paper presented at 19th Int. Symp. on Shock Waves, Marseille, France, 7/93.

(38) D.J. Bamford, A. O'Keefe, A.W. Strawa, D.A. Steward, and D.S. Babikian, *"Characterization of Arc-Jet Flows Using Laser-Induced Fluorescence,"* presented at the AIAA Aerospace Sciences Meeting, Reno, 1/194.

(39) D.S. Babikian, R.A. Craig, G. Palumbo, and G. Palmer, *"Measured and Calculated Spectral Radiation from a Blunt Body Shock Layer in an Arc-Jet Wind Tunnel,"* presented at the AIAA Aerospace Sciences Meeting, Reno, 1/194.

(40) D.S. Babikian and G.A. Raiche, *"Spetroscopic Investigation of Thermochemical Processes in a Blunt Body Shock Layer in an Arc-Jet,"* prepared for AIAA/ASME 6th Joint Thermophysics and Heat Transfer Conf., Colorado Springs, 6/1994.

(41) D.S. Babikian, N.K.J.M. Gopaul, and Ch. Park, *"Measurement and Analysis of Nitric Oxide Radiation in an Arc-Jet Flow,"* AIAA-Paper 93-2800 (Orlando, 7/1993).

(42) J.-L. Cambier and D.K. Prabhu, *"Numerical Simulations of Nonequilibrium Shock Layers with Highly Efficient Implicit Schemes,"* AIAA-Paper 92-2973 (Nashvillem 7/1992)

(42) T. Gökcen, *"Computation of Nonequilibrium Viscous Flows in Arc-Jet Wind Tunnel Nozzles,"* prepared for 32nd AIAA Aerospace Sciences Meeting, Reno, 1/1994.

Spectral Measurements of Shock Layer Radiation in an Arc-Jet Wind Tunnel

Giuseppe Palumbo,[1] Roger Craig[2] and Armando Carrasco[3]

KEY WORDS

Spectroscopic Analyzers, Optical Instrumentation, Radiation Instrumentation, Ultraviolet (UV) Instrumentation

ABSTRACT

Measurements were made of the radiating gas cap of a blunt body in an NASA-Ames 20 MW arc-jet wind tunnel. The test gas was air. Spectra of the flux incident on a small aperture centered at the stagnation region were obtained. A helium-cooled, magnesium fluoride window transmitted flux into an evacuated collimating system that focused the aperture onto the entrance slit of a spectrometer. Data were obtained with films and by photomultipliers. The range covered was 120 nm to 1000 nm and the resolution was 0.05 nm to 0.5 nm. This paper presents preliminary results from the experiment. Representative spectral records from 200 nm to 1000 nm are shown. The spectra show the atomic lines from oxygen and nitrogen in the IR, as well as the molecular systems of NO, N_2, N_2^+, and CN. Copper, as a contaminant, and carbon are tentatively identified. Planned subsequent laboratory work will result in calibration of spectral sensitivity and refined wavelength determinations.

---

[1] Eloret Institute .
Work performed under NASA Cooperative Agreement NCC2-653
1176 Maraschino Drive
Santa Clara, CA 94057

[2] MCAT Institute
Work performed under NASA Cooperative Agreement NCC2-762
NASA Ames Research Center
Moffett Field, CA 94035

[3] Thermo-Physics Facilities Branch
NASA Ames Research Center
Moffett Field, CA 94035

INTRODUCTION

Arc-jet wind tunnels, simulating conditions of high speed flight, are likely to be more and more important for aerospace research in the future. Computational modelling replacing the work of low speed wind tunnels, wherein real gas effects do not dominate, is becoming a reality. However, high speed flights, such as earth entry from a space mission (low earth orbit, LEO, or further), involves flowfield gases which are not in thermochemical equilibrium (references 1 and 2). This can include important levels of transport of radiative energy (reference 3). At present we cannot accurately predict the environmental conditions surrounding these spacecraft. Figure 1 shows flight regimes experienced for the entries of the Shuttle, Apollo and a proposed Aeroassisted Space Transfer Vehicle (ASTV). An ASTV is a conceptual vehicle which utilizes aerodynamic forces to decelerate and alter orbit parameters to rendezvous with the Shuttle or a space station (reference 1). The design of future, highly efficient heat-shields (i. e., not overdesigned) for these vehicles, and others, requires the capability of making accurate heating predictions. This fact is acknowledged by the inception of the Aeroassist Flight Experiment (reference 4). This experiment utilized a vehicle designed to be deployed and recovered by the Shuttle. It was to fly a trajectory which simulated an ASTV maneuver from geosynchronous earth orbit (GEO) to LEO for rendezvous with the Shuttle or a space station. The objective was to gather a data base for development of the ASTV and other advanced space transportation systems. The program was recently canceled due to funding limitations. Although the activity was cancelled the technical requirement remains.

Real gas computational models are being developed (reference 5) but validating data are lacking. Various models predict widely different radiative heating levels. For example, predictions of ASTV radiative heating from only the VUV atomic lines range from insignificant amounts to levels dominating the overall heating (references 6, 7 and 8).

Arc-jet wind tunnels can produce the enthalpy and pressure conditions simulating these high speed entries. These facilities generally consist of an arc heater, a supersonic nozzle, a test box, a model holder and the necessary equipment to deal with the extreme heat transfer and the exhaust. Reference 9 describes arc-jet wind tunnels in some detail. In the past their main use has been for heat shield development. Future uses will include aerothermodynamic testing for spacecraft flight. Also these facilities can be used to conduct experiments to validate computational codes. Even though the size scale cannot be simulated, a flow-field rich in non-equilibrated, radiating gas can be

generated. Computational models can be exercised on arc-jet test conditions for comparison with experimental results. There are some major difficulties in this approach, however. The free stream plasma flow conditions (enthalpy, species distribution, energy states distribution, etc.) in an arc-jet are not well understood. Initial conditions for shock layer computational models can only be estimated. At present there are efforts to calculate the model test environments using computational models starting with the arc column, continuing with the conical or contoured expansion nozzle, and culminating in the flow field of a model located in the exit flow from the nozzle (reference 10). Experimental results are needed to support the theoretical work. A review of techniques used to study arc-jet wind tunnel flow is given in reference 11.

This paper reports on initial results of an arc-jet wind tunnel experiment. The experiment measured the spectral radiative flux emanating from the shock layer and incident on a blunt model placed in the supersonic stream. Data was taken from 120 nm to 900. This paper presents results the longer wavelength results from 200 nm. The VUV results will be reported on elsewhere. The purpose was to gather data to help characteriz ; the stagnation region shock layer flow. Understanding this flow would be valuable for development and validation of advanced arc-jet wind tunnel design codes and help extend the capability of this class of facility to advanced aerothermodynamic testing.

The data shown in this paper are preliminary and do not benefit from final calibrations. The flux was spectrally resolved and over a wide range. The data will be analyzed and used to identify important radiating species and help determine the state of the gas and the operating characteristics of arc-jet wind tunnels.

EXPERIMENTAL SETUP

The experimental setup is as described in reference 12 except that the model diameter was increased to 6 inches. Figures 2 and 3 are from this reference and are included here. Figure 2 is a schematic plan view of the experiment. Supersonic flow from the arc is produced in the nozzle and the model is placed in the free stream. The standing shock layer over the model is indicated. Figure 3 is a schematic view of the model. The model face is a 6" diameter flat disk and the entire model is water cooled. A small aperture centered on the forward face admits the surface radiative flux. A helium cooled window, shown immersed in a cavity below the aperture, transmits the surface flux into the optical system. The optical system consists of a flat mirror, directing th optical path to a concave mirror, which in turn collimates the beam to another concave mirror shown at the top of figure 2. This mirror focuses the aperture,

via a flat turning mirror, onto the slit of the spectrograph. The spectrograph
was a 0.5 meter instrument using a modified Czerny-Turner optical layout with
the provision for operating either as a scanning monochromator or a film
spectrograph . The portions of the system exposed to the plasma were all water
cooled. Figure 4 shows the model arrangement in the test box. The nozzle exit
can be seen at the left, and the aperture can be seen centered on the model face.
The optical axis in front of the model was canted 15° from the centerline to
reject radiation from the arc column.

TEST CONDITIONS

The test was conducted in the Ames 20 Megawatt Aerodynamic Heating Facility.
The facility was operated with a supersonic nozzle with a 1.5 inch diameter
throat and an 18" exit diameter. The facility operating parameters were as
follows:

> Test gas mixture: 80% air* and 20% Argon by mass,
> arc current: 1000 amperes,
> arc column pressure: 15 psia,
> nozzle pressure: 7.5 psia,
> test box pressure: 0.2 to 0.3 mm Hg, and
> stagnation pressure: 9 mm Hg.

The resulting free stream conditions for the present experiment is approximate
as indicated in by the circle in figure 1. The velocity is deduced from an
estimate of the free stream enthalpy which was, in turn, derived from the
heating rate of a small sphere placed in the stream. It should be noted that the
arc-jet free stream enthalpy, although repeatable, is not well characterized.
Indeed, one of the objectives of this experiment is to help quantify this and
other arc-jet wind tunnel performance characteristics.

Figure 5 is a photograph taken during a test. The shock is seen well formed over
the flat model face. The intense radiation from the high temperature shock
layer gases is clearly evident.

The experiment consisted of a series of 10 minute runs during each of which a
specific spectral region was examined. The length of a run was limited by the
heating loads on the test box. Data were obtained using film and
photomultiplier tubes. The photomultiplier signal was processed with

---

* Dried and filtered ambient air

synchronous amplification. Readout was on a cha recorder and digitally recorded.

The instrument configurations used in the tests are summarized in Table 1.

DIGITAL DATA ACQUISITION

Four signals were recorded digitally during the experiment tests: stagnation pressure on the model face, optical system vacuum pressure, photomultiplier high voltage, and photomultiplier output signal. The stagnation pressure, vacuum pressure, and the high voltage were recorded at one hertz with an analog mixer. The photomultiplier output signal was recorded forty hertz.

Figure 6 shows the configuration of the data recording system for the time history of the pressure, vacuum, and high voltage signals. The system used a multiplexer and a controller configured with a portable personal computer. Twisted and shielded grounded cables were used to transmit the signals. The data acquisition and instrument control software were configured to record the data during each run at one hertz and concurrently display it on the monitor.

Figure 7 shows the configuration of the data recording system for the photomultiplier records. The system consisted of a controller, a scanning A/D converter, and a 16 channel isolated input rack connected to an NB-DMA board contained within the personal computer system. The data acquisition and control software was set to record at 40 Hertz.

The photomultiplier data presented here were manipulated for display purposes using graphic and analysis software.

RESULTS AND DISCUSSION

Computed Spectral Details.

The development of computational codes to predict the shock layer radiation, such as that measured by this experiment, is a parallel, ongoing activity at the Ames Research Center. These codes are based on calculations of the arc process, the expansion in the nozzle and the shock layer processes. The radiating shock region is very non-homogeneous and involves many kinetically controlled processes. Substantial radiation emanates from the nonequilibrated regions immediately behind the shock. Here the kinetic temperature is extremely high, approaching 50,000K. The spectral line radiation is strongly Doppler broadened by this high temperature. The cooler parts of the shock will

partially absorb the strong features directed toward the surface, but absorption will occur only at around the line centers because the absorption lines are narrow due to the low kinetic temperature. The surface radiative heating flux is thus seen to be the aggregate radiation from regions of very different conditions and estimates from computational codes involve consideration of complex interactive and kinetic processes. At present these codes exist as separate codes but the goal is to couple them together and validate the result as a reliable code for predicting arc-jet wind tunnel conditions. Figure 8 is a calculated spectrum. NO bands are seen from 190 nm to 300 nm. $N2(2+)$ bands contribute energy from 280 nm on and merge with the stronger $N2^+(1-)$ and $N2(1+)$ bands which dominate the molecular systems from 300 nm to the infrared. Rich and diagnostically important atomic line radiation is predicted from oxygen and nitrogen in the infrared.

Test Results

As indicated above the data were taken with film and with photomultiplier tubes. The data presented herein are not corrected for instrument spectral response. This correction will be done with future work. The photomultiplier data was digitized in-situ. The film spectra density will be subsequently digitized.

Ultraviolet-visible results.

Data was acquired in the spectral region from 200 nm to 500 nm by both film and photomultiplier tube. Figure 9 is a print from a film record taken on 8/10/92. The spectral range is from 330 nm to 450 nm. The uppermost spectrum is from the shock layer radiation and includes $N_2^+(1-)$ $B^2\Sigma_u^+-X^2\Sigma_g^+$ and CNv $B^2\Sigma-X^2\Sigma$ band systems and atomic lines from nitrogen and oxygen. The other spectra are mercury line calibrations. Figure 10 is a densitometer scan of the 360 nm to 395 nm region of figure M in which details of a portion of the $N_2^+(1-)$ system are shown. The vib-rot structure can be seen in detail. This and the other film records will be digitally analyzed for subsequent use. Photomultiplier data were obtained in this region also. Figure 11 shows photomultiplier data of the spectral details from 200 nm to 300 nm. This spectral region is dominated by the NO_γ $A^2\Sigma^+-X^2\Pi$ bands. Figure 12 is the photomultiplier data from 250 nm to 500 nm. These data were recorded digitally in-situ as well as with chart recorder backup. As with the VUV data, there is no correction to these figures to account for instrument spectral response. This correction awaits further laboratory work.

Visible-infrared results.

Time limitations prohibited use of photomultiplier tubes beyond 700 nm. Film spectra, however, were obtained with great detail. Figure 13 is a print of the film taken from the 7/23/92 test. It covers the spectral range from 450 nm to 950 nm with a resolution of approximately 0.1 nm. Figure 14 is a densitometer trace of this record. The details which overlap with the photomultiplier record can be seen. The important atomic oxygen and nitrogen emission lines are well resolved. Figure 15 is an densitometer trace of an expanded portion of this film indicating the resolution of the atomic lines. Several features await identification. Calibrations of the non-linearities of the film system will result in a data base allowing comparison of the intensities of these features with theoretical results. Their relative intensities will help understand the electron density of the plasma.

CONCLUSIONS

The spectra have been obtained from the flux incident on the stagnation surface of a flat model placed in the supersonic stream in an arc-jet wind tunnel. The preliminary data set shown is detailed at high resolution from 200 nm to 1000 nm. Important radiators are evident. The data set will be further developed and used to help refine and calibrate computational models of the aerothermodynamics of entry and of arc-jet wind tunnels.

ACKNOWLEDGMENTS

TABLE 1

I-TESTS USING FILM

Date	Grating Ruling, *l/mm*	Blaze Wavelength *nm*	Slit *microns,*	Exposure, *seconds*	λ range *nm*
7/8/92	60	300	20	100	200 to 500
7/15/92	180	150	20	60, 300	200 to 500
7/16/92	300	500	20	10, 50, 300	300 to 1000
7/23/92	300	500	20	100, 390	300 to 1000
7/24/92	1200	150	20	100, 600	200 to 400
8/10/92	1200	150	20	10, 100, 480	300 to 500

II-TESTS USING PHOTOMULTIPLIER TUBE

	Grating *l/mm*	Blaze *nm*	resolution, *nm*	spectral features	λ range, *nm*
8/4/92	2400	150	0.4	$N2^+(1-)$	300 to 500
8/4/92	2400	150	0.1	$N2^+(1-)$	300 to 500
8/5/92	2400	150	0.4	NOγ	200 to 290
8/5/92	2400	150	0.1	NOγ	200 to 290

REFERENCES

1. Walberg, Gerald D., "A Survey of Aeroassisted Orbit Transfer", J. Spacecraft, 22, 1, Jan-Feb 1985

2. Shinn, Judy L., and Jones, Jim J., "Chemical Nonequilibrium Effects on Flowfields for Aeroassisted Orbital Transfer Vehicles", J. Spacecraft, 22, 1, Jan-Feb 1985

3. Park, Chul, "Radiation Enhancement by Nonequilibrium in Earth's Atmosphere" J. Spacecraft, 22, 1, Jan-Feb 1985

4. Williams, L., Putnam, T., Morris, R., "Aeroassist Flight Experiment", Aeronautics Division, Headquarters, National Aeronautics and Space Administration, Washington, D.C.

5. Park, C., "Problems of Rate Chemistry in the Flight Regimes of Aeroassisted Orbital Transfer Vehicles", Reprinted from "Thermal Design of Aeroassisted Orbital Transfer Vehicles", H. F. Nelson ed., Progress of Astronautics and Aeronautics, 96, 1985.

6. Whiting, Ellis E., and Park, Chul, " Radiative Heating at the Stagnation Point of the AFE Vehicle", NASA TM 102829, November 1990.

7. Carlson, L. A., "Approximation for hypervelocity, Non-equilibrium, Radiating, Reacting, and Conducting Stagnation Regions", AIAA Thermophysics, Plasmadynamics and Laser Conference, June 27-29, 1988, San Antonio, TX, AIAA Paper 88-2672.

8. Moss, J. N., "Non-equilibrium Thermal Radiation for an Aeroassist Flight Experiment Vehicle", AIAA 26th Aerospace Science Meeting, Jan. 11-14, 1988, Reno NV, AIAA Paper 88-0081.

9. Balter-Peterson, Aliza, et. al., "Arc Jet Testing in NASA Ames Research Center Thermophysics Facilities", Proceedings from AIAA/NASP International Aerospace Planes Conference, Orlando, FL December 1-4, 1992

10. Babikian, Dikran, Gopaul, Nigel K. J. M., and Park, Chul, "Measurement and Analysis of NO Radiation in an Arc-Jet Flow", Proposed paper for AIAA 28th Thermophysics Conference, July 6-9, 1993, Orlando, FL.

11. Scott, Carl D., "Intrusive and Nonintrusive Measurements of Flow Properties in Arc Jets", Invited paper for the Workshop on Hypersonic Flows for Reentry Problems", co-organized by INRIA-Sophis Antipolis and GAMNI-SMAI, January 22-26, 1990, Antibes, France.

12. Palumbo, G., "Shock Layer Vacuum UV Spectroscopy in an Arc-Jet Wind Tunnel" NASA TM 02258, January, 1990.

FIGURES

Figure 1.
Flight regimes of mission returns for ASTV, Shuttle, and Apollo. The point indicated by the circle is an estimate of the altitude and velocity simulated by the a c-jet conditions used during the present tests.

Figure 2.
Schematic diagram of experimental setup. The arc column is to the left of the nozzle.

Figure 3.
Schematic diagram of model showing the aperture and window and orientation of the bow shock. Radiation incident onto the surface is reflected by the turning mirror to the concave mirror and thence to the spectrograph. Vacuum was maintained <0.01μ for the VUV tests.

Figure 4.
Photograph of model in test box. The optical system is protected by the water cooled coils shown as well as internal water cooling. The aperture can be seen in the face of the model. The nozzle exit can be seen at the left.

Figure 5.
Photograph of model during test. The stagnation shock is seen well formed over the model face and the intense radiation from the shock heated air is evident.

Figure 6.
Data acquisition system block diagram for recording the stagnation pressure on the model face, optical system vacuum pressure, photomultiplier high voltage.

Figure 7.
Data acquisition system block diagram for recording the photomultiplier output signal.

Figure 8.
Preliminary calculation of the spectral surface flux from the stagnation region of a model placed in an arc-jet wind tunnel.

Figure 9

Print from a film record taken on 8/10/92. The spectral range is from 330 nm to 450 nm. The uppermost spectrum is from the shock layer radiation and includes $N_2^+(1-)$ $B^2\Sigma_u^- - X^2\Sigma_g^-$ and CNv $B^2\Sigma - X^2\Sigma$ band systems and atomic lines from nitrogen and oxygen. The other spectra are mercury line calibrations.

Figure 10

Densitometer trace of the 360 nm to 395 nm region of the film record of figure M is shown. This region includes a portion of the $N_2^+(1-)$ $B^2\Sigma_u^- - X^2\Sigma_g^+$ band system. The vibration-rotation lines are seen to be well resolved. The atomic oxygen line at 394.8 nm is also shown.

Figure 11

Photomultiplier record of spectrum from 200 nm to 300 nm. This spectral region is dominated by the NO_γ $A^2\Sigma^+ - X^2\Pi$ bands.

Figure 12.

Photomultiplier record of spectrum from 250 nm to 500 nm. The molecular spectra from NO_γ $A^2\Sigma^- - X^2\Pi$, $N_2^+(1-)$ $B^2\Sigma_u^- - X^2\Sigma_g^-$ and CNv $B^2\Sigma - X^2\Sigma$ are in this region as well as atomic lines from oxygen and nitrogen and copper (contamination from the arc electrodes).

Figure 13.

Photographic print of 7/23/92 film spectrum from 450 nm to 950 nm. Two different duration exposures of the shock layer emission were taken. Exposure A is a short exposure of emission from the shock layer and an overlapping calibration exposure from a Hg lamp. Exposures B and D are Hg lamp calibration exposures. Exposure C is a long exposure without overlapping Hg lamp calibration. Selected Hg emission lines in the first, second and third orders, are indicated.

Figure 14.

Densitometer trace of 7/23/92 film spectrum from 500 nm to 1000 nm. The important atomic oxygen and nitrogen emission lines are well resolved. Also seen are the copper lines at 324.7 nm and 327.4 nm in the second and third orders.

Figure 15.

Expanded portion of the 7/23/92 film spectrum densitometer trace showing the atomic lines near between 800 nm and 880 nm. Several features await identification.
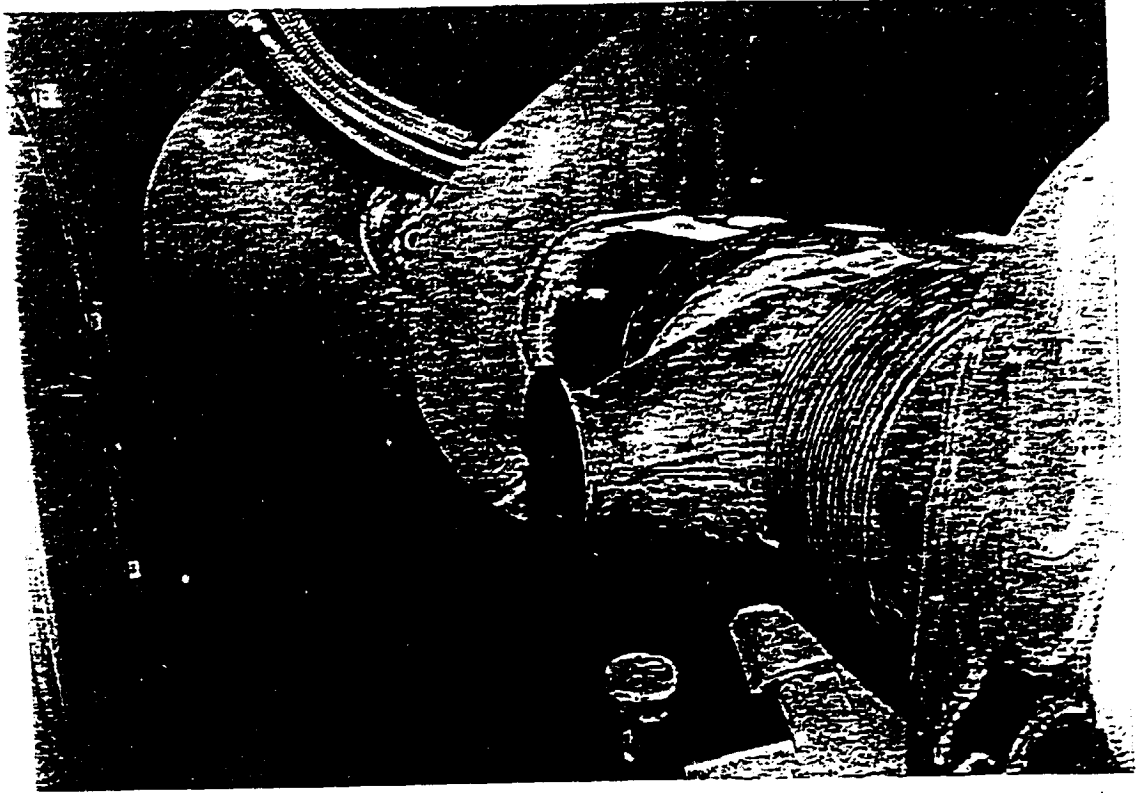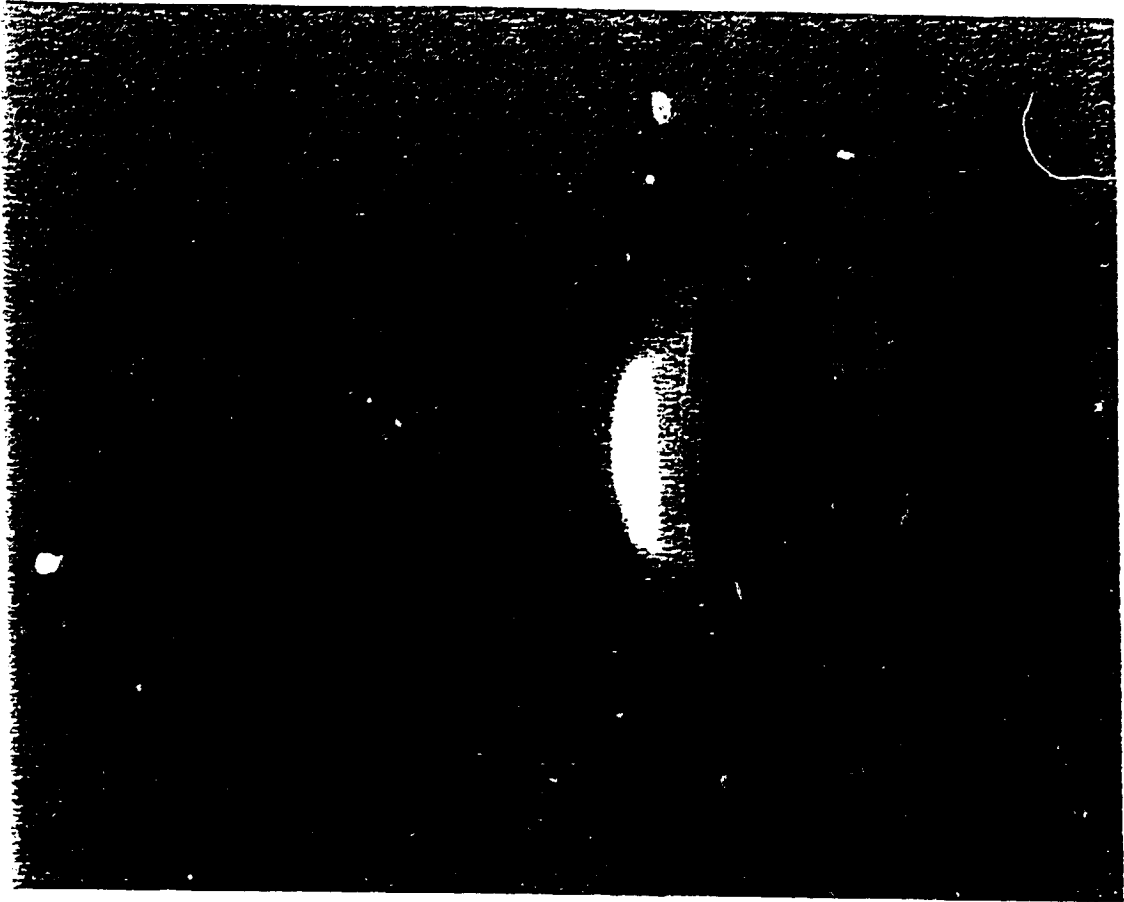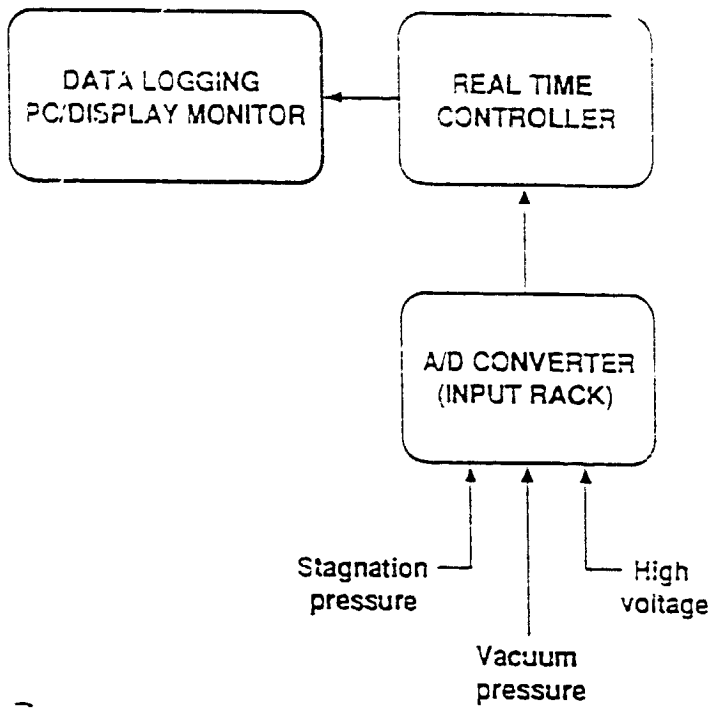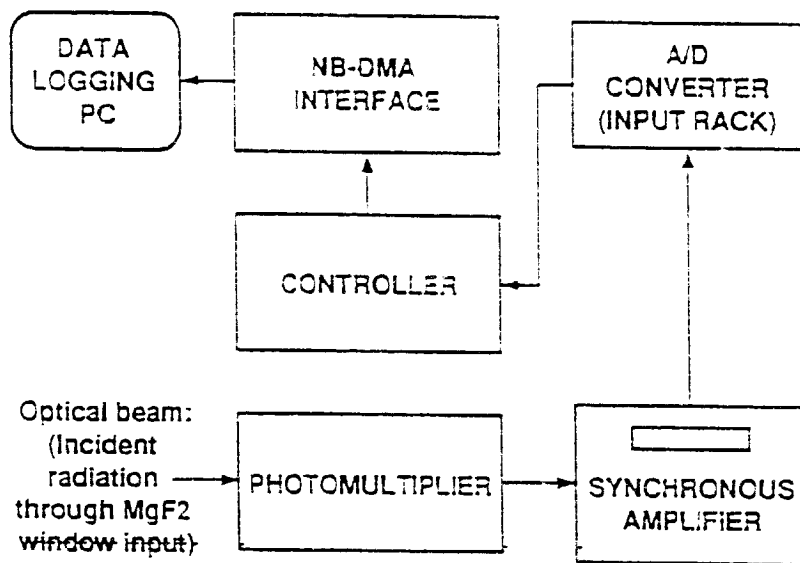
Shuttle entry

Significant nonequilibrium

ASTV

1% ionization   Apollo entry

Equilibrium

Altitude (ft × 10⁻³)

Velocity (ft/sec × 10⁻³)

Palumbo-1

0.5-m UV spectrograph

Concave mirror

Flat turning mirror

Standing shock

Nozzle

Exhaust

Flow

Model

Concave mirror

Flat turning mirror

Palumbo-2

Shock

Turning mirror

MgF$_2$ window

He flush

15° off axis
light cone

To spectrograph
optics

Vacuum

Palumbo-3

4

5

```
┌─────────────────────┐         ┌─────────────────────┐
│   DATA LOGGING      │◄────────│    REAL TIME        │
│  PC/DISPLAY MONITOR │         │    CONTROLLER       │
└─────────────────────┘         └─────────────────────┘
                                          ▲
                                          │
                                ┌─────────────────────┐
                                │   A/D CONVERTER     │
                                │   (INPUT RACK)      │
                                └─────────────────────┘
                                   ▲     ▲     ▲
                                   │     │     │
                        Stagnation ┘     │     └─ High
                        pressure         │        voltage
                                      Vacuum
                                      pressure
```

Pakurbo-6

DATA LOGGING PC ← NB-DMA INTERFACE ← A/D CONVERTER (INPUT RACK)

CONTROLLER

Optical beam: (Incident radiation through MgF2 window input) → PHOTOMULTIPLIER → SYNCHRONOUS AMPLIFIER

Panurroo-7

Calculations

Wavelength (nanometers)

Wavelength (nanometers)

Hg lines

365.6   435.8

394.8 O

Wavelength (nanometers)

360   365   370   375   380   385   390   395

Wavelength (nanometers)

Wavelength (nanometers)

NOγ
258.7
263.0
267.1
271.3
295.2 NOγ
315.9 NOγ
324.7 Cu
327.4 Cu
353.2 N$_2^+$ (1-)
354.8 N$_2^+$ (1-)
356.3 N$_2^+$ (1-)
358.2 N$_2^+$ (1-)
385.1
386.1   CNv
387.1
388.3 CNv
388.4 N$_2^+$ (1-)
391.4 N$_2^+$ (1-)
394.8 OI
409.9 NI
410.9 NI
423.6 N$_2^+$ (1-)
427.8 N$_2^+$ (1-)
436.8 OI
465.4 OI
466.2 NI
467.2 OI
493.5 NI

0   5   10   15

250   300   350   400   450   500

Wavelength (nanometers)

A
B
C
D

312.6 313.0
(3rd order)

253.1
(3rd order)

365.0
(2nd order)

312.6 313.0
(2nd order)

253.6
(2nd order)

435.8

Hg lines

394.8

Palumbo No. /3

Cu (3rd order)

N₁ lines

O₁ lines

N₁ lines

O₁ line

N₁ lines

O₁

Cu (2nd order)

Wavelength (nanometers)

500   600   700   800   900   1000

Axis: Wavelength (nanometers)
X-axis values: 810, 820, 830, 040(840), 850, 060(860), 070(870), 800(880)

Peak labels:
N_I lines
N_I (821.0)
N_I (824.2)
O_I (844.6)
N_I (856.7)
N_I (859.4)
N_I (862.9)
N_I (865.5)
N_I lines
N_I lines

Bottom marking: Figure S/...
Wavelength (nanometers)

N_I lines

N_I (821.0)

N_I (824.2)

O_I (844.6)

N_I (856.7)

N_I (859.4)

N_I (862.9)

N_I (865.5)

N_I lines

N_I lines

810   820   830   840   850   860   870   880

AIAA 94-0656

APPLICATION AND VALIDATION OF THE FL3D SOLVER TO PROPULSION FLOWS

C. R. Bobba,
R. K. Rout and J. L. Younghans

GE Aircraft Engines
Cincinnati, OH.

E. Venkatapathy,

Eloret Institute
Palo Alto, CA.

32nd Aerospace Sciences Meeting & Exhibit
January 10-13, 1994 / Reno, NV

APPLICATION AND VALIDATION OF THE FL3D SOLVER
TO PROPULSION FLOWS

C. R. Bobba, *Senior Engineer,* *
R. K. Rout, *Senior Engineer,*†‡
and
J. L. Younghans, *Manager* †
General Electric Aircraft Engines
Cincinnati, Ohio, 45215

Ethiraj Venkatapathy, *Scientist,*†*
Eloret Institute, 3788 Fabian Way,
Palo Alto, California 94303

ABSTRACT

The FL3D solver, a full three-dimensional Navier-Stokes solver, has been applied to a number of problems of interest to GE Aircraft Engines Co. This validation exercise had two purposes. The first goal was to evaluate the accuracy, ease of use and cost of computing the complex internal, external and coupled flow problems with the FL3D solver. The second motive was to apply the solver in the preliminary mode and evaluate its adaptability to propulsion component design. A limited number of examples have been solved and the solutions are compared with available experimental data. The advantages and limitations with the FL3D solver are discussed. Experience gained with the solver and its use in the design environment are included.

INTRODUCTION

The propulsion system design involves component flows that are internal, external and regions where these two types of flows interact. In addition solutions are sought where complex configurations such as center-bodies, mixer chutes, primary and secondary flow interaction, plume interference, boundarylayer and shearlayer developments etc . are common elements. Often in the design process, a number of geometric and fluid dynamic parameters are varied to understand the design performance under design and off design conditions. With intuitive knowledge and understanding of the flow the designers may choose to introduce novel changes and this may require computations to be performed with rapid turn around yielding plausible directions to the design efforts, for example, film cooling with blowing on an airfoil at select locations. For a CFD solver to be used in a general design environment, one would like it to be robust, accurate, flexible and be able to handle not only complex configurations but also changes to the original geometry the design process may suggest in a timely fashion.

FL3D is a robust compressible flow Navier-Stokes solver developed at NASA Ames Research Center. The solver has been validated for external high-speed flows. GE Aircraft Engines recently acquired this solver. The solver has been undergoing validation and calibration tests on a number of internal, external and mixed flows of interest. Some of these problems have either experimental or other numerical solutions. These problems exhibit the real world complexities but are easier to model. Other problems are of design and exploration type and were chosen to explore the user friendly and stability aspects of the FL3D solver.

The primary objective of this paper is to catalogue the experiences and understanding gained with the FL3D solver. As such the qualitative aspects of the solution characteristics for each case are discussed. The successes as well as the shortcomings of the solver are outlined.

CFD SOLVER

All the CFD solutions to be presented in this paper were obtained with the FL3D[1-3] solver. This is an implicit, full Navier-Stokes solver and uses Roe upwind, TVD, flux-difference splitting technique to represent the inviscid fluxes and a central-difference approximation to represent the viscous fluxes. It is second-order accurate in space and first order accurate in time. With the use of local time step to converge faster to steady state, the time accuracy is not maintained. Though time accuracy is not maintained, the scheme is a time marching hyperbolic method wherein the steady state solution is obtained by marching from a prescribed solution. The solver is capable of handling single, zonal or multiple grids with and without hole regions. A single block version with blank region (Iblanks) topology was used for all the present computations. A large number of boundary conditions are available and are specified through input by the user. These boundary conditions can accommodate many of the real world problems. The FL3D code is configured to require minimal memory and has been ported to Workstation platforms, such as HP workstation.

The convergence to steady state is problem dependent and for simple 3-D problems like nozzles, steady state solutions have been obtained within 1000 iterations. For com-

plex problems, more than 6000 iterations in time were required to reach a steady state solution. The limiting mechanism seems to be the evolution of separated flow domain and /or the shock structures in the computational domain. The convergence rates of the solver seems to be slow while solving the incompressible flows (Mach number less than 0.3 in the freestream) while maintaining good accuracy of the solution.

GRID GENERATION

A number of grid generation tools were used to generate the grids. These tools varied from simple algebraic grid generators to commercially available software packages like IDEAS and GRIDGEN3D. For complex problems grid generation has been the most time consuming of tasks. In addition to the initial grid generation, adaptive regridding has been utilized in a limited number of problems to improve solution accuracy. SAGE[4], an algebraic solution adaptive grid redistribution scheme, was used in the present work to generate adaptive grids.

TURBULENCE MODEL

The FL3D solver contained the original Baldwin-Lomax algebraic turbulence model. This model was augmented with a free shear-layer model. This is a simple mixing length model and it is similar to Prandtl's mixing length model for free shear layer flows. The model was developed with the aid of extensive data base on supersonic plumes measured at Florida State university[5,6,7]. In particular

$$\mu_t = C_1(\rho) * (L^2) * (\omega) \tag{1}$$

where :

$$C_1 = 5.9725.$$

$$\rho = \text{density}.$$

$$\omega = \text{vorticity}.$$

$$L = 0.60 * (1 + \sqrt{\frac{\rho}{\rho_{ref}}}) * X_{eq}$$

and

$$X_{eq} \simeq C_2 * r_{jet} * \tan^{-1}(\frac{1}{C_2} * (\frac{x}{r} - (\frac{x}{r})_{cutoff} + \frac{\pi}{2}))$$

$$C_2 = 6.3662$$

It should be pointed out that $(\frac{x}{r})_{cutoff}$ is problem dependent. For the test cases that were studied in the present work $(\frac{x}{r})_{cutoff}$ was assumed to be 20.0. It appears to us that this needs to be investigated further to determine the validity of this model.

The function X_{eq} is defined in an analogous fashion similar to mixing lengths in boundary layer estimates. The constants and functional relationships are developed from the data base from Florida State University. This model was

used to simulate the supersonic plume characteristics and yielded satisfactory agreement with measurements. The purpose of this simple model is to gain some understanding of mixing in high speed high temperature (1000 degrees F and up) plumes and determine dominant factors influencing the mixing. The desire is to provide data base for higher order turbulence models that can better describe the characteristics of supersonic jets. These algebraic models available in FL3D solver are considered ad hoc models at best. The limited number of turbulent solutions obtained with this model have proven to be cost effective and sufficiently accurate for design purposes.

RESULTS AND DISCUSSION

A number of internal and external flows and plume-interaction flow problems were computed. Summary of the results are given below. Computed results are compared with experimental data whenever available.

1. 3D - 29° Vectored Nozzle :

The objective is to validate the FL3D solver. In this 3-D internal flow problem the cross section of the nozzle transitions from circular cross section to rectangular section at the nozzle exit. Also, the nozzle design is such that the outflow is turned 29° to the incoming flow to vector the flow in a desirable direction. The flow is fully 3-D. The nozzle geometry, grid and mach number contours are presented in Figure 1. Comparison of wall pressure distribution between the computed solution and the experimental measurement, shown in Figure 2, is very good. The mach number contours along the symmetry plane shows the flow to be very three dimensional. The predictions were able to capture the shocks and their reflections in the aft section of the nozzle.

Detailed look at the solution near the throat section of the nozzle revealed the shock-boundary layer interaction and flow separation. In the design of nozzles, it is very useful to know the existence and extent of separated flow regions. The computed solution was able to predict a small recirculation zone at the throat of the top wall as expected. The good agreement of the measured data and the computations are presented in Figure 2. Several significant features of the solution predicted by FL3D solver are: 1) its ability to capture the shocks and their subsequent reflections off of the walls, 2) its ability to simulate shock boundary layer inter-action and its ability to predict the separation and 3) reattachment of the flow under the influence of changing pressure gradients in the flow domain. This example is presented here as a validation of the code's predictive capabilities.

2. 3D Multi Stream S-Duct Flow :

The objective in computing this problem was to evaluate the code's capability to simulate, a) mixing of hot and cold streams, b) compression corner effects, and c) expansion corner and curvature effects. The geometry for this problem was selected carefully to include all the features to simulate the above mentioned complexities. At the inlet an axisymmetric cold-stream at 880° R and a hot core flow at 1995° R were introduced. These two flows are separated at inlet

by a wall. The schematic of the flow features, the geometry and a representation of the grid used are shown in Figure 3. The grid is dense at the region where the cold and hot flows meet in the inlet region. Both the flows at entrance are subsonic. The mixed flow accelerates to Mach number 1.0 as it approaches the throat. Beyond the throat region the flow expands to supersonic flow as it passes through the nozzle. The cross sectional grid, total temperature distribution, Mach contours along the axial plane and at selected cross sections are presented in Figure 4. The Mach number distribution shows a large acceleration on the expansion corner and deceleration at the bottom corner. The total temperature distribution shows the development of the shearlayer and the mixing of the hot and cold flows in this region. The sharp curvature changes in the geometry gave rise to the formation of two vortices. These vortices in turn promoted further mixing of the two streams in the duct. The total temperature contours presented in Figure 4, clearly shows the dramatic effect of these vortices. Beyond the throat a divergent nozzle was attached to the geometry to further examine the capabilities of the code, FL3D, to simulate the supersonic flow. Details of the calculations showed the flow separation and reattachment at the top wall of the duct. The recirculation regions created by the compression corner at the bottom wall are also captured satisfactorily by the predictions.

In summary the qualitative results presented here demonstrate the ability of the FL3D code to predict the mixing of hot and cold flows coupled with the influence of the sharp curvature changes in the geometry. It shows further evidence of the code's ability to satisfactorily simulate the influence of expansion corners in supersonic flow regimes.

3. 2-D Splitter Plate flow:

This problem was selected to demonstrate the influence of geometry changes on the solution. The geometry consists of channel formed by a 40 inch long top and bottom walls. A splitter plate of 8 inches long is introduced to split this channel in two separate channels at the entrance. In the top channel a cold subsonic stream was introduced. In the bottom channel a hot choked flow was introduced. The static temperature ratio of the two flows (Hot/Cold) is 1.1 .

In this exercise two problems are considered. For both the problems the bottom wall and the splitter plate geometries are held at fixed positions. In the first problem the top wall is held parallel to the bottom wall. Whereas in the second problem the top wall was diverging to an overall increase of 5 per cent in the exit area starting at 20.0 inches from the inlet. The hot flow between the splitter and the bottom wall is expanded (transonic flow mach 1.2 at the end of splitter plate) and is interacting with the cold flow from the top channel. The development of the boundary layer on the top wall and the mixing layer from the end of the splitter plate are captured properly by the code.

The splitter plate thickness and small changes in the angle of the top wall had significant effect on the flow development. The computational grid and the temperature con-

tours from the computed solutions are shown in the top of Figure 5. The bottom two figures compare the estimated temperature distribution on the top wall. The small changes in geometry had significant effect on the solution and this is demonstrated by changing the top channel (secondary flow) cross-section slightly. This in turn caused large changes in the predicted pressure. The primary(bottom channel)/core flow can be allowed to reach either subsonic or supersonic conditions by the small changes introduced in the secondary (top channel) flow region. The differences in the computations and the measurements are due to the uncertainty in the geometric data provided by the experimental groups. Geometry for the first 20 inches are known accurately and the rest of the geometry was not. The disagreement of the computations with data for this example may be partly due to the turbulence model and its inability to simulate supersonic mixing satisfactorily.

4. Supersonic nozzle flow with center body:

The aim here is to introduce a contoured center body in a supersonic nozzle and evaluate the solution. The geometry considered is an axisymmetric nozzle with center body and the flow is choked at the throat and the flow is supersonic at the exit. Figure 6 shows the grid and the Mach number contours from the predicted solution. The choking of the flow at the throat and the compression produced along the compression region of the center body due to the change in curvature is clearly seen. A shock wave has developed at this region on the center-body (where the curvature of the geometry is changing) and is subsequently reflected off of the nozzle wall. The effects of the curvature on supersonic nozzle flows were captured well by the code with no surprises.

5. The effect of External Pressure:

The intent of this problem is to investigate the effect of the over-expansion of the supersonic nozzle flow under simulated freestream flow conditions. An external (outside wall) wall was added to the nozzle geometry shown in the previous problem. A high subsonic free stream flow of Mach number 0.9 is included in the problem definition. With this external flow condition the nozzle exit flow was over expanded. The combined grid and the FL3D estimated mach number contours are shown in Figure 7. The interaction of these flows (nozzle flow and external flow) created an extremely complex flowfield as presented in the mach number distribution shown here. The external wall of the nozzle is contoured to accelerate the freestream flow on it as a result of this flow acceleration on the nozzle external wall Mach number exceeds 1.0 on it, thus reducing the pressure on the wall. The subsequent recompression of the flow to regain the static pressure balance gives rise to the shock; a lambda shock; on the nozzle wall. The shock-boundary layer interaction, coupled with the over expanded flow led to the complicated shock pattern inside the nozzle as shown in the figure. These interactions separated the flow from the nozzle wall both inside as well as out side. A plot of the velocity vectors, Figure 8, at the trailing edge of the nozzle

clearly indicate the flow reversals, recirculations, and separation due to the shock boundary layer interactions in an over expanded supersonic flow under simulated high subsonic freestream flow.

6. Axisymmetric Turbulent Plumes:

Plumes are an integral part of propulsion system. They can occur either external or internal as in the case of single sided expansion ramp, one sided evolution of plumes determine the thrust efficiency. To validate the CFD solver for plumes axisymmetric under-expanded and ideally expanded plumes are considered. Detailed measurements of the flow characteristics from such supersonic jets are made at Florida State University (1991-1992 Mechanical Engineering Department/ GE - FSU Cooperative program). A simple mixing length turbulence model was devised to simulate the turbulent jets. Calculations are made with this model to predict the characteristics of the under-expanded jets and fully expanded jets. The predicted temperature contours for these jets are shown in Figure 9. The shock patterns shown for the under-expanded jets are indicative of the plausibility of the solution. The shock free nature of the fully expanded jets is also presented in this figure. A comparison of Mach number distribution on the centerline of the jet with measured data is presented in Figure 10. The agreement between the measurements and predictions for the fully expanded (shock free conditions) jets shown in figure is very good. For underexpanded jets, the nozzle pressure is higher than the ambient pressure. As such the jet expands to reach a pressure balance with that of the ambient pressure; thus giving rise to higher Mach number down stream of the nozzle exit. In this process the jet over expands and tries to achieve pressure balance via compression (oblique shock formation) wave. This procession of expansion and compression, after the nozzle exit continues till the pressure in the jet reaches that of the ambient pressure. The ability of FL3D to predict such flow properties with proper frequency (the number of expansions and compression cells) and amplitude (magnitude changes) of the mach number is shown in the figure. Comparison of the predictions with experimental data presented in the figure shows satisfactory agreement.

These comparisons demonstrate the ability of the FL3D to accurately predict a variety of complex flow fields from propulsion systems

Conclusions

The predictions and their comparisons with experimental data; whenever available; demonstrate that the code

FL3D can capture the salient characteristics of supersonic/transonic nozzle flows. Curvature effects of the nozzle geometry on the flow fields are predicted accurately. Its ability to estimate the properties in a shearlayer is demonstrated in the splitter-plate problem. The computational experiments performed further show the capabilities of the code to predict separation, recirculation and flow reversals in a complex flow field. Its ability to capture shocks has been demonstrated amply through the exercises presented here. The application of code to predict the supersonic jet flow fields has been demonstrated in this work. Our experience shows that FL3D can simulate the flow fields for propulsion systems adequately.

ACKNOWLEDGEMENTS

References

[1] Venkatapathy, E., Feiereisen, W.J., and Obayashi, S., "Computational Studies of Hard-Body and 3-D Effects in Plume Flows," AIAA Paper 89-0129, January 1989.

[2] Venkatapathy, E.,and Feiereisen, W.J., "Computational Analysis of Plume Induced Separation," AIAA Paper 91-0711, January 1991.

[3] Ruffin, S.M., Venkatapathy, E., Lee, S.H., Keener, E.R., and Spaid, F.W,. " Hypersonic Single Expansion Ramp Nozzle Simulations, " Journal of Spacecrafts and Rockets , Vol.29, No. 6, 1992.

[4] Davies, C.B., and Venkatapathy, E., " Application of a Solution Adaptive Grid Scheme to Complex Three-Dimensional Flows ", AIAA Journal, Vol.30, No. 9, September 1992.

[5] Ying, S.X., Bobba, C.R., and Younghans, J.L., " Design and Evaluation of Novel Exhaust Systems – A Numerical Study", Proceedings of Tenth International Symposium on Air Breathing Engines, (ISOABE), Volume 1, September, 1991. Nottingham, England.

[6] Narayanan, M., Ying, S.X., Bobba, C.R., Younghans, J.L., " A Numerical Study of Compressible Viscous Flow in a Novel Exhaust System", AIAA Paper 91-1728, 1991.

[7] Bobba, C., Early, K.S., " Three Dimensional Flow Characteristics of Under and over Expanded Rectangular Jets", Proceedings of The Specialty Group on Targets, Backgrounds and Discrimination. Held at Naval Postgraduate School, Monterey, CA. January 23 - 25, 1990.
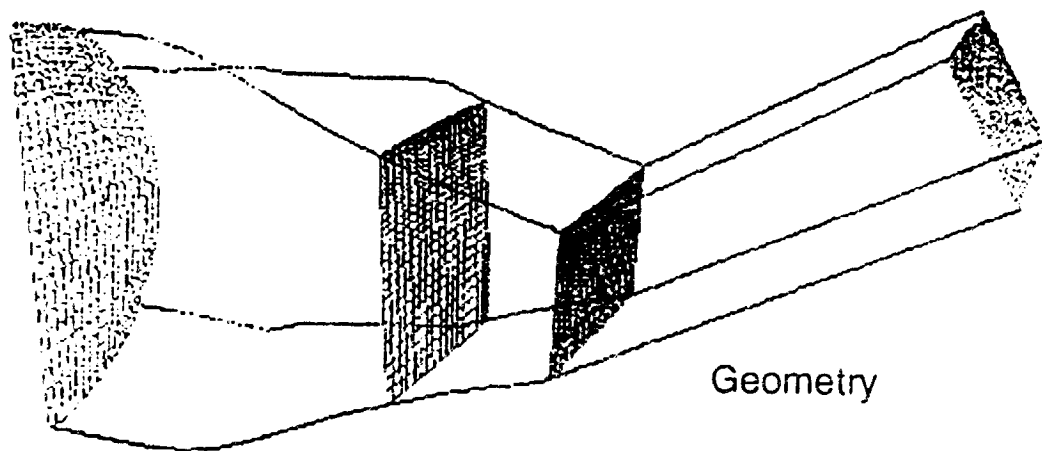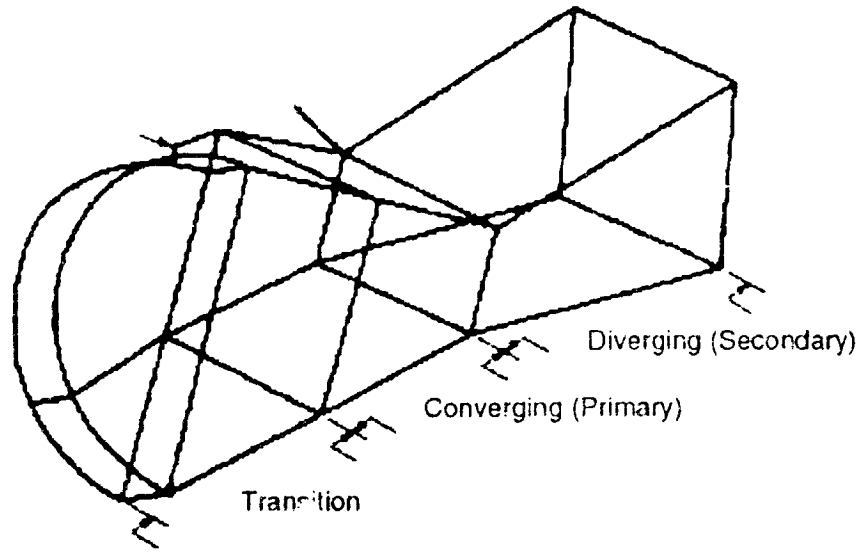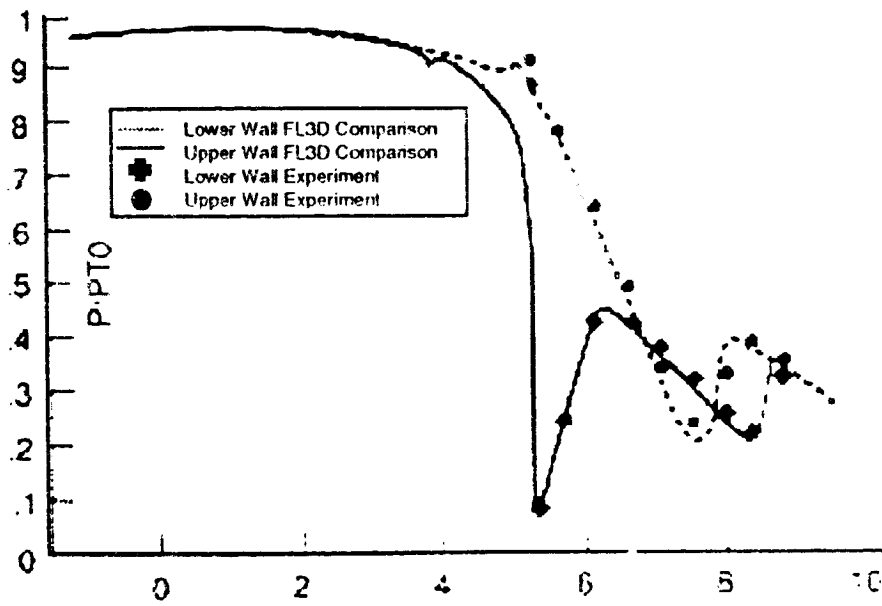
Geometry
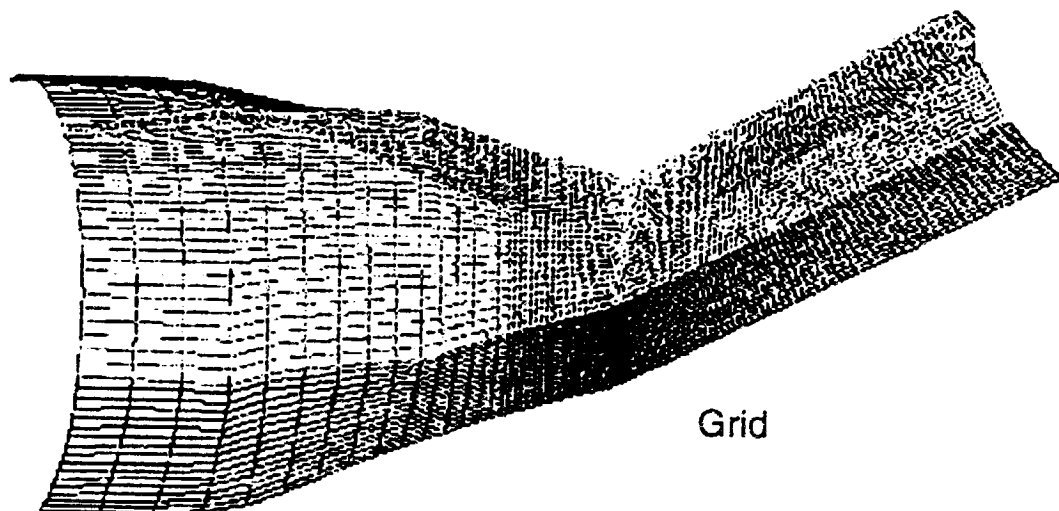
Grid
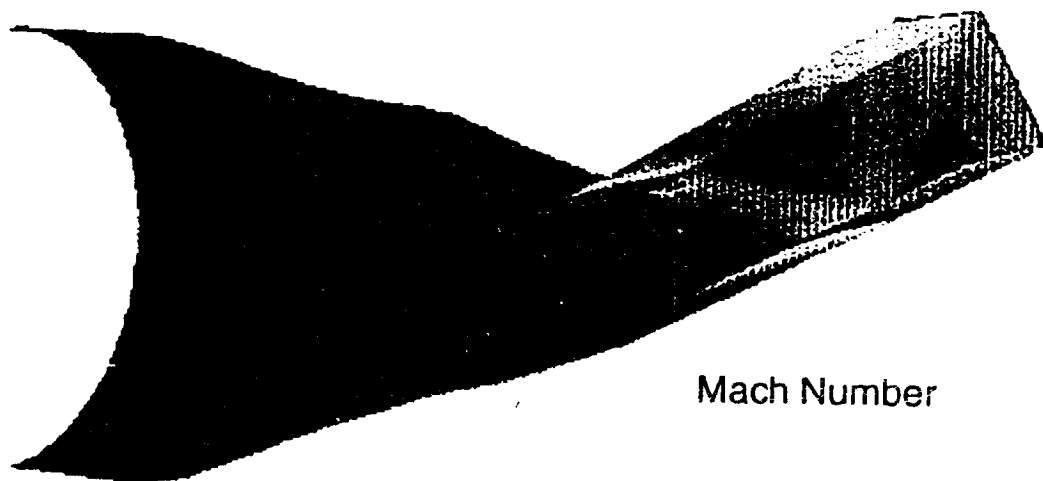
Mach Number

Figure 1. 29° vectored nozzle geometry, grid and mach number contours

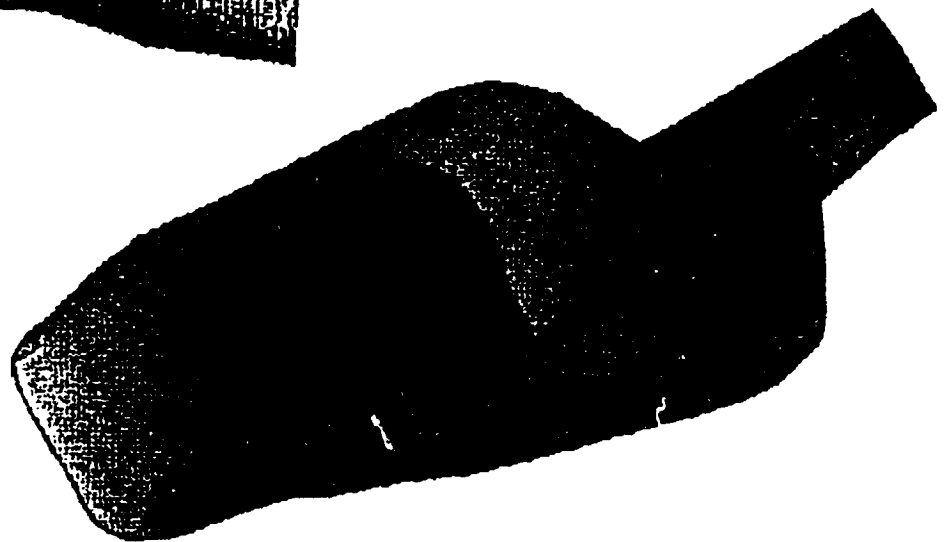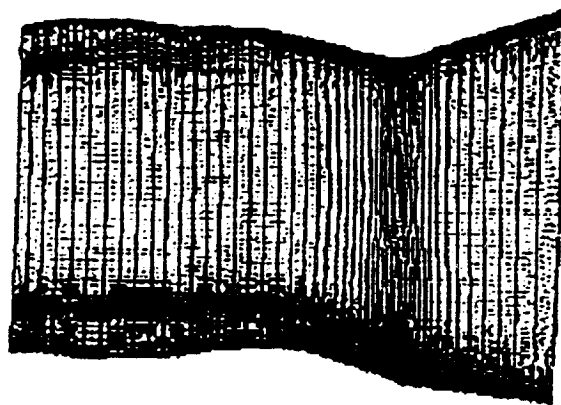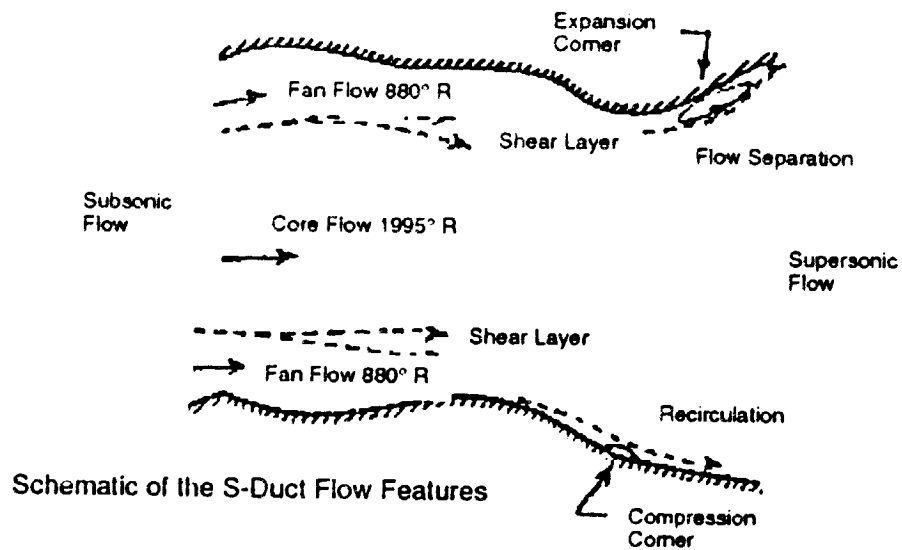3D Geometry of the 29° vectored
2DCD Nozzle with transition duct
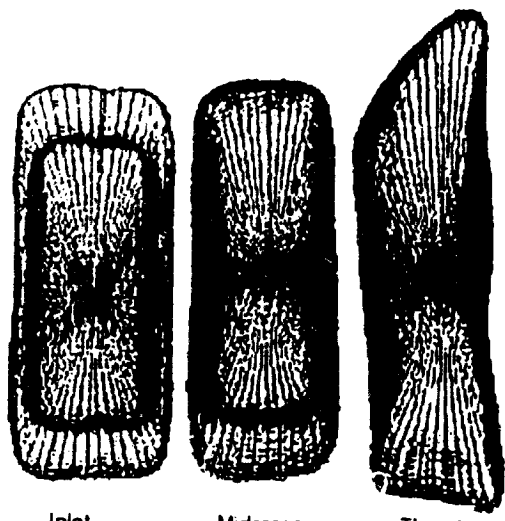

Comparison of Wall Pressure
- Experiment and FL3D Solver

Figure 2. Comparison of wall pressure distribution

Problem: Investigate mixing of subsonic primary (hot) flow with subsonic secondary (cold) flow exiting as supersonic

**Nature of the Flow:** Transonic, mixing of hot core and cold fan flow with sharp curvature

Expansion
Corner

Fan Flow 880° R

Shear Layer

Flow Separation

Subsonic
Flow

Core Flow 1995° R

Supersonic
Flow

Shear Layer

Fan Flow 880° R

Recirculation

Schematic of the S-Duct Flow Features

Compression
Corner

S-Duct Geometry and
Computational Grid in Axial Plane

Figure 3.   S-Duct grid and flow features description

Inlet   Midcross   Throat
Plane

S-Duct Geometry and Computational
Grid in Cross Plane
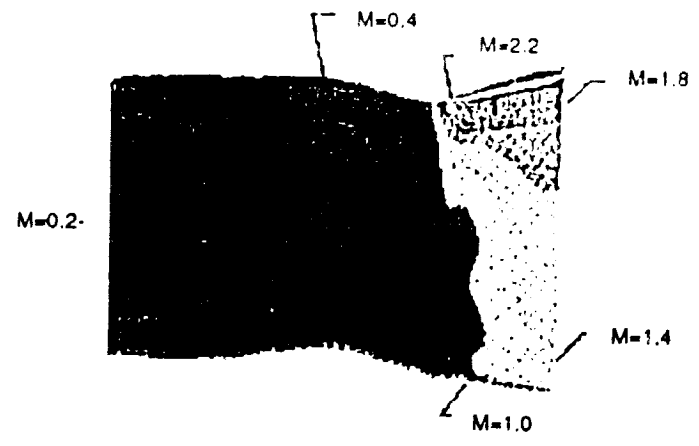
Mach No. Contours in the Axial Plane for S-Duct

T_t/T_{ref}
Blue = 0.25
Yellow = 0.6
Red = 0.7
Green = 0.5
Magenta = 0.8
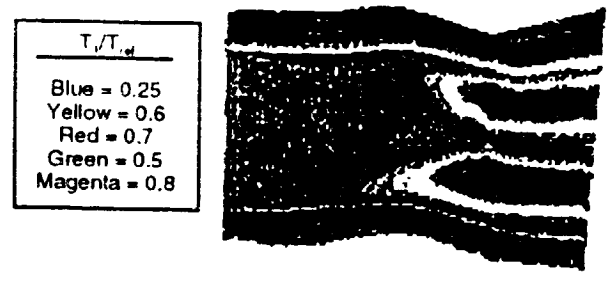
Total Temperature Distribution in the Axial Plane

T_t/T_{ref}
Blue = 0.25
Yellow = 0.6
Red = 0.7

Inlet

Midplane

Throat
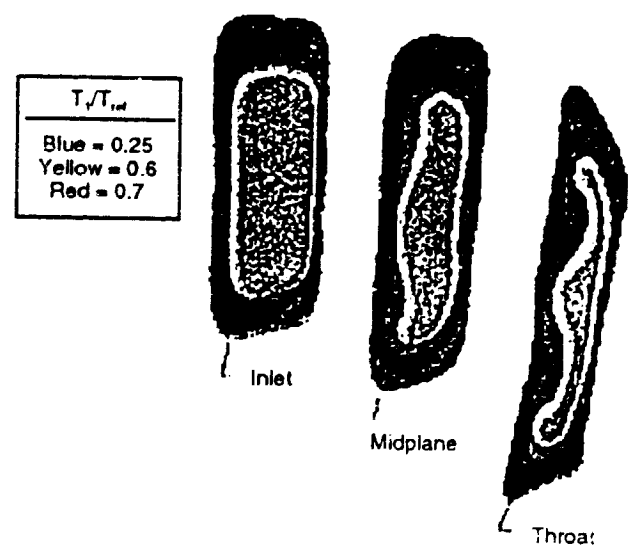
Total Temperature Distribution in the Cross Plane

Figure 4.   S-Duct Flow characteristics

Problem: Investigate the mixing of supersonic flow with a subsonic film at one wall

Grid for Geometry 2 (63*63)

31.4"

0.45"

2.288"   2.434"   2.894"

Temperature Contours

8.0"

Splitter Plate Thickness = .01"
Geometry 1
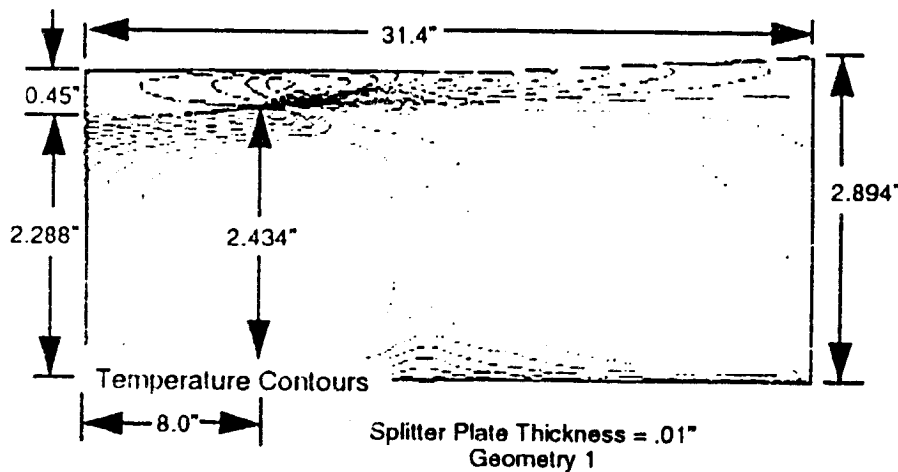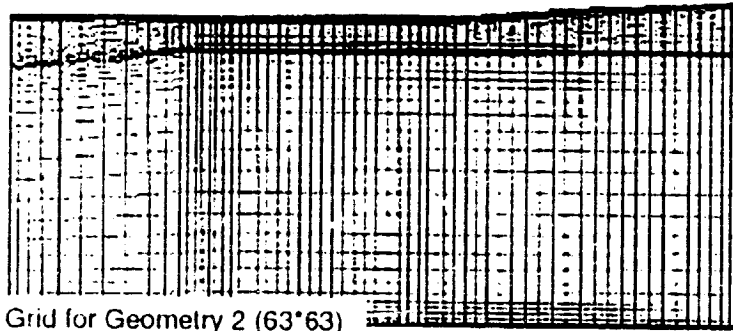
	Primary	Secondary
Ptotal	72.348	46.24
Ttotal °F	451.6	65.7
Flow Rate	10.056	1.471
Mach No.	1.0	0.661

Experiment
Computations (Geometry 1)
Computations (Geometry 2)

T/T_{ref}

X inches

Top Wall Pressure Comparison

Experiment
Computations (Geometry 1)
Computations (Geometry 2)

T/T_{ref}

X inches

Top Wall Temperature Comparison
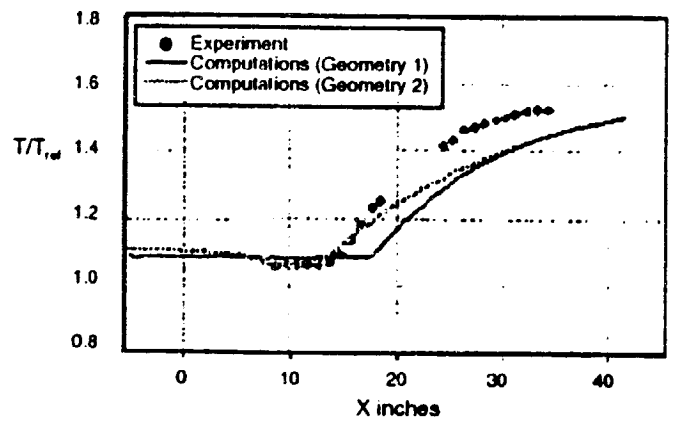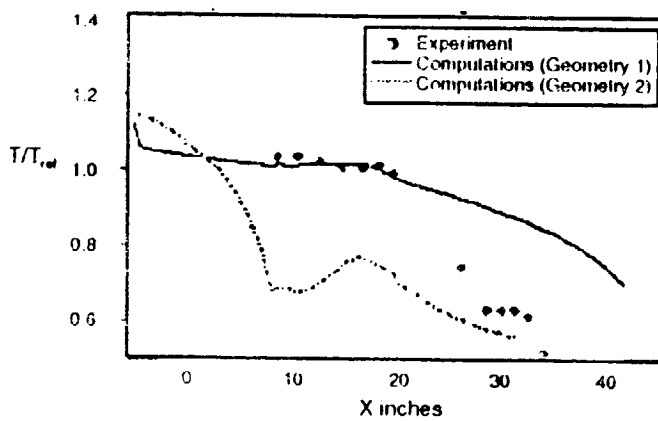
Figure 5.   Mixing characteristics of supersonic and subsonic flows

Problem: Supersonic flow solution with center body

Nature of the Flow: Transonic

Geometry

Subsonic region
curvature effect

$m_{ext} = 2.0$

Mach Number
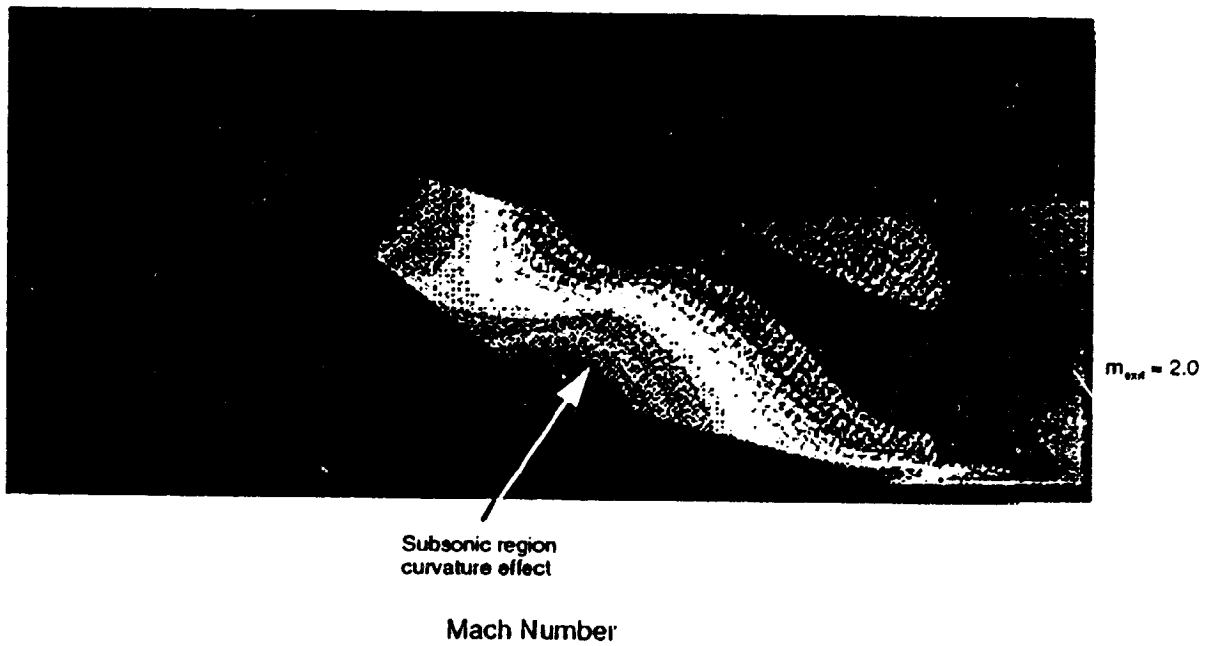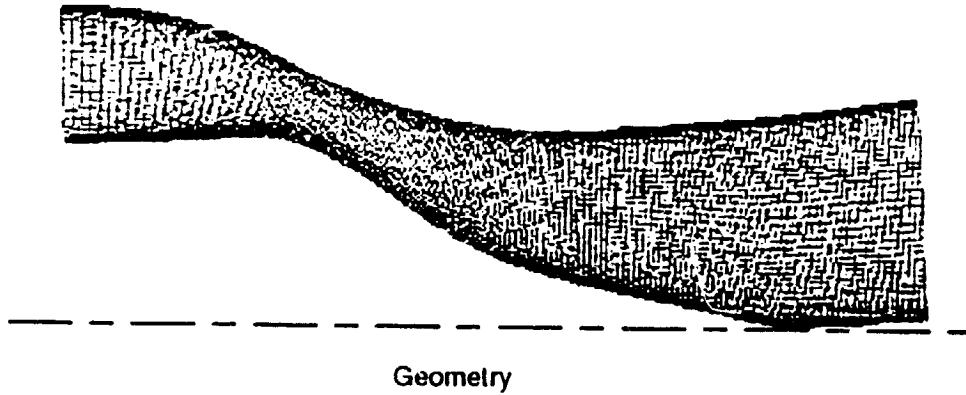
Figure 6. Supersonic nozzle flow and geometry

Problem: Investigate the flow properties from an over-expanded supersonic nozzle

Nature of the Flow: Over expanded supersonic flow at 0.9 external mach

$P = P_{amb}$
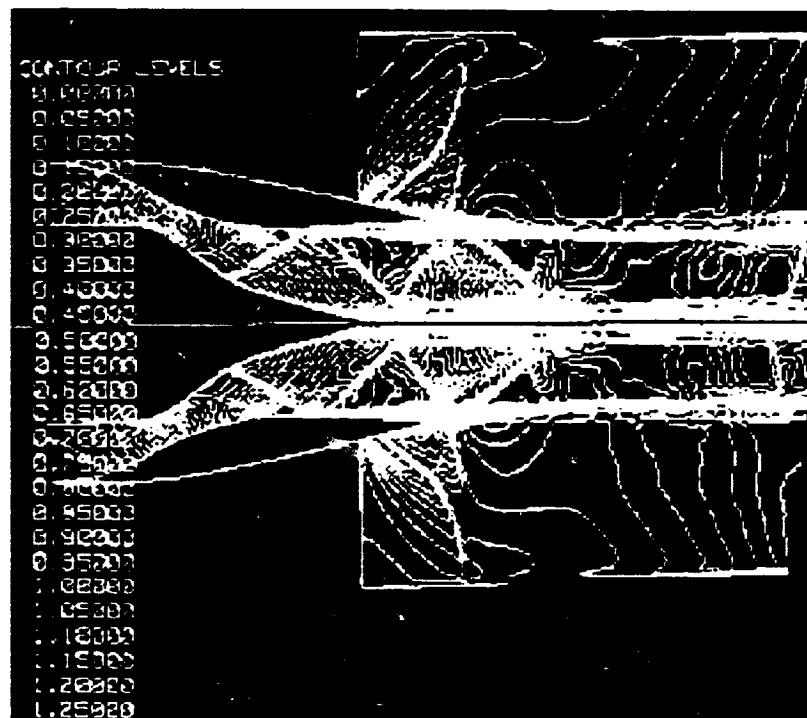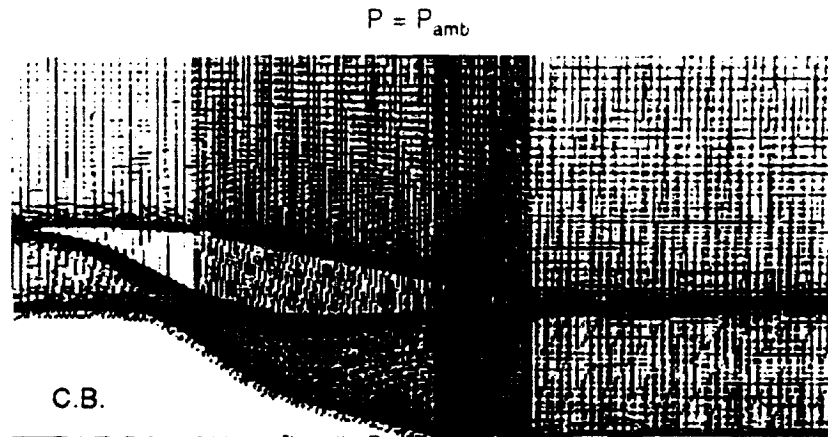
Figure 7. Over expanded nozzle flow

$M_{exit} = 2.0$ $T_{tjet} = 1260°\ R$ $Dia_{jet} = 1.15in$

Npr = 8.0   **Fully Expanded**
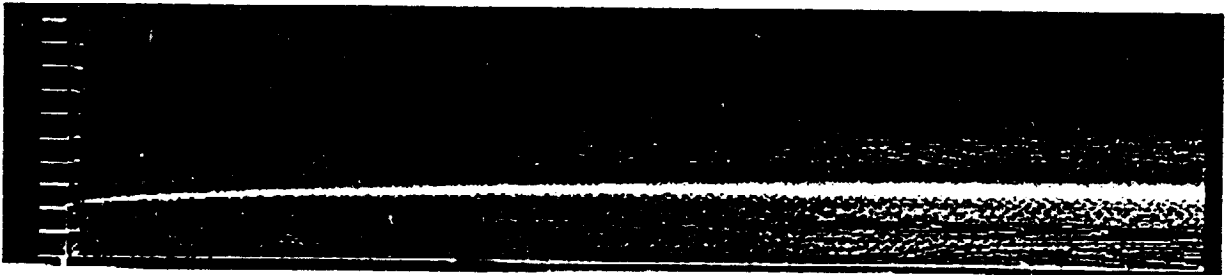
                              Under Expanded

Npr = 9.82
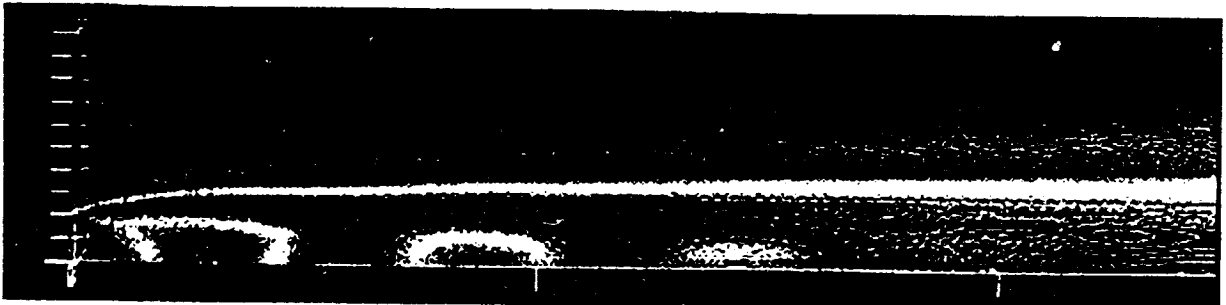
Figure 9:   Supersonic plume characteristics

Problem: Estimate the plume characteristics of a supersonic jet

Nature of the Flow: Fully expanded and under expanded plumes

Fully-Expanded Turbulent Jet Plume Flow
Mach Number Along the Cener Line

Under-Expanded Turbulent Jet Plume Flow
Mach Number Along the Cener Line
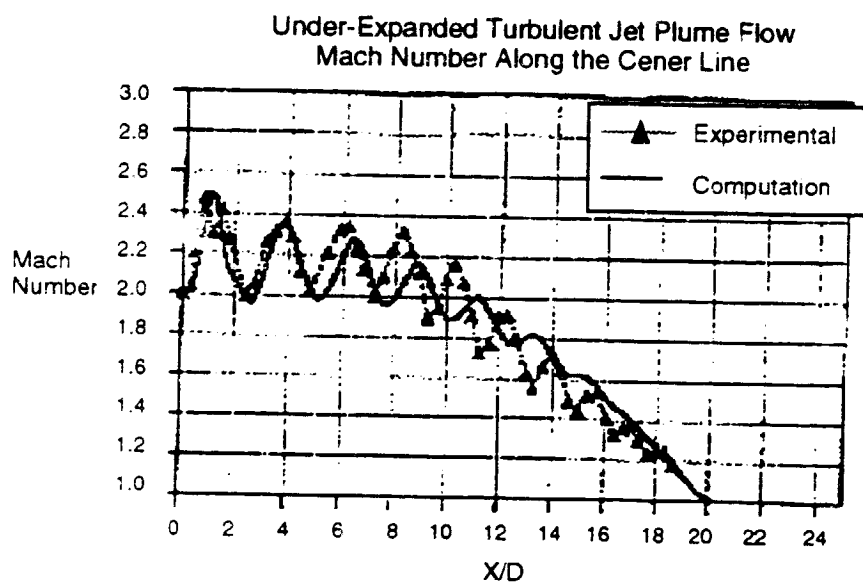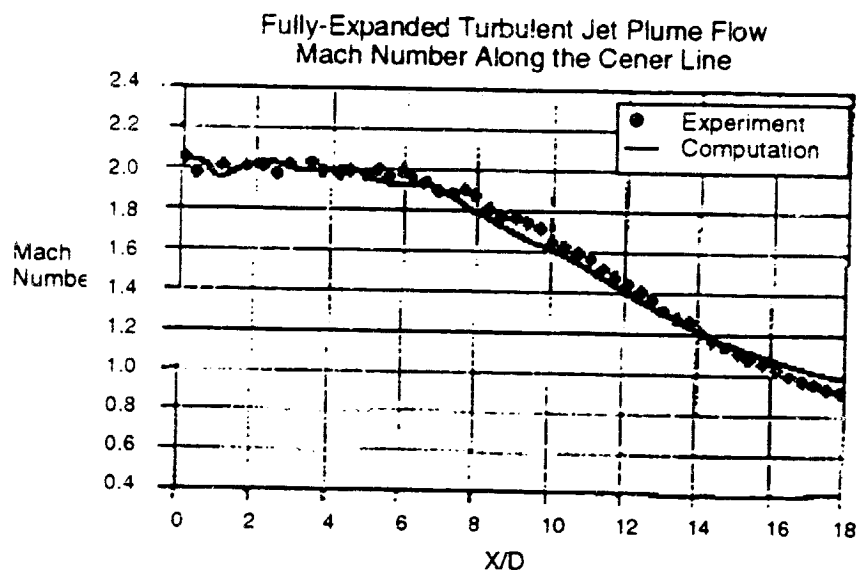
Figure 10: Supersonic plumes - comparing centerline characteristics

AIAA 94-0019

COMPUTATIONAL ANALYSIS OF A 2DCD NOZZLE FLOW WITH THE FL3D SOLVER

C. R. Bobba,
R. K. Rowe and R. K. Rout
GE Aircraft Engines
Cincinnati, OH.
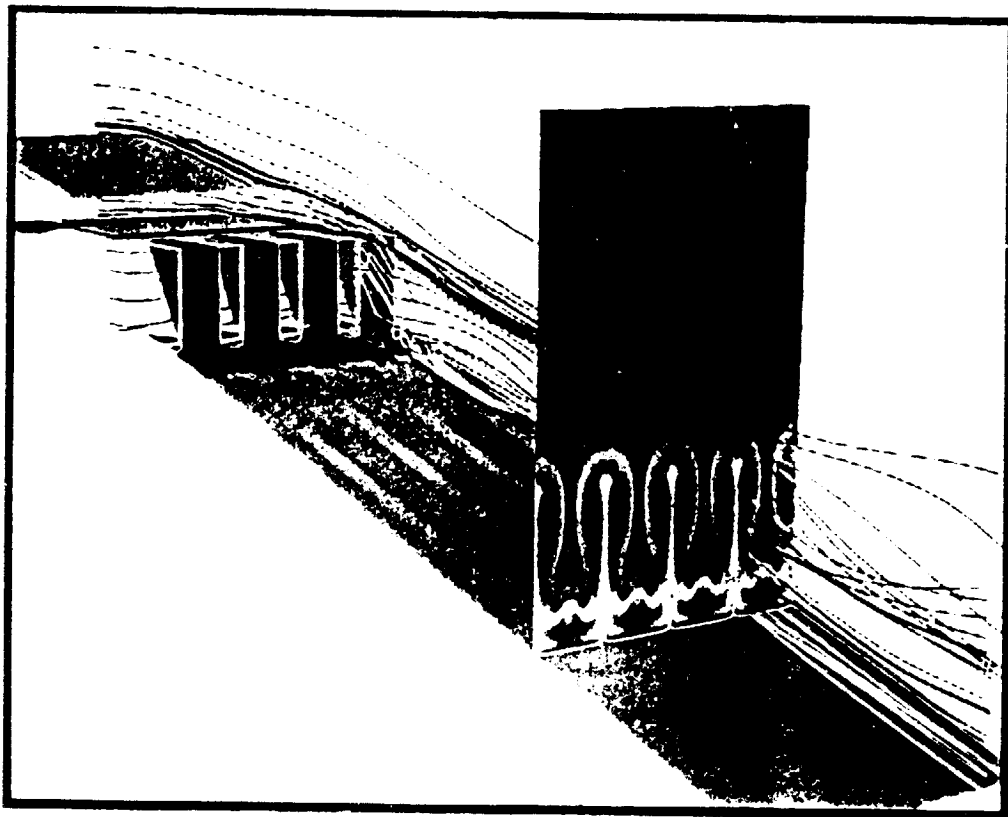
E. Venkatapathy,

Eloret Institute
Palo Alto, CA.

32nd Aerospace Sciences Meeting & Exhibit
January 10-13, 1994 / Reno, NV

COMPUTATIONAL ANALYSIS OF A 2DCD
NOZZLE FLOW WITH THE FL3D SOLVER

Choudary R. Bobba, Senior Engineer[†]
R. Kevin Rowe, Staff Engineer[†]
and
R. K. Rout, Senior Engineer[††]

General Electric Aircraft Engines
Cincinnatti, Ohio, 45215

Ethiraj Venkatapathy, Scientist[†]*

*Eloret Institute, 3788 Fabian Way,
Palo Alto, California 94303*

ABSTRACT

A two-dimensional, convergent-divergent (2DCD) exhaust system has been analyzed with the FL3D Navier-Stokes flow solver. The nozzle incorporated a chute suppressor system at the exit of the core flowpath for noise abatement at takeoff. Results show an extremely three dimensional flowfield with very complex flow structures. The computed solution was compared to limited experimental test data. In general, the predicted pressure distributions matched well with test data. The predicted flowfield captured the important flow-features observed during testing and from shadowgraph pictures. The computational results have enhanced the understanding of this type of complex nozzle flow and can be used in improving its design.

INTRODUCTION

Recent studies have predicted a 400 percent increase in commercial transpacific air travel and a doubling of transatlantic trips by the year 2000. These studies have shown a sizable market potential for a civil aircraft which would significantly reduce the time to fly these transcontinental routes. An aircraft that cruises at over twice the speed of sound will cut the time to fly from Los Angeles to Tokyo from 10 hours to about 4 hours. In a world that is truly becoming "globalized", this time savings is very attractive.

One of the challenges to high speed aircraft systems is designing an engine system which meets or exceeds civil noise requirements. During takeoff and climb, the dominant noise source emanates from the engines. Typical military engines for supersonic flight incorporate low bypass, high specific thrust turbofan systems. As such, these systems generate high exit velocities to meet thrust requirements. These high exit velocities in turn generate high levels of noise which are unacceptable in a civil aircraft. In order to lower the noise levels resulting from these engine systems, exhaust nozzles which entrain ambient air into the nozzle are a prime candidate for this aircraft[1 - 10]. The entrainment and mixing of this ambient air with the engine core flow lowers the exit velocity while maintaining the thrust at required levels.

This paper presents a computational study performed to evaluate one of these mixer nozzle candidates. The FL3D

flow solver from NASA Ames Research Center was used for this analysis. As will be described in more detail later in the paper, FL3D is a three-dimensional (3D) full Navier-Stokes computational fluid dynamics (CFD) solver. The main purpose of this study was to better understand the flow physics of this nozzle design while validating FL3D for these type of systems. The results of the analysis are compared to a limited amount of test data and several interesting characteristics of the nozzle flowfield are discussed.

2DCD NOZZLE GEOMETRY

The nozzle analyzed in this study is shown schematically in Figure 1. It is a two-dimensional (2D) wedge nozzle with a lobed mixer located in the primary stream. A similar nozzle was designed and tested by Harrington, et al.[1] The unique feature of this nozzle is the addition of a secondary or bypass stream to further attenuate jet noise.

The mixer rack consists of five mixer chutes located at equal spanwise distances apart. As can be seen in Figure 1, the chute entrance angle is relatively steep (55 degrees). This was dictated by the need to stow these chutes inside the wedge at cruise conditions. The primary flow flowpath through the mixer is convergent, resulting in the primary stream throat being located at the mixer exit. At the exit of the mixer (i.e. the mixing plane) the secondary duct area is 1.5 times the primary duct area.

The nozzle has a straight wedge with a 15 degree half angle. The sidewalls for the secondary duct terminate at the secondary nozzle exit. The sidewalls for the primary duct

terminate at the mixing plane. The secondary flowpath is a convergent nozzle with the throat at the exit plane.

The spanwise computational domain for this analysis (shown in Figure 2) consisted of a section of the total nozzle geometry extending from the centerline of a primary chute to the centerline of a secondary chute The top-to-bottom computational domain extended from a farfield freestream boundary to the nozzle centerline.

GEOMETRY MODELING USING I-DEAS

Since the nozzle geometry is highly three-dimensional an advanced CAE package called I-DEAS (Integrated Design Engineering and Analysis Software) was used to create the geometry model and the computational grid for the flow analysis. The nozzle geometry is generated using a building block approach provided in the I-DEAS solid modeling environment. At first the chute geometry is built using the cross sectional definition and invoking the 'sinking operation'. Then a thickness is added to the inner chute surface to generate the actual chute geometry with variable thickness from top to the bottom of the chute. Then the single chute is replicated to give a series of chutes that represent the true chute configuration in the nozzle.

The nozzle flow domain without the chutes being two dimensional, was created using the outline of the inner and outer boundaries only. The chute is then located in this domain in its proper orientation and location to generate the divided flow path for the core and the fan flow. The most important information in this operation is the three dimensional intersection of the plug boundary with the chute boundary at its bottom. This information is automatically obtained from I-DEAS when the chute is located on to the plug surface. The 3-D surface information and the outer flow boundaries are then transferred directly to the grid generator for creating suitable grid for the flow analysis.

COMPUTATIONAL GRID

Since the geometry is complex with immersed bodies and wall boundaries in the flow field, a suitable block structure was designed to accommodate these complexities in the flow domain. The block structure is also designed such that a better control of grid in terms of quality as well as quantity could be achieved in the flow domain. A schematic of the grid blocks generated is presented in Figure 3. The blocks are generated using the block structure option available in I-DEAS grid generation module. This block structure algorithm through data base management system keeps track of the block interface connectivity between two different blocks as well as the surface interface connectivity of a single block. This feature automatically allows the same number of grid points and the function continuity along the interface between the blocks. The grid is generated in these individual blocks first and then merged to form a single structured grid. Figure 4 shows the computational grid in the chute-symmetry plane. A finer grid distribution is

provided where ever there is a solid boundary to resolve the viscous layer near the wall. The grid was clustered in the streamwise direction where ever large gradients are expected in the flow field such as the region close to the exit plane of the primary nozzle.

RESULTS AND DISSCUSSION

An algebraic turbulence model based on a Baldwin-Lomax formulation has been used with the FL3D flow solver for the results presented in this paper. The length scales are deduced from the grid normal distances from the wall, and the velocity scales are estimated from the vorticity distribution in the flowfield. The results presented were computed both with laminar as well as with turbulent viscosity. The influence of turbulence on the pressure distribution on various surfaces of the geometry is explored. The changes in the flowfield from the core center plane to the chute center plane are presented. The interaction of the core flow with the secondary flow and its impact on the separation characteristics of the flow on the centerbody is investigated. The estimated pressure distributions are compared with measured data where available. Qualitative comparisons of computed flow characteristics with shadowgraph measurements are also shown in this paper.

FLOW ORIENTATION

The flow orientation presented earlier in the paper is briefly re-stated here. The computational domain consists of three different flows. They are : (1) Primary flow, (2) Secondary Flow and (3) Freestream flow. These flows are separated by solid walls up to the nozzle exits. Downstream of the nozzle exits, they are free to interact with each other. The physical orientation of the 2DCD nozzle geometry and the flow are shown in Figure 1. The flow conditions used in this study are:

$$\text{Primary Pressure Ratio } (P_{T_{prime}}/P_{amb}) = 3.2$$

$$\text{Secondary Pressure Ratio } (P_{T_{sec}}/P_{amb}) = 2.2$$

$$\text{Freestream Mach number } = 0.2$$

The primary flow accelerates to supersonic speeds as it negotiates through the passage between the chutes. As such, the pressure of the primary flow at the mixer chute exit is dictated by the area ratio of the primary chute flowpath. However, at the end of the mixer chute, the flow exits to ambient conditions and must adjust accordingly.

The secondary flow exits the nozzle at supersonic speeds just upstream of the mixer chute leading edge. The flow is then split into two regimes. Some of the flow is free to flow down the chutes and mix with the primary flow in the adjacent mixer chutes. The remaining flow continues over the top of the primary chutes where it forms a stratified layer over the primary flow. The freestream flow is able to interact with the secondary and primary flows downstream of the secondary nozzle exit.

led to a large scale flow separation on the wedge surface, and separation of the secondary flow in the mixer chutes. The turbulent flow results agreed well with available surface static pressure measurements and with shadowgraph pictures of the flowfield. The CFD results have provided a good understanding of the flow phenomenon in these type of nozzles and will aid in improving its design.

ACKNOWLEDGEMENTS

REFERENCES

[1] Harrington, D.E., Schloemer, J.J., Skebe, S.A., "Thrust Performance Of Isolated, Two-Dimensional Suppressed Plug Nozzles With And Without Ejectors At Mach Numbers From 0 to 0.45", NASA TM X-3384, May 1976.

[2] Bevliaqua, P.M., "Evaluation of Hypermixing for Thrust Augmenting Ejec- tors," Journal of Aircraft, Vol. 11, 1974.

[3] Bevliaqua, P.M., "Analytical Description of Hypermixing and Test of an Improved Nozzle," Journal of Aircraft, Vol. 13, 1976.

[4] Paynter, G.C., Birch, S.C. Spalcing, D.B. and Tatchell, D.G., "An Experimental and Numerical Study of a 3-D Mixing Flows of a Turbofan Engine Exhaust System," AIAA Paper 77-204, Jan. 1977.

[5] Press, W.M., Morin, B.L. and Gousy, R.G., "Forced Mixer Lobes in Ejector Designs," Journal of Propulsion and Power, Vol. 4, No. 4, July-Aug 1988.

[6] Patterson, R.W., "Turbofan Mixer Nozzle Flow Field - A Benchmark Experimental Study," Journal of Engineering for Gas Turbine and Power, Vol. 106, July 1984.

[7] Tillman, T.G., Patrick, W.P. and Patterson, R.W., "Enhanced Mixing of Supersonic Jets," AIAA paper 88-3022, 1988.

[8] Tillman, T.G. and Patterson, R.W., "Supersonic Nozzle Mixer Ejector," AIAA paper 89-2925, 1989.

[9] Lord, W.K., Jones, C.W., Stern, A.M. Head, V.L., and Krejsa, E.A., "Mixer-Ejector Nozzle for Jet Noise Suppression," AIAA paper 90-1909, 1990.

[10] DeBonis, J.R., "Full Navier-Stokes Analysis of Two-Dimensional Mixer/Ejector Nozzle for Noise Suppression," NASA TM 105715, 1992 (also AIAA 92-3570, 1992).

[11] Venkatapathy, E., Feiereisen, W.J., and Obayashi, S., "Compuatational Studies of Hard Body and 3-D Effects in Plume Flows," AIAA paper 89-0129, 1991.

[12] Venkatapathy, E., and Feiereisen, W.J., "Computational Analysis of Plume Induced Separation," AIAA paper 91-0711, 1991.

[13] Ruffin, S.M., Venkatapathy, E., Lee, S.H., Keener, E.R., and Spaid, F.W., "Hypersonic Single Expansion Ramp Nozzle Simulations, " Journal of Spacecrafts and Rockets, Vol., 29, No. 6, 1992.

[14] Davies, C.B., and Ventkatapathy, E., "Application of a Solution Adaptive Grid Scheme to Complex Three-Dimensional Flows," AIAA Journal, Vol. 30, No. 9, September 1992.
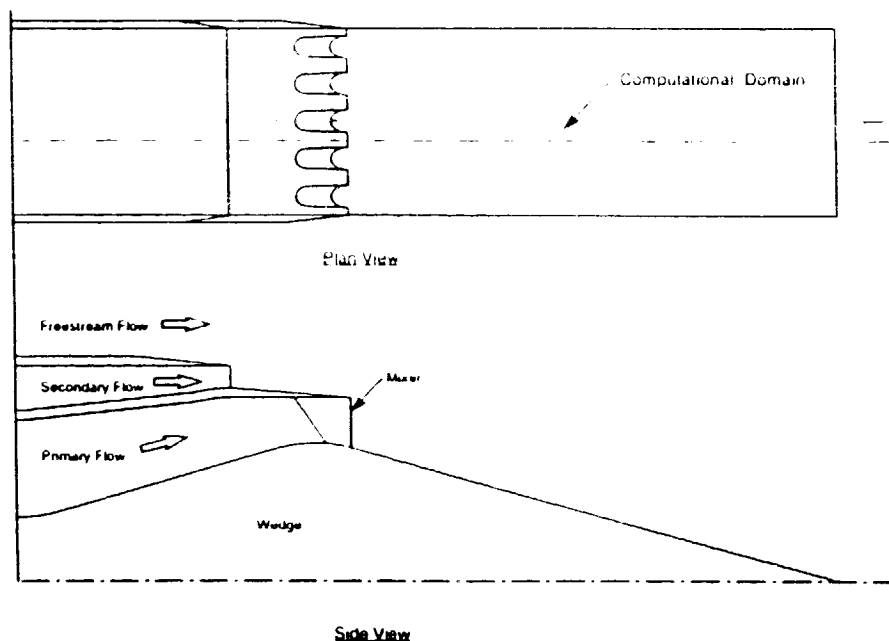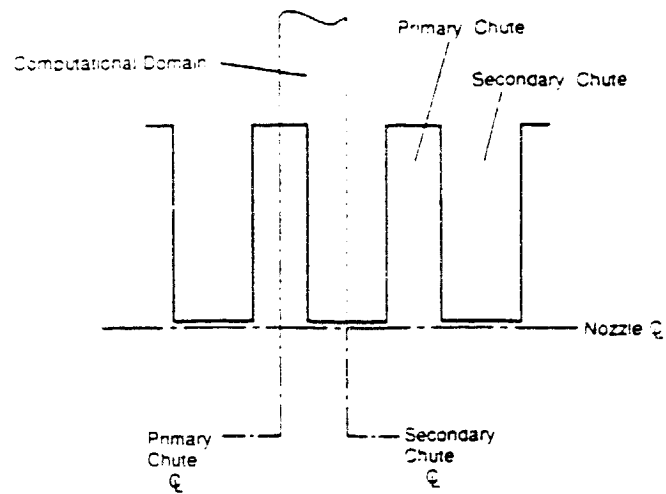

Figure 1. Schematic Of 2DCD Nozzle Geometry

Figure 2. Schematic of the computational domain at the mixer exit.
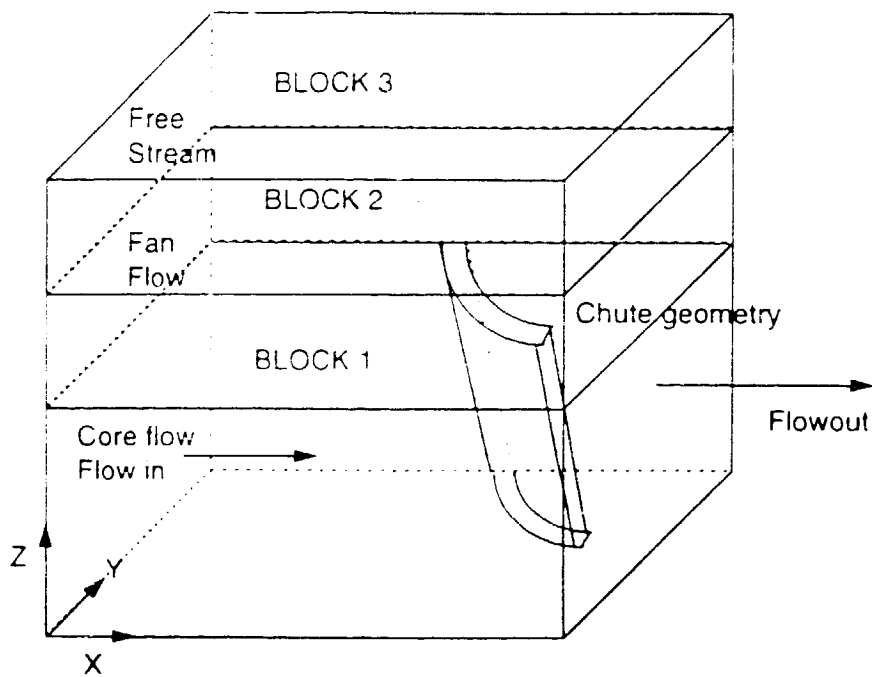

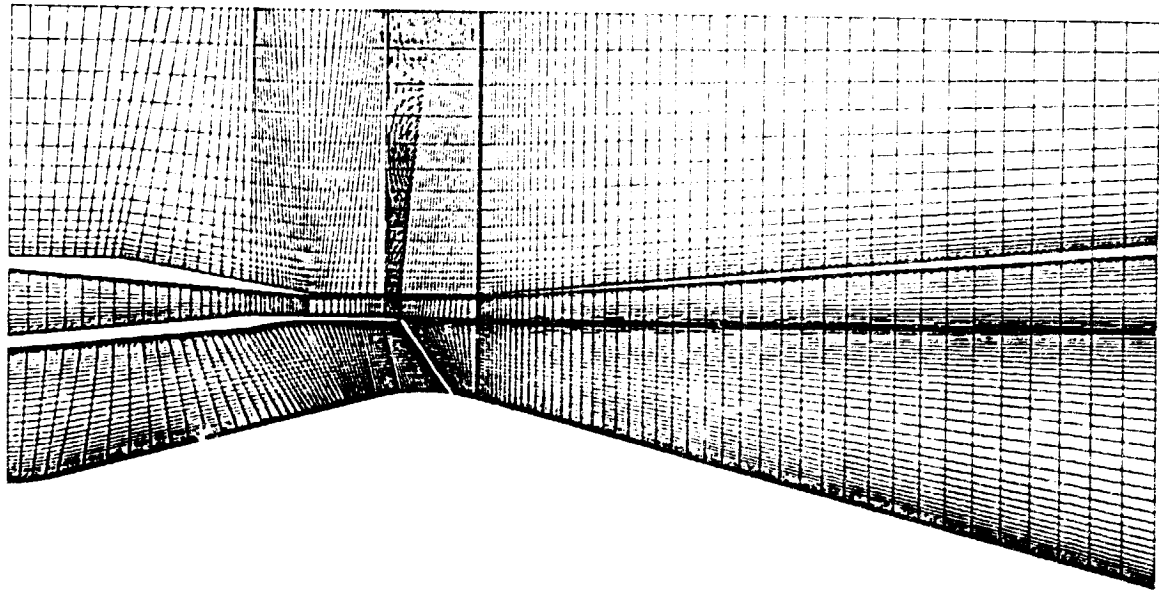Figure 3. Block structure representation for the computational grid.

Figure 4. Computational grid in the chute-symmetry plane.

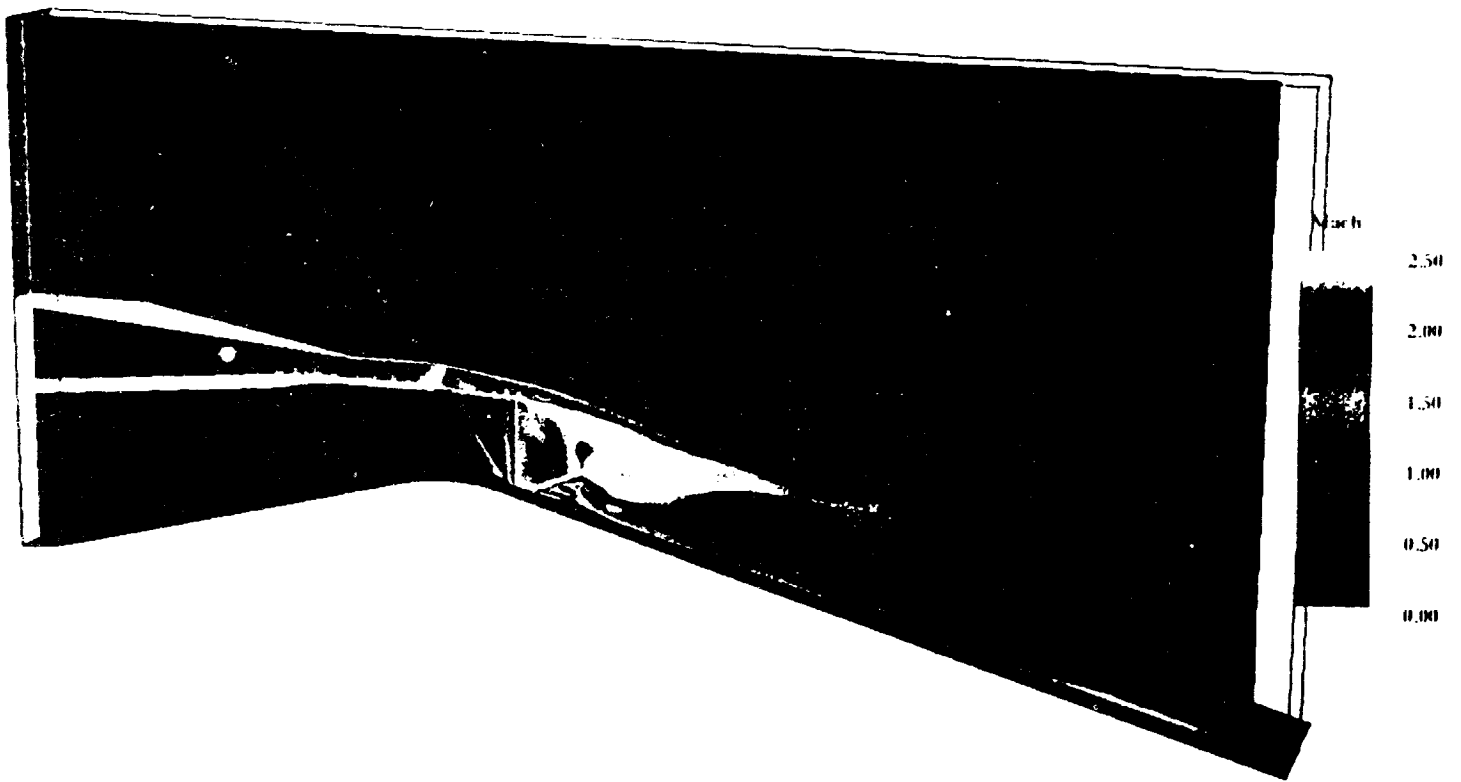Figure 5. Computed Mach number contours - core-symmetry plane.

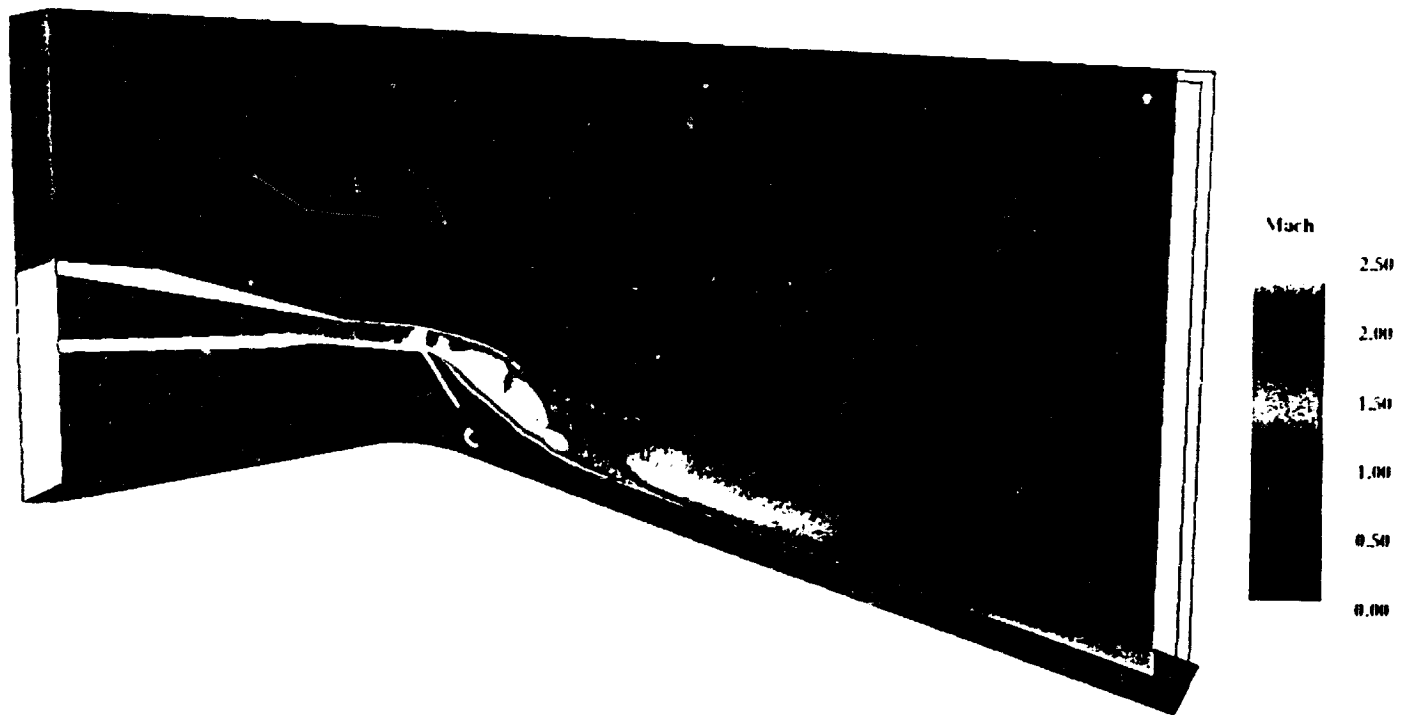Figure 6. Computed Mach number contours - mid plane.

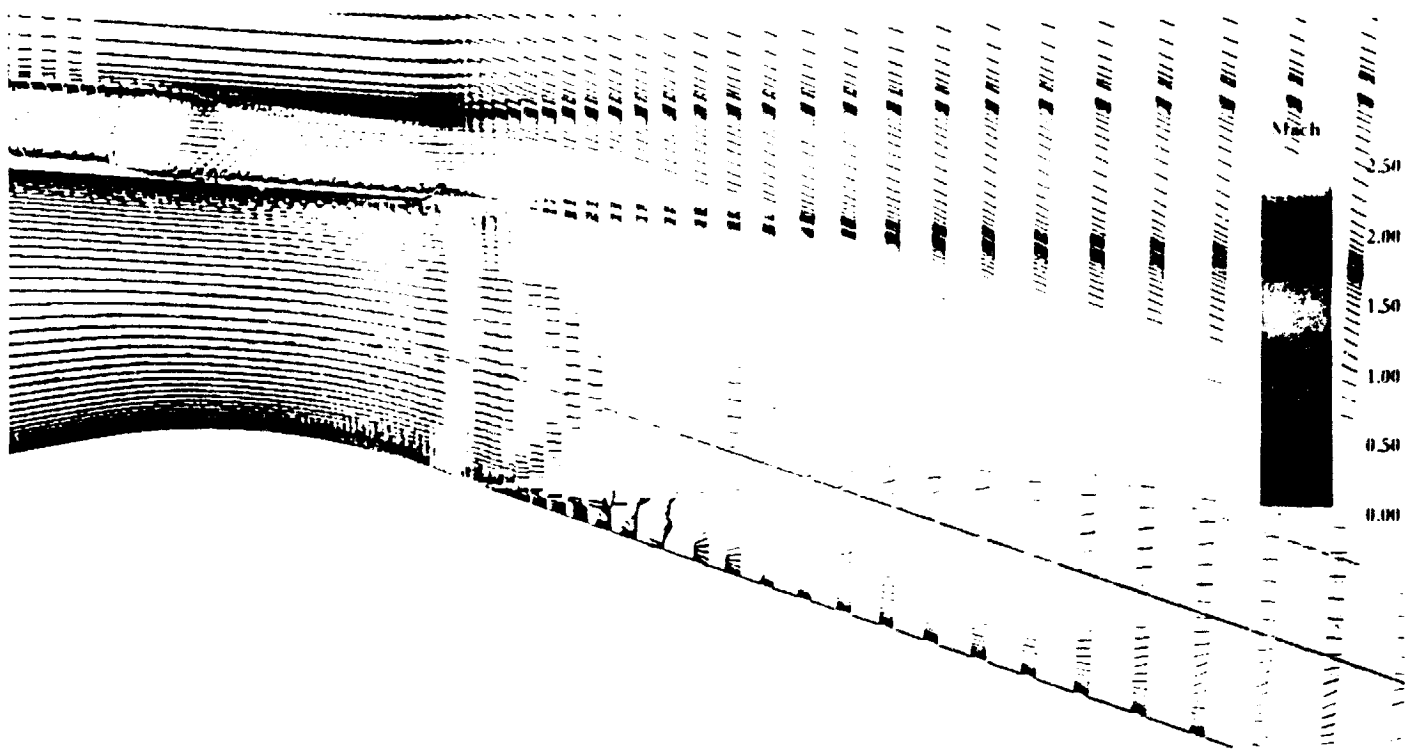Figure 7. Computed Mach number contours - chute-symmetry plane.

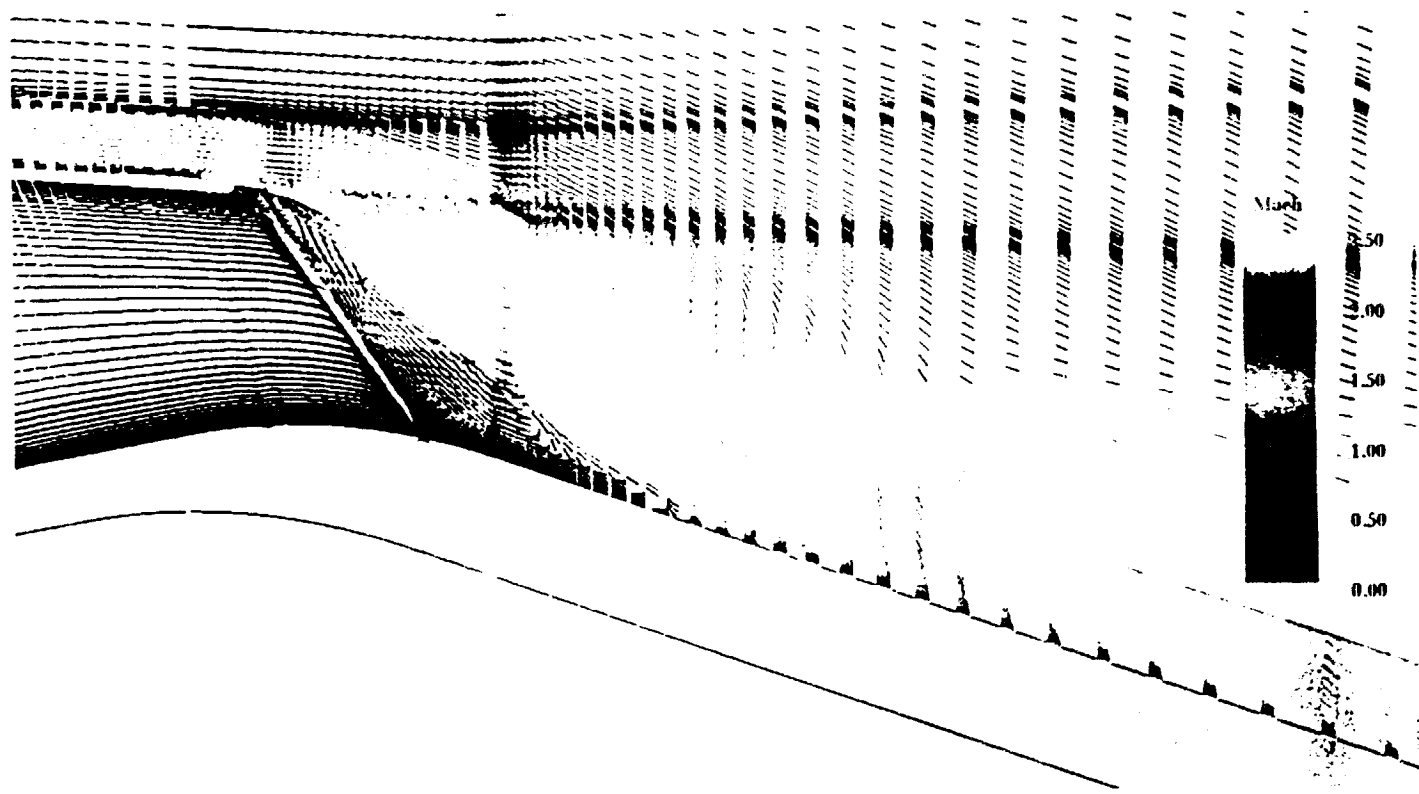Figure 8. Computed velocity vector direction - core-symmtery plane.

Figure 9. Computed velocity vector direction - chute-symmtery plane.

Particle Traces

Particles Released From Core Region
Particles Released From Flade Region
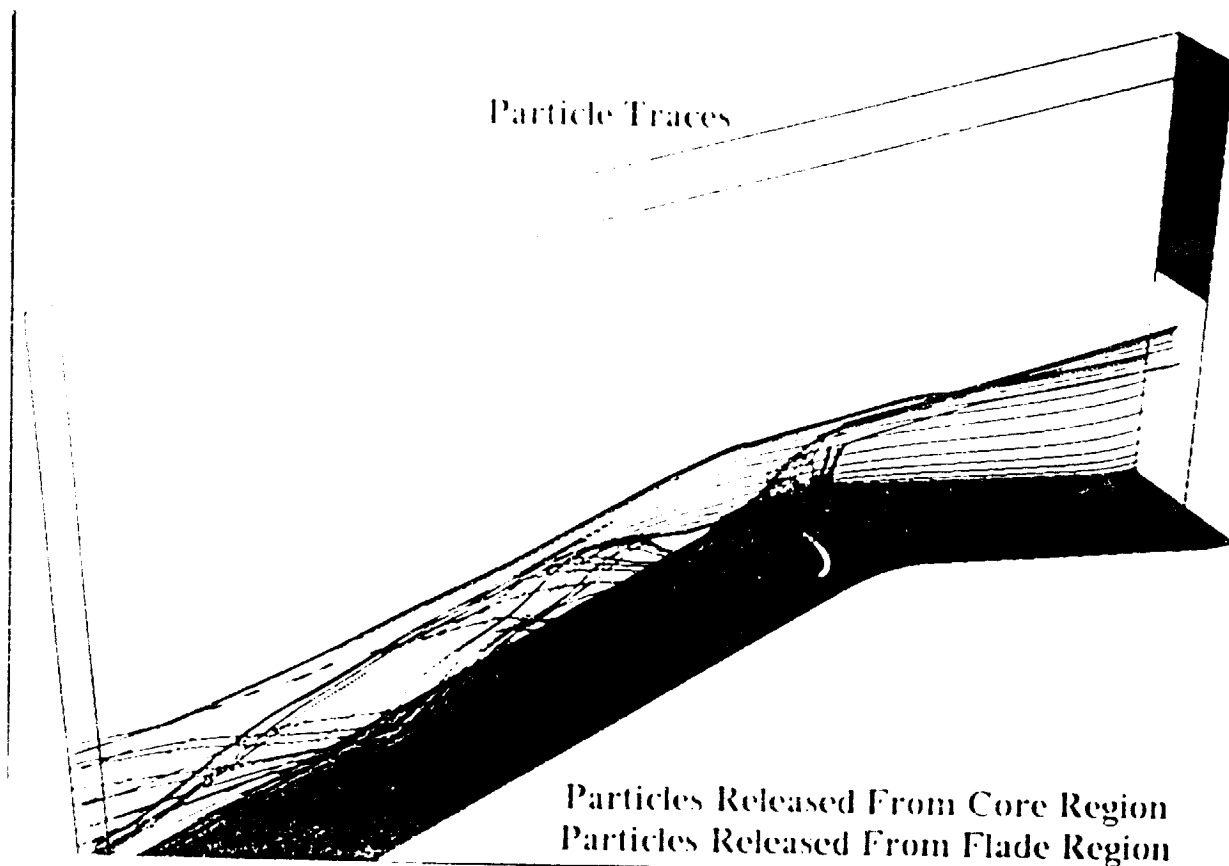
Figure 10. Particle traces from core and fan flow regions.
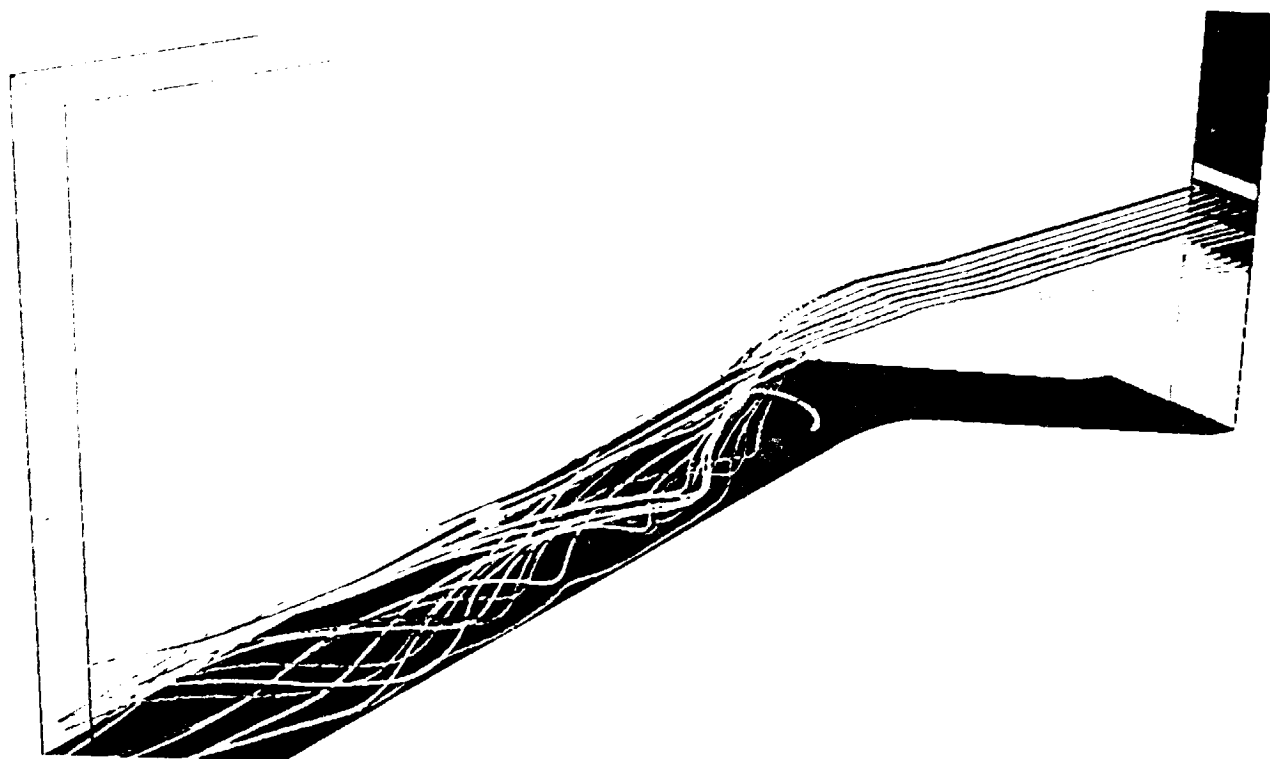
Figure 11. Particle traces from fan flow region alone.
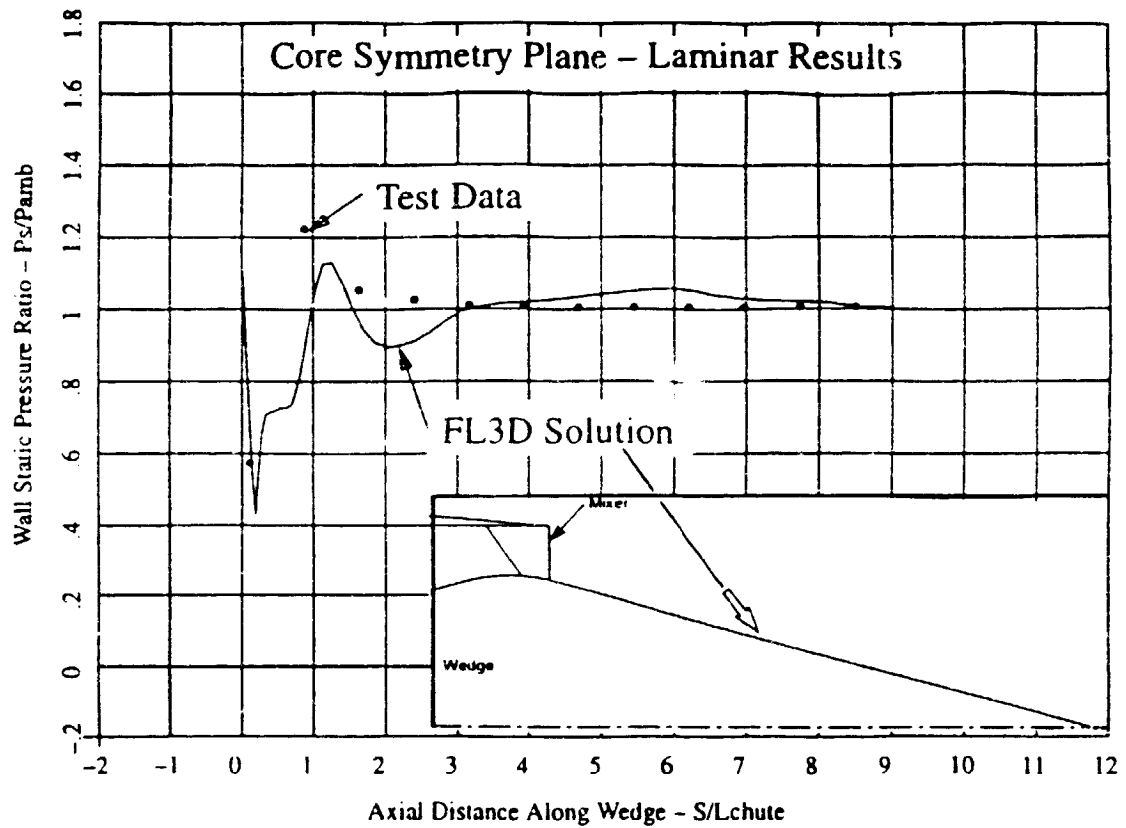
Figure 12. Pressure distribution comparison along the wedge (ramp) wall
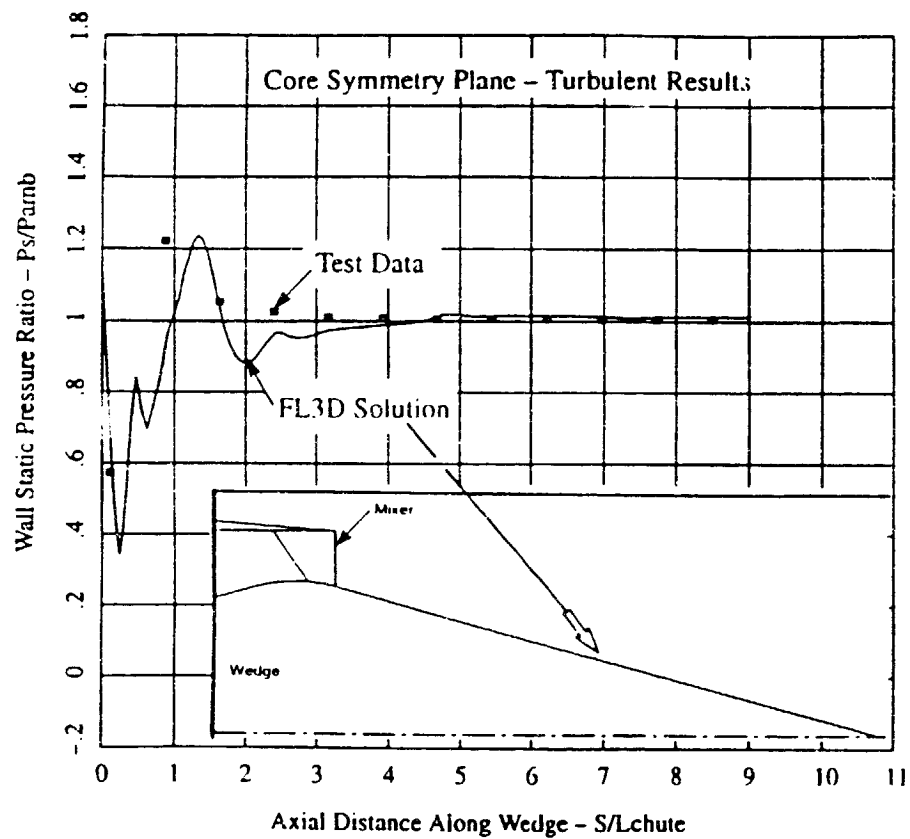- laminar computations.

Figure 13. Pressure distribution comparison along wedge wall
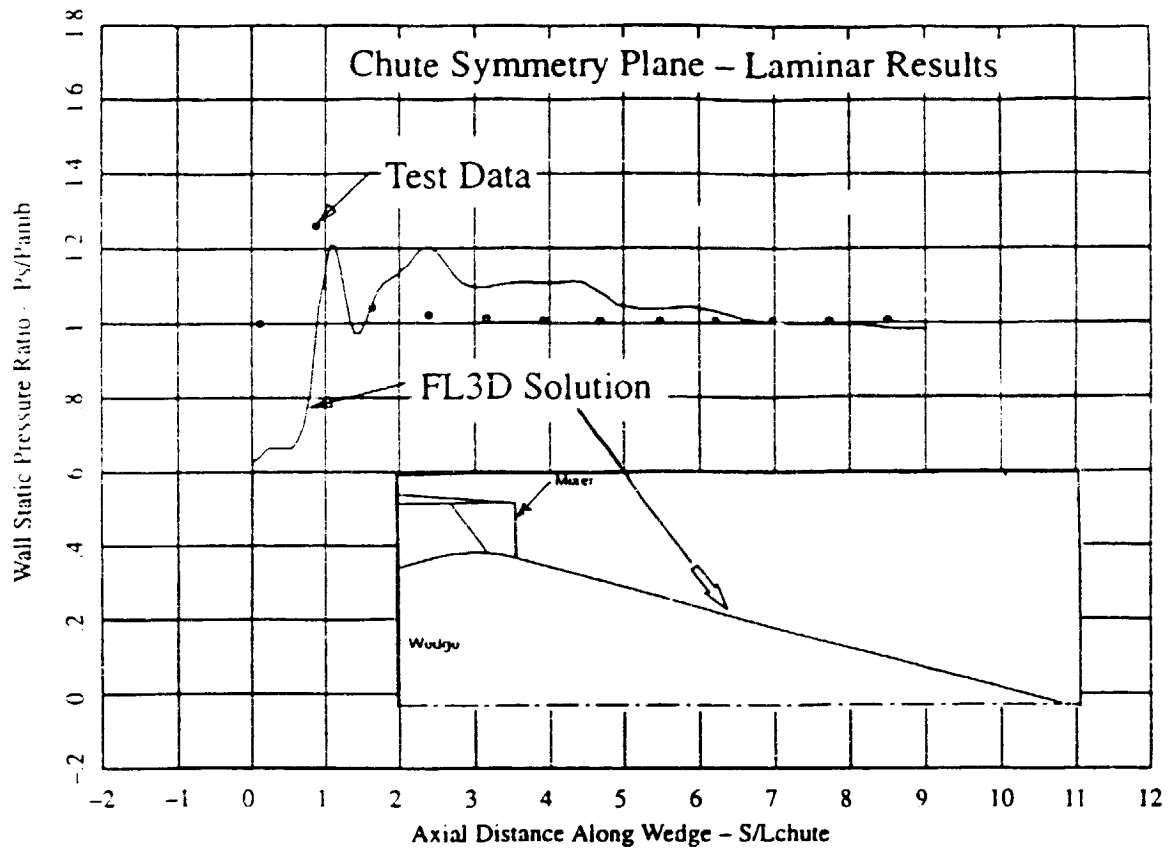- turbulent computations.

Figure 14. Pressure distribution comparison along the wedge (ramp) wall
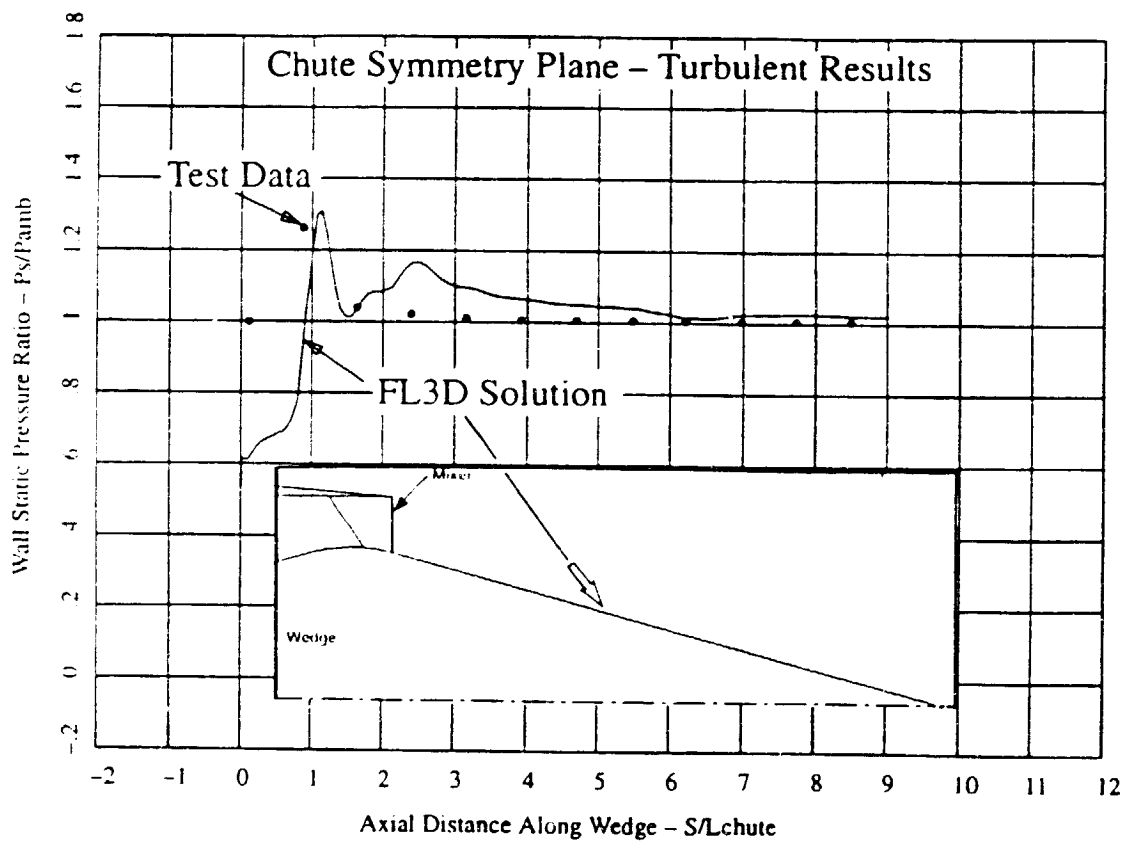- laminar computations.

Figure 15. Pressure distribution comparison along wedge wall
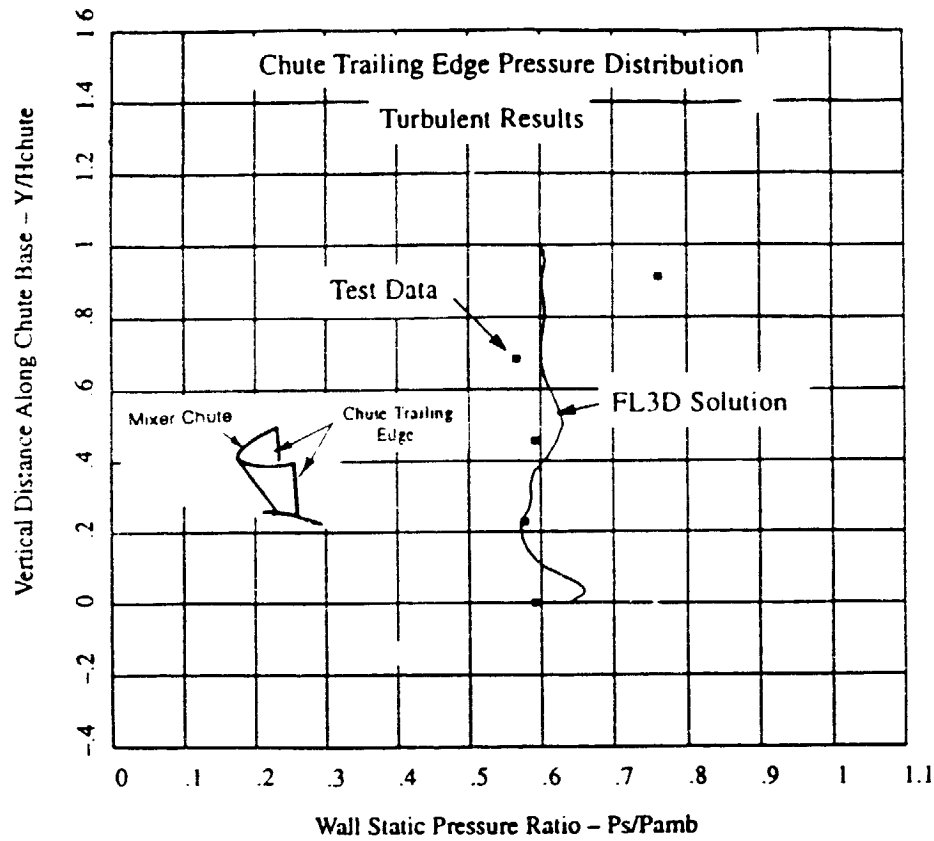- turbulent computations.

Figure 16. Pressure distribution comparison along the chute trailing edge
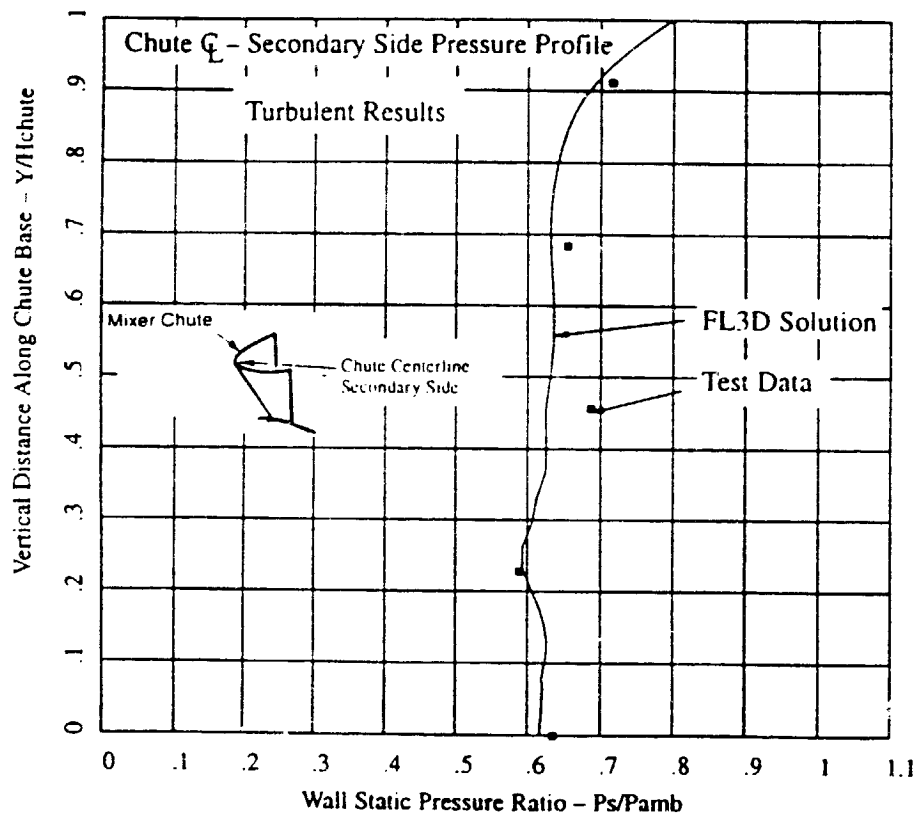- turbulent computations.

Figure 17. Pressure distribution comparison along the chute center-line
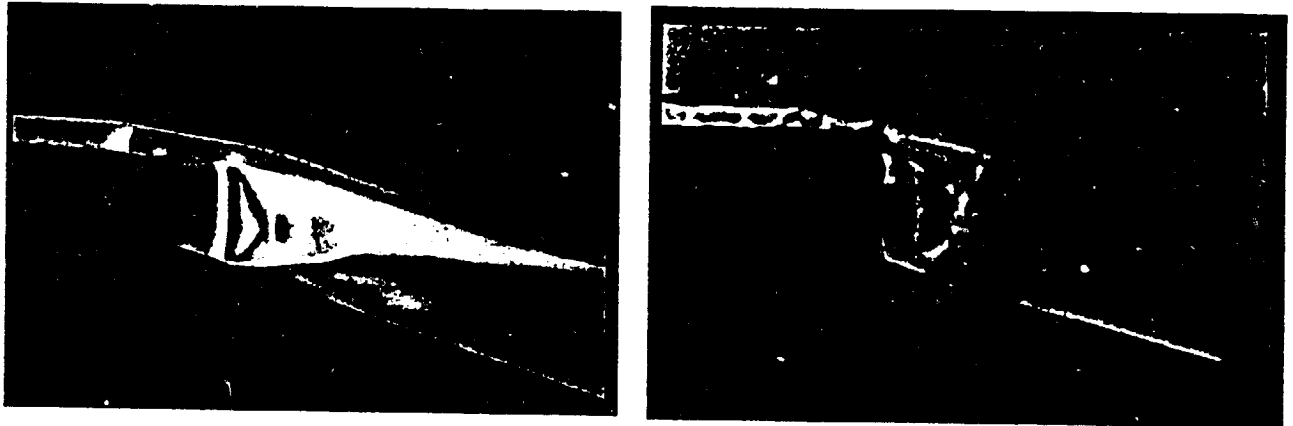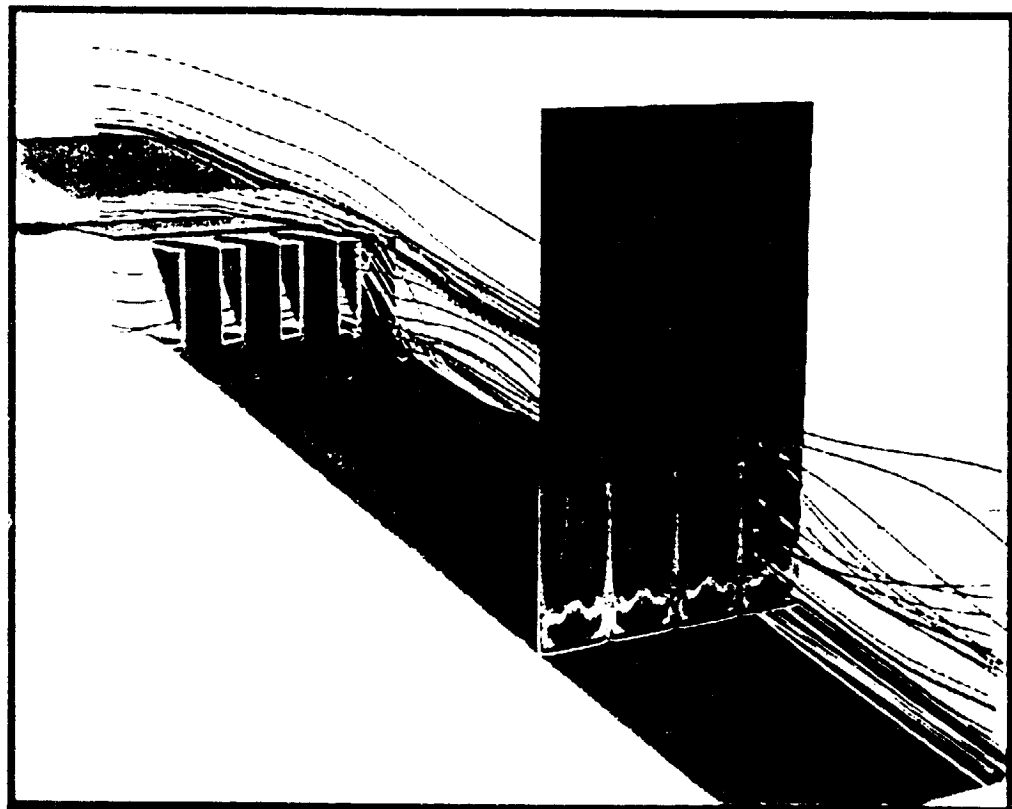- turbulent computations.

Figure 18. Comparison of the computed Mach contours on the core-symmetry plane (left) and the experimental shadowgraph (right).

F. Venkatapathy

Figure 19. A composite view from the computations : surface pressure, particle traces and Mach contours on axial plane downstream of the chute exit.

Time-Dependent Simulation of Reflected-Shock/Boundary Layer Interaction in Shock Tubes

G.J. Wilson[1], S.P. Sharma[2], and W.D. Gillespie[3]

[1] Eloret Institute, 3788 Fabian Way., Palo Alto, CA 94303, USA

[2] Aerothermodynamics Branch, NASA-Ames Research Center, Moffett Field, CA 94035, USA

[3] Department of Aeronautics and Astronautics, Stanford University, Stanford, CA 94305, USA

Abstract. An initial experimental/numerical investigation has been conducted to gain a better understanding of the multi-dimensional flow phenomena inside pulse facilities and the influence of these phenomena on test conditions and test times. Experimental data from the NASA Ames electric-arc driven shock tube facility (from cold driver shots) is compared to time-dependent axisymmetric numerical simulations of the complete facility. These comparisons help establish the numerical modelling requirements for simulating shock tube flow and help validate the computations. The numerical simulations are used to study the interaction between the reflected shock wave and the side wall boundary layer and the resulting shock bifurcation. Of particular interest is the effect of the bifurcated shock structure on the driver/driven gas interface. The computations demonstrate how this shock structure introduces a mechanism for the driver gas to contaminate the the stagnation region thereby reducing the duration of the test time. The simulations incorporate finite-rate chemistry, a moving mesh and laminar viscosity.

Key words: Shock Tube, Computation, Shock/Boundary Layer Interaction

1. Introduction

Knowing the length of the test time and the state of the test gas provided by shock tubes or shock tunnels is critical to interpreting data obtained from these facilities. Unfortunately, it is well established that the test time achieved in these facilities is usually significantly less than ideal theory predicts. Many investigations have been carried out to understand and quantify the physical mechanisms which cause shortened test times. These mechanisms include deformation of the contact discontinuity caused by the diaphragm rupture process, mass transfer of the driven gas into the boundary layer, contact discontinuity instabilities, and shock/boundary layer interaction after reflection of the incident shock off the end wall.

It is not clear which of the mechanisms mentioned above limits test times most and it may be that the dominant mechanism varies with the experimental facility or the run conditions. There is a large amount of evidence, however, that suggests that the reflected-shock/boundary layer interaction is often a major contributor to the contamination process. It is well established that under many conditions the reflected shock will interact with the boundary layer causing it to bifurcate near the wall (see Fig. 1). Mark (1958) developed a model to predict the characteristics of the bifurcation and the conditions under which it will occur. He showed that the flow in the energy deficient boundary layer has a stagnation pressure that is less than the stagnation pressure behind the normal reflected shock and is prevented from passing under the reflected shock. Instead, it separates and collects in a bubble of gas next to the wall. A consequence of the shock bifurcation is a jet of gas near the shock tube wall as depicted in Fig. 1. The jet is present because the gas which passes through the oblique shocks at the foot of the bifurcated shock retains a higher velocity than the gas which encounters the normal shock. Particularly clear experimental evidence of this phenomenon can be seen in the recent color schlieren photographs of Kleine et al. (1991) which include features such as the rolling up of the wall jet as it encounters the end wall. Davies (1966, 1967, 1969) used Mark's model to show that the wall jet provides a

mechanism for contamination of the stagnation region by propelling cold driver gas toward the end wall and into the driven gas. He and others such as Bull and Edwards (1968) have done experiments which measured the time of arrival of the cold driver gas through this mechanism.
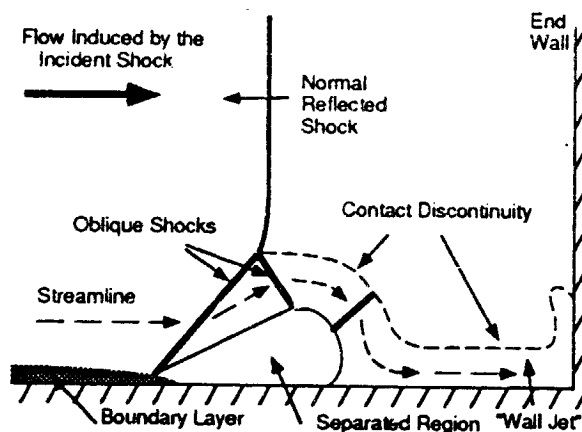

Fig. 1. Schematic diagram of reflected shock/boundary layer interaction
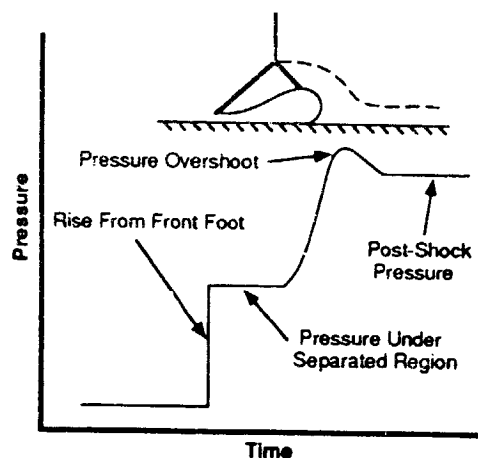

Fig. 2. Schematic diagram of pressure trace under bifurcated shock

The reflected-shock/boundary layer interaction described above can explain much of what is observed experimentally in shock tubes. However, more complicated flow structures such as a pseudo-shock (or shock train) can develop when the shock/boundary layer interaction is strong. Matsuo et al (1975), Strehlow and Cohen (1959), and Brossard and Charpentier (1985) all show schlieren photographs of the formation of multiple shocks after the reflection of the incident shock. The effect of these multiple shocks on driver gas contamination has not been studied.

In the absence of optical data, the presence of shock bifurcation can be inferred from side-wall pressure measurements. Figure 2 shows that the passage of the reflected shock is marked by a two-step pressure rise follow by a pressure overshoot as described by Sanderson (1969). It can also be deduced by noting the change of the reflected shock speed compared to inviscid theory (Mark 1958; Strehlow and Cohen 1959; Matsuo et al. 1975).

There have been several recent examples of computations of reflected-shock/boundary layer interaction at the end of a shock tube with the computational domain limited to the stagnation region (e.g. Kleine et al. 1991 and Yakano 1991). The present authors are unaware, however, of any computations which have looked at the contamination of the stagnation region with driver gas through the wall jet mechanism proposed by Davies. One way to accomplish this is to begin a simulation of a shock tube at the diaphragm rupture allowing the position of the contact discontinuity and the boundary layer development to be computed. This, in turn, makes it possible for phenomena such as the reflected shock/boundary layer interaction and the reflected-shock/contact discontinuity interaction to be investigated numerically. This approach is adopted herein by computing the time-dependent flow inside the NASA Ames electric-arc driven shock tube (cold driver shots without the arc-driver). The simulations assume that the contact discontinuity is planar at diaphragm rupture and that boundary layer is laminar. Experimental data in the form of wall static pressure traces and heat transfer was gathered to help guide the numerical modelling and validate the simulations. The present work is a continuation of research reported in Wilson et al. (1993) and more details can be found there.

2. Experimental Facility

The NASA Ames electric-arc driven shock tube facility has several possible configurations and has a large hypervelocity operating range using its arc-driver (Sharma and Park 1990). However, this work only considers experiments using a cold helium driver with nitrogen in the driven section. These shots were made with a cylindrical driver of .86 m (2.8 ft) in length and 10 cm (3.93 inches) in diameter. The driven section was 4.22 m (13.85 ft) long with the same diameter as the driver. A single self-break diaphragm separated the driver and driven gases.

For the current experiments the instrumentation consisted of pressure transducers flush mounted at three fixed positions on the shock tube walls, at 2, 6, and 24 inch s from the end wall. There were also two pressure transducers flush mounted on the end wall, one at the center and one 1/4 inch from the tube side wall. In addition, the end wall was modified so that it could be moved forward and backward at one inch increments. This made it possible to collect data at variable distances from the end wall (i.e. 1, 2, and 3 inches from the end wall for the first side wall gauge and, thus, 5, 6, and 7 inches from the end wall for the second gauge). The pressure transducers were PCB Piezotronics, Inc. Model 113A21 with a circular surface area .218 inches in diameter and a rise time of 1 microsecond. Heat-transfer data has also been collected at the same side wall locations at instrument locations opposite of the pressure transducers.

3. Numerical Method and Gas Model

The gas dynamic equations for the axisymmetric simulations are solved by using an explicit finite-volume form of the Harten-Yee upwind TVD scheme (Yee 1989). The gas model includes the three major species present in the shock tube for the present experiments (N_2, N, and He) and accounts for finite-rate chemical processes. A separate equation for vibrational energy is included so that vibrational nonequilibrium effects can be assessed. The present work, however, enforces thermal equilibrium. The numerical method is essentially an extension of the quasi-one-dimensional work in Wilson (1992). The full Navier-Stokes viscous terms are included.

Mesh points are clustered at the contact discontinuity to minimize numerical diffusion and are convected with the gas interface as it travels down the driven tube. This approach has the additional benefit of compressing all of the cells associated with the driven tube into the end wall region of the shock tube as the driven gas is compressed thereby providing a fine axial mesh during the shock reflection. The grid is also clustered around the incident shock so that the resolution is relatively high where the boundary layer is initially formed behind the shock. Points are also concentrated near the wall to resolve the boundary layer. Because the Euler terms are treated explicitly, the computations are advanced at a CFL number less than 1 based on the inviscid gas dynamics. To avoid the more limiting time step dictated by the viscous terms, the thin-layer viscous terms are treated implicitly (note that all the viscous terms are included explicitly). It is believed that the time accuracy of the solution is not significantly effected by this approach and without it the simulation becomes impractical. The source terms representing the finite-rate chemical kinetics and vibrational relaxation are also treated implicitly. This implicit formulation reduces the formal temporal accuracy to first order.

5. Results and Discussion

The results presented in this short paper represent a single test condition with a nominal driver pressure of 4.83 MPa (700 psi) and a driven pressure of 20 torr nitrogen with both sections at ambient temperature (295 K). Three shots are reported with the end wall position varied for each shot so that there is data 1, 2, and 3 inches from the end wall (these shall be referred to as the 1 inch position, the 2 inch position, etc.). Because of the self-break single diaphragm, a

precise repeatability of shock speed for the three shots was not possible. The shock speed for the 1, 2, and 3 inch positions were 1984 m/sec, 2005 m/sec. and 1953 m/sec, respectively. Figure 3 shows the pressure trace for the 2 inch position. Several of the major events are labeled. These include the passage of the incident and reflected shocks, the arrival of the rarefaction. and the presence of waves reflected off the contact discontinuity. The time axis is adjusted so that zero time corresponds to the shock arrival at the end wall. This allows a meaningful comparison of traces with the end wall in different positions.
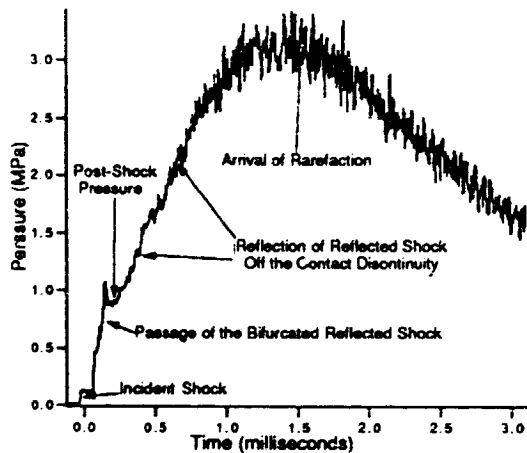

Fig. 3. Experimental and computed pressure traces 2 inches from the driven tube end wall
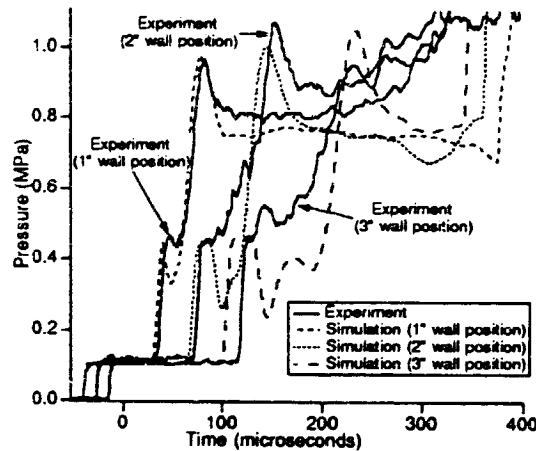
Fig. 4. Experimental and computed pressure traces 1, 2, and 3 inches from the driven tube end wall

The axisymmetric simulation used an initial driver pressure 11% higher than the experimentally reported value in order for the computed incident shock speed to match the experimental one. The reason for this discrepancy is not known. All other initial conditions matched the experimentally reported ones. A cold wall boundary condition of 295 K was enforced. The computational mesh contained 800 points along the length of the tube (400 each in the driver and driven sections) and 112 points between the tube centerline and an outer wall. The points were exponentially clustered near the wall with a minimum spacing of .150 mm at the wall for the first few meters of the driven tube and was ramped down to a constant .015 mm over the last .75 meters of the tube. This approach eased the computational cost by allowing a larger time step early in the solution. As mentioned before, the solutions assumed an initially planar contact discontinuity and laminar viscosity. Verification that the reflected shock/boundary layer interaction has all of the features depicted in Fig. 1 is presented by Wilson et al. (1993).

A composite of experimental and computed pressure traces in the end wall region for early times after the shock reflection is presented in Fig. 4. It is seen that the general features of the experimental and computed pressure traces are quite similar. Evidence of the shock/boundary layer interaction in the pressure traces, as depicted in Fig. 2, is clearly seen. The computation and experiment are in good agreement for the trace 1 inch from the end wall, fair agreement at 2 inch position, and by the 3 inch position it is clear that discrepancies are growing. Further deterioration of the agreement is seen in the traces farther back from the end wall (not shown here). While it appears that the growth of the bifurcated shock structure is being captured fairly well by the simulations, the computed speed of the bifurcated shock is too fast and the predicted pressures under the separated flow region differ. Even with the differences, the general features of the flow appear accurate enough that a qualitative investigation of the interaction of the reflected shock with the contact discontinuity is deemed worthwhile.
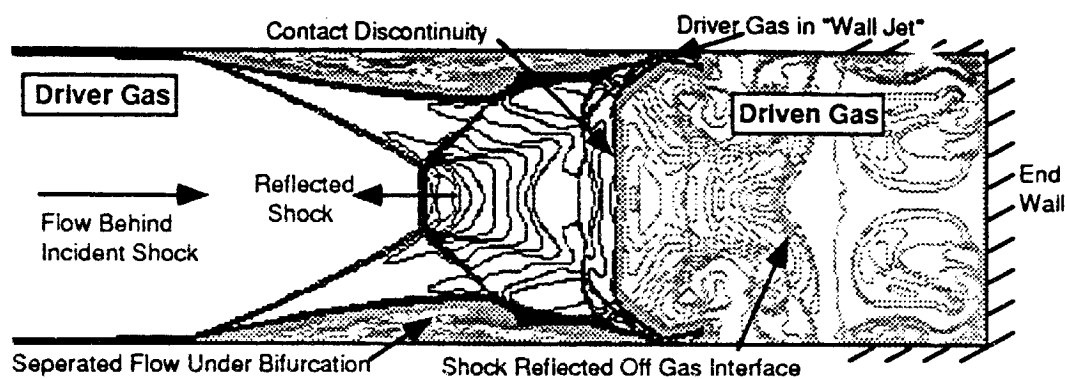
Fig. 5. Computed temperature contours showing reflected shock/contact discontinuity interaction

Figure 5 contains temperature contours after the reflected shock has interacted with the contact discontinuity. The figure shows that the bifurcated shock structure deforms the contact discontinuity near the wall. Hot driven gas in the separated region under the shock bifurcation is carried into the driver gas while the driver gas that passed through the oblique shocks of the bifurcation retains a higher flow velocity and penetrates into the driven gas (i.e. it is part of the wall jet). There is also the additional feature of a shock reflected off the contact discontinuity due to the overtailored conditions. There are many nonuniformities in the stagnation region because of the shock/boundary layer interaction. As waves such as the shock reflected off the contact discontinuity interact with these non-uniformities even more complex features are formed. It is easy to see why pressure trace data can become quite noisy.

There are many possible reasons for the discrepancies seen between the experimental data and the present computations. Experimentally, the point of transition between laminar and turbulent flow is not known. It is believed that the flow near the end wall is laminar (heat transfer data seems to support this); however, the flow must eventually become turbulent. This may happen in the separated flow region under the bifurcated shock. Data interpretation is further complicated by arbitrary variations in the finer features. For example, the size of the pressure overshoot associated with the shock bifurcation can be notably different on the same shot for two transducers mounted at opposite sides of the tube. Numerically, the authors have found that it very difficult to resolve the shock/boundary layer interaction to the point where solutions become grid independent. Many grid refinement studies have shown that the wall spacing used here (.015 mm) is nearly sufficient;, however, these studies have also shown that the grid spacing along the tube is also important and that the current solutions would be helped by further grid refinement. Additionally, the starting assumption of an sharply defined, planar contact discontinuity causes waves which interact with the interface to be much more sharp (and often of higher magnitude) than those observed experimentally. An initially deformed interface will be tried in the future.

5. Conclusions

Axisymmetric simulations of the NASA Ames electric-arc driven shock tube have been done which include the wall boundary layer and the computations have been compared with experimental data. These simulations have allowed the wall jet created by the reflected shock/boundary layer interaction to be investigated numerically for the first time. These simulations support earlier analytical and experimental work which indicate that this mechanism can contribute to the reduction of the usable test time by allowing the driver gas to contaminate the stagnation region. Before any driver gas contamination, the wall jet creates nonuniformities in the stagnation region

which create complex flow patterns, especially when waves due to non-tailored conditions interact with these non-uniformities.

Acknowledgement

References

Brossard J and Charpentier N (1985) Experimental Study of Shock Wave Reflection in a Narrow Channel. Proc 15th Intl Symp. on Shock Waves and Shock Tubes, pp. 163-169

Bull DC and Edwards DH (1968) An Investigation of the Reflected Shock Process in a Shock Tube. AIAA J 6:1549-1555

Davies L (1966) The Interaction of a Reflected Shock Wave with the Boundary Layer in a Shock Tube and its Influence on the Duration of Hot Flow in the Reflected-Shock Tunnel. Part I. Aeronautical Research Council-CP-880

Davies L (1967) The Interaction of a Reflected Shock Wave with the Boundary Layer in a Shock Tube and its Influence on the Duration of Hot Flow in the Reflected-Shock Tunnel. Part II. Aeronautical Research Council-CP-881

Davies L and Wilson JL (1969) Influence of Reflected Shock and Boundary-Layer Interaction on Shock-Tube Flow. Phys of Fluids, Supplement I, 12:I-37 - I-43

Kleine H, Lyakhov VN, Gvozdeva LG and Grönig H (1991) Bifurcation of a Reflected Shock Wave in a Shock Tube. Proc 18th Intl Symp on Shock Waves and Shock Tubes, pp. 261-266

Mark H (1958) The Interaction of a Reflected Shock Wave with the Boundary Layer in a Shock Tube. NACA TM 1418

Matsuo K, Kage K, and Kawagoe S (1975) The Interaction of a Reflected Shock Wave with the Contact Region in a Shock Tube. Bull of the JSME 18.

Sanderson RJ (1969) Interpretation of Pressure Measurements Behind the Reflected Shock in a Rectangular Shock Tube. AIAA J 7:1370-1372

Sharma, SP and Park C (1990) Operating Characteristics of a 60- and 10 cm Electric Arc-Driven Shock Tube - Parts 1&2: The Driver and Driven Sections. J Therm and Heat Trans 4:259-272

Strehlow RA and Cohen A (1959) Limitations of the Reflected Shock Technique for Studying Fast Chemical Reactions and Its Applications to the Observation of Relaxation in Nitrogen and Oxygen. J of Chem Phys 30:257-265

Wilson, GJ (1992) Time-Dependent Quasi-One Dimensional Simulations of High Enthalpy Pulse Facilities. AIAA paper-92-5096, AIAA 4th Intl Aerospace Planes Conf, Orlando, FL

Wilson, GJ (1993) Time-Dependent Simulations of Reflected-Shock/Boundary Layer Interaction. AIAA paper-93-0480, AIAA 31st Aerospace Sciences Meeting, Reno, NV.

Yakano, Y (1991) Simulations for Reflected Shock Waves in Combustible Gas in Shock Tubes. Proc 18th Intl Symp on Shock Waves and Shock Tubes, pp. 869-874

Yee, HC (1989) A Class of High-Resolution Explicit and Implicit Shock-Capturing Methods. NASA TM 101088

CHARACTERIZATION OF ARC-JET FLOWS USING LASER-INDUCED FLUORESCENCE

Douglas J. Bamford and Anthony O'Keefe

Deacon Research, Palo Alto, CA

Anthony W. Strawa and David A. Stewart

NASA Ames Research Center. Moffett Field, CA

and

Dikran S. Babikian

Eloret Institute, Palo Alto, CA

Extended Abstract

We have used laser induced fluorescence (LIF) to characterize the free stream of the 20 Megawatt Aerodynamic Heating Facility at NASA/Ames Research Center. Knowledge of the free stream properties is required for a detailed understanding of the interaction between the arc flow and test models. Until recently the properties of the free stream have been inferred from measurements of bulk properties such as heat loss to cooling water in the discharge and heat transfer to test models, combined with emission spectroscopy and computer modeling of the arc jet flow. Heat loss measurements in the discharge are too difficult to be carried out routinely, and model heat transfer measurements suffer from a lack of detailed knowledge of the chemical processes occurring on the surface. Because the most important species in the flow are in the ground electronic state, emission spectroscopy can provide no information about them. Our experimental program is designed to measure the velocities, translational temperatures, and radial distributions for two of the most important species, atomic oxygen and atomic nitrogen. Com-

parison of the experimental results with both theory and earlier experimental results will greatly increase our knowledge of the free stream properties.

The experimental approach for number density measurements is as follows. The photon source is a Nd:YAG-pumped, frequency doubled dye laser producing tunable radiation in ultraviolet. To detect atomic oxygen, we excite the $3p^3P \leftarrow 2p^3P$ two-photon transition at 226 nm and detect fluorescence from the $3p^3P_{2,1,0} \rightarrow 3s^3S_1$ transition at 845 nm. For atomic nitrogen detection, we plan to excite the $3p^4D \leftarrow 2p^4S$ two-photon transition at 211 nm and detect fluorescence from the $3p^4D \rightarrow 3s^4P$ transition at 870 nm. The fluorescence is imaged onto the surface of a red-sensitive photomultiplier tube. For number density measurements the intensity of the near-infrared laser-induced fluorescence (LIF) is monitored as a function of the wavelength of the ultraviolet laser. Using calibration procedures described previously [Phys. Rev. A 34, 185 (1986)] along with absolute values of the two-photon cross section [Phys. Rev. A 36, 3497 (1987)] the absolute number density is determined. This measurement is repeated at several different radial positions (with a spatial resolution of about 1 cm) to determine the radial dependence of the number density in the flow (which has cylindrical symmetry).

Flow velocities for atomic oxygen are determined from the Doppler shift of the $3p^3P_{2,1,0} \leftarrow 2p^3P_2$ transition relative to the fixed frequency of a nitric oxide LIF transition in a static room temperature gas cell. We first record the unshifted position by taking several simultaneous spectra of flowing O-atoms and static nitric oxide with the laser at 90 degrees to the flow, as shown in Figure 1. We then repeat the experiment with the laser at an angle θ degrees to the flow, as shown in Figure 2. The spacing between the $R_1(16)$ line of the $\gamma(0,0)$ band of $^{15}N^{16}O$ and the $3p^3P_{2,1,0} \leftarrow 2p^3P_2$ line of atomic oxygen is measured in both cases, and the difference between these spacings, $\Delta\lambda$, is determined. The velocity, v, is then calculated using the following equation:

$$v = (\Delta\lambda/\lambda) \times (c/\cos\theta),$$

where c is the speed of light. The precision of the O-atom velocity measurements is ± 1 km/sec. For atomic copper we use a similar approach, eliminating the need for a frequency standard by simultaneously exciting the flow with beams at $\theta = 90$ degrees and $\theta = 73$ degrees. Excitation occurs via the $^2P_{3/2} \leftarrow ^2S_{1/2}$ transition at 324.85 nm or the $^2P_{1/2} \leftarrow ^2S_{1/2}$ transition at 327.49

nm, and fluorescence is detected from either the $^2P_{3/2}\rightarrow{}^2D_{5/2}$ transition at 510.70 nm or the $^2P_{1/2}\rightarrow{}^2D_{3/2}$ transition at 578.37 nm. The precision of the Cu-atom velocity measurements is ±1.5 km/sec.

The relative O-atom number density as a function of radial position, for expansion through a 61 cm diameter nozzle, is shown in Table I.

Table I. Relative number density of $O(2p^3)$ as a function of radial position.

==

distance from centerline (cm)	relative [O] (arbitrary units)
0	0.86
15	0.85
25	0.63

==

In future work we will measure the relative number density at several additional radial positions and place the number densities on an absolute scale.

The experimental velocities are given in Table II.

Table II. Summary of experimental velocity measurements.

==

Date	species	nozzle dia. (cm)	mass-avg. enthalpy (MJ/kg)	velocity (km/sec)
9/16/92	Cu	30.5	15	3.0
9/17/92	Cu	30.5	15	2.6
9/21/92	Cu	30.5	13	3.2
9/21/92	Cu	30.5	13	3.9
12/17/92	O	30.5	17	2.7
2/19/93	O	61.0	15	4.2
2/19/93	O	61.0	15	4.0
3/9/93	O	61.0	15	4.2
3/10/93	O	61.0	12	5.3
3/31/93	O	61.0	10	4.1
3/31/93	O	61.0	9	4.4

==

All of these velocities except the last one were measured along the centerline of the flow. The last velocity was measured at a point 15 cm above the centerline of the flow to test for a spatial

dependence of the flow velocity. Within our error limits, there appears to be no spatial dependence. Because the velocities measured under (nominally) identical conditions are internally consistent, they can be used with confidence to test existing codes describing the arc jet flow. In the near future we will add another column to Table II containing the calculated velocities and briefly describe the procedure used to obtain them.

To measure absolute number densities of $O(2p^3P)$ we must measure the rate of collisional quenching (by electrons and neutral species) which removes population from the $3p^3P$ state following laser excitation. Because the laser pulse is less than 5 ns long, we can measure this rate directly if the fluorescence lifetime is substantially longer than 5 ns. As Figure 3 shows, the fluorescence lifetime under typical arc jet conditions is about 28 ns. The ratio of this lifetime to the radiative lifetime ($\tau = 35$ ns) is the fluorescence quantu: . yield, about 80%.

In summary, we have used laser induced fluorescence (LIF) to characterize the free stream of the 20 Megawatt Aerodynamic Heating Facility at NASA/Ames Research Center. The velocities of both a major flow component (atomic oxygen) and a minor component (atomic copper) have been measured under a variety of operating conditions. The relative number density of O-atoms in the $2p^3P$ electronic state as a function of radial position has been determined under one set of conditions. The rate of collisional quenching for $O(3p^3P)$ has been measured. In the near future we plan several extensions of this work, including absolute number density measurements for $O(2p^3P)$, relative number density measurements for $N(2p^4S)$, rotational-translational temperature measurements using $O(2p^3P)$, and measurements of flow velocity as a function of radial position. A detailed comparison of the LIF results with both computer simulations of the arc jet flow and previous experimental measurements will be carried out.

Figure 1. LIF signals for nitric oxide (in a room temperature gas cell) and atomic oxygen (in the arc jet) as a function of laser wavelength, with the laser at 90 degrees to the flow direction. (The ultraviolet excitation wavelength is half the wavelength shown, which is the dye laser wavelength prior to frequency-doubling.)
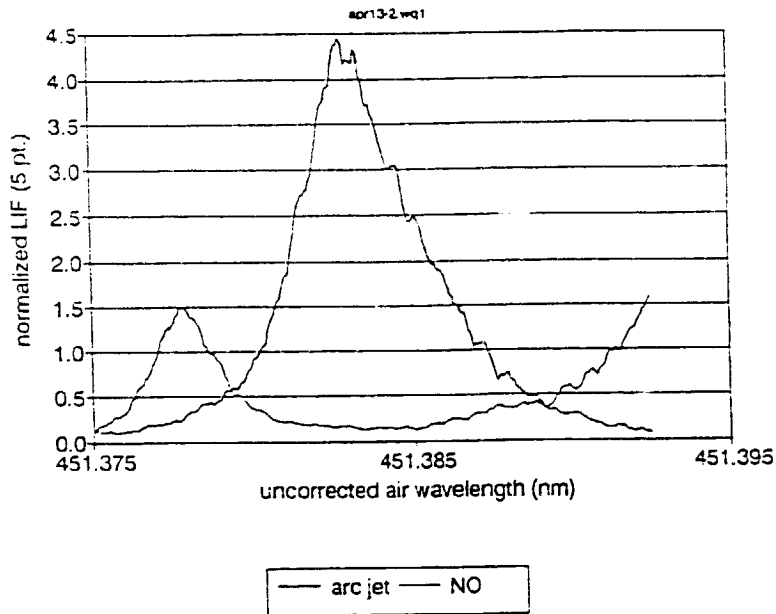

Figure 2. The same as Figure 1, but with the laser at 73 degrees to the flow direction. The O-atom resonance has moved further away from the NO resonance by an amount equal to the Doppler shift.
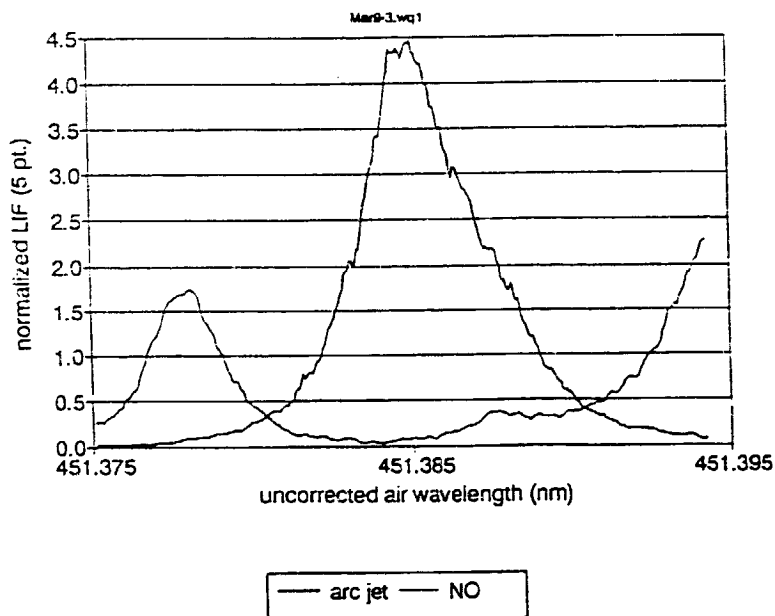
Figure 3. Fluorescence intensity as a function of time following excitation of the $3p^3P_{2,1,0} \leftarrow 2p^3P_2$ transition in atomic oxygen with a short laser pulse.
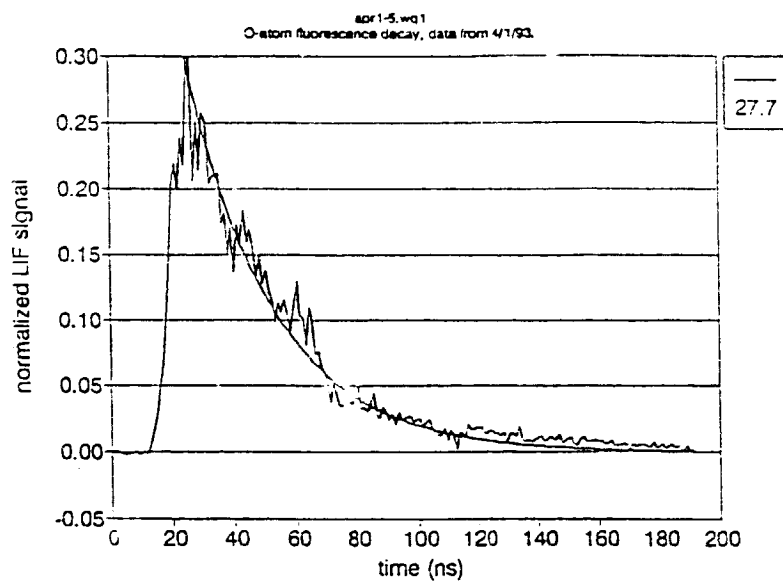
Measured and Calculated Spectral Radiation from a Blunt Body Shock Layer in an Arc-Jet Wind Tunnel

Dikran S. Babikian[1]
Roger A. Craig[2]
Giuseppe Palumbo[3]
and
Grant Palmer[4]

The shock layer spectral radiation incident on a blunt body placed in a NASA-Ames $20MW$ arc-jet wind tunnel is measured. The spectra show the atomic lines of oxygen, nitrogen, and copper, as well as the molecular band systems of NO, N_2, N_2^+, and CN.

The flow fields of the experiment is predicted in three separate steps. First, the equilibrium flow field of the arc column and the nozzle entrance are computed from the known operating conditions of the arc-jet wind tunnel using the arc heater flow field code ARCFLO. Second, the nonequilibrium flow field of the nozzle and the free stream are calculated using the multi-temperature, one dimensional code NOZNT. Third, the nonequilibrium flow field of the blunt body shock layer is calculated using the axisymmetric 2d2T code, which solves the two dimensional Navier Stokes equations for a two temperature reacting gas. Thirteen species; N, O, NO, Ar, N_2, O_2, NO^+, N_2^+, O_2^+, O^+, N^+, Ar^+, and e^- are included in the chemistry model.

The spectra of the incident radiation in the range $200nm$ to $1000nm$ are calculated using the modified version of the nonequilibrium air radiation computer code NEQAIR. The computed and the measured spectra are compared.

Results of analysis of the vacuum ultra violet region from $120nm$ to $200nm$ will be reported elsewhere.

Experiment

The NASA Ames $20MW$ Aerodynamic Heating Facility is operated with a conical nozzle. The experimental set-up, test conditions, and digital data acquisition are described in detail in references [1] and [2]. Figure 1 shows a schematic sketch of the nozzle and the spectrographic set-up. Figure 2 is a schematic sketch of the 6.0 inch flat disk model and the helium cooled magnesium floride MgF_2 window that transmits the surface radiative flux into an evacuated optical system. The incident radiation is collimated via a set of mirrors and focused onto the entrance slit of a McPherson spectrometer. The spectrometer has a

[1] Eloret Institute, 3788 Fabian Way Palo Alto, CA 94303. Research Scientist, Member AIAA.
Mailing Address: NASA Ames Research Center, MS 230-2, Moffett Field, CA 94035.
[2] MCAT Institute, NASA Ames Research Center, Moffett Field, CA. Research Scientist, Sn. Mem. AIAA.
[3] Eloret Institute, 3788 Fabian Way Palo Alto, CA 94303. Research Scientist.
[4] NASA Ames Research Center. Moffett Field, CA. Research Scientist, Member AIAA.

focal length of 0.5 meter and operates either as a scanning monochromator or as film spectrograph. The radiation from the $120nm$ to $1000nm$ range incident on the MgF_2 window is measured. The data are obtained using films or photomultiplier tubes.

Figures 3 and 4 show samples of the experimental data obtained with the photo multiplier tube and the film. The photomultiplier record of spectrum from $200nm$ to $300nm$ is shown in Fig. 3. This region is dominated by the $NO\gamma$ band system resulting from the $A^2\Sigma^+ \rightarrow X^2\Pi$ transition. Figure 4 is the densitometer trace of a film record from $500nm$ to $900nm$. Atomic oxygen and nitrogen emission lines are well resolved. Copper lines are seen at $324.7nm$ and $327.4nm$ in the second and third orders.

Computation

The equilibrium flow field of the arc column and the nozzle entrance are calculated using the ARCFLO (Arc Heater Flowfield) computer program [3,4,5]. The inputs to the ARCFLO are the operating parameters of the $20MW$ Aerothermodynamic Heating facilities given in Ref. 2. The enthalpy at the entrance of the nozzle, an important parameter for solving the nozzle flow, is determined from the enthalpy distribution at the exit of the constrictor tube [6]. The nonequilibrium flow field of the nozzle and the upstream shock layer flow conditions are calculated using the multi-temperature nonequilibrium nozzle flow code NOZNT [7]. Figures 5 and 6 show temperature and mole fraction variation along the axis of the nozzle.

The two-dimensional code, 2d2T, is used to calculate the thermochemical nonequilibrium flowfield of the blunt body [8,9]. The full Navier-Stokes equations and 13-species chemical model with the latest reaction rates are incorporated. The electron excitation energy and the vibrational energy are assumed to be characterize by one temperature, T_v, as are the translational and rotational energies by one temperature, T_t. Figures 7 and 8 show the stagnation line temperature and mole fraction profiles respectively.

The spectrum of the radiative power that strikes the stagnation point of the flat disk model is calculated using the modified version of the NEQAIR code developed by Park [10,11]. The spectra shown in Figs. 9 and 10 are preliminary results and are obtained by spatially integrating the local radiative properties along the stagnation streamline. Figure 9 is the calculated spectrum from $200nm$ to $300nm$ corresponding to measurements shown in Fig. 3. Figure 10 shows the calculated spectrum from $500nm$ to $900nm$ that corresponding to measurements shown in Fig. 4.

This work is an initial effort to eventually obtain a computationally based, experimentally validated, description of the physical and chemical processes in an arc-jet wind tunnel. In the final paper, comparison of the calculations and the experimental data will be presented.

References

[1] Palumbo, G., "Shock Layer Vacuum UV Spectroscopy in an Arc-Jet Wind Tunnel," NASA Technical Memorandum 102258.
[2] Palumbo, G., Craig, R., and Carrasco, A., "Spectral Measurements of Shock Layer Radiation in an Arc-Jet Wind Tunnel," Proceedings of 39th ISA International Meeting, Albuquerque, New Mexico, May 1993.
[3] Watson, V.R. and Pegot, E.B., "Numerical Calculations for the Characteristics of Gas

Flowing Axially Through a Constricted Arc," NASA TN D-4042, 1967.

[4] Nicolet, W.E., Shepard, C.E., Clark, K.C., Balakrishnan, A., Kesselring, J.P., Suchsland, K.E., and Reese, J.J., "Methods for the Analysis of High-Pressure, high Enthalpy Arc Heaters," AIAA paper 75-704, Denver, Colorado, 1975.

[5] Nicolet, W.E., Shepard, C.E., Clark, K.C., Balakrishnan, A., Kesselring, J.P., Suchsland, K.E., and Reese, J.J., "Analytical and Design Study for a High-Pressure, High-Enthalpy Constricted Arc Heater," AEDC-TR-75-47, 1975.

[6] Gopaul, K.J.M.N., Babikian, S.D., and Park, C., "Measurement and Analysis of NO Radiation in an Arc-Jet Flow," AIAA Paper 93-2800, Orlando, Florida, July 1993.

[7] Park, C. and Lee, S.H., "Validation of Multi-Temperature Nozzle Flow Code NOZNT," AIAA Paper 93-2862, Orlando, Florida, July 1993.

[8] Palmer, G., "Enhanced Thermochemical Nonequilibrium Computations of Flow Around the Aeroassist Flight Experiment Vehicle," AIAA Paper 90-1772, 1990.

[9] Palmer, G., "Thermochemical Nonequilibrium Flow Computations of Flow Around the Aeroassist Flight Experiment," Journal of Thermophysics and Heat Transfer, Vol. 6, No. 3, 1992, pp. 405-411.

[10] Park, C., "Nonequilibrium Air Radiation (NEQAIR) Program: User's Manual," NASA Technical Memorandum 86707, 1985.

[11] Park, C., "Calculations of Nonequilibrium Radiation in the Fight Regimes of Aeroassisted Orbital Transfer Vehicles," Thermal Design of Aeroassisted Orbital Transfer Vehicles, Progress in Astronautics and Aeronautics, Vol. 96, edited by H. F. Nelson, AIAA, New York, 1985, pp. 395-418.
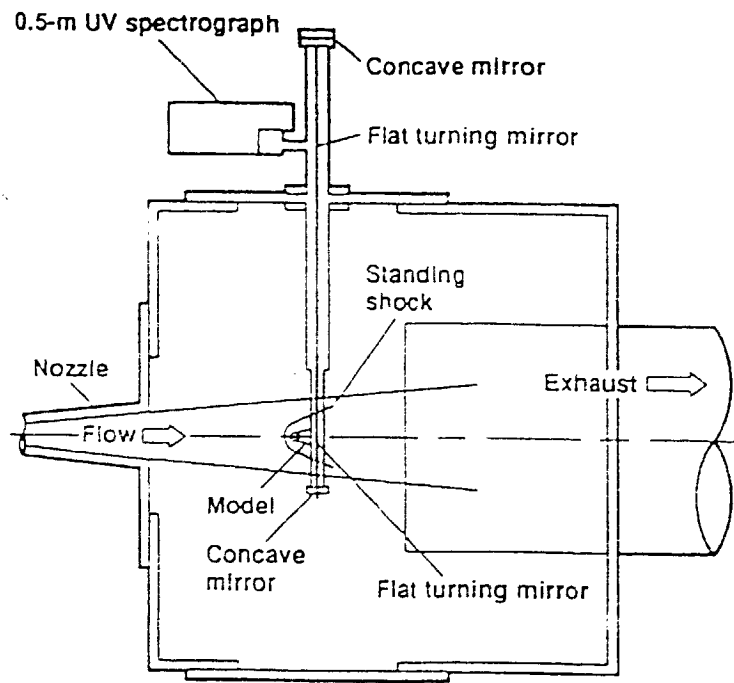
Figure 1. Sketch of model showing location in arc-jet wind tunnel flow. The stagnation region flux incident on the model aperture is imaged onto the spectrometer through an evacuated optical system.
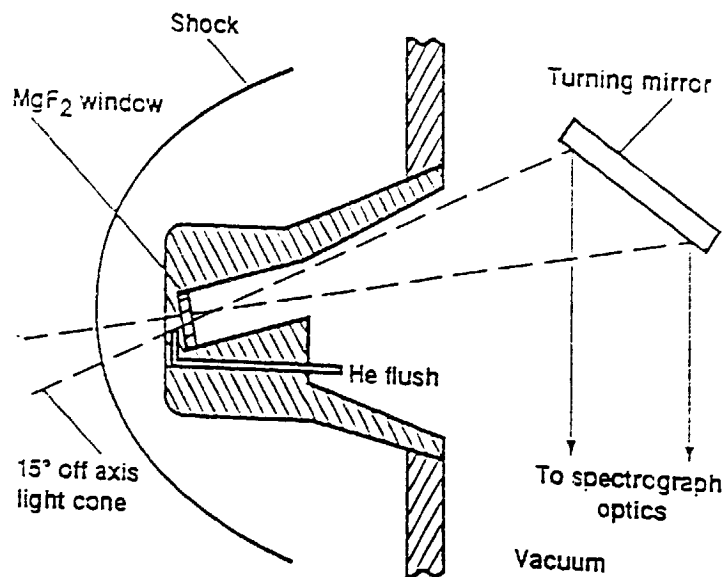

Figure 2. Sketch of the model face showing the helium cooled window. The view field is canted 15" from the tunnel centerline to exclude radiation from the arc column.
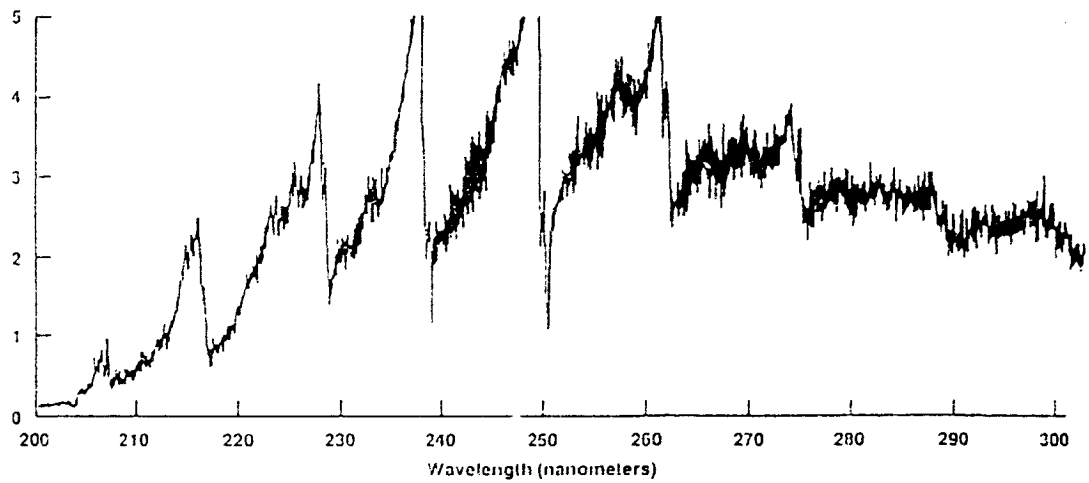
Figure 3.   Stagnation region surface flux from 200 nm to 300 nm:
Photomultiplier output with spectrometer used in scanning
monochromator mode.
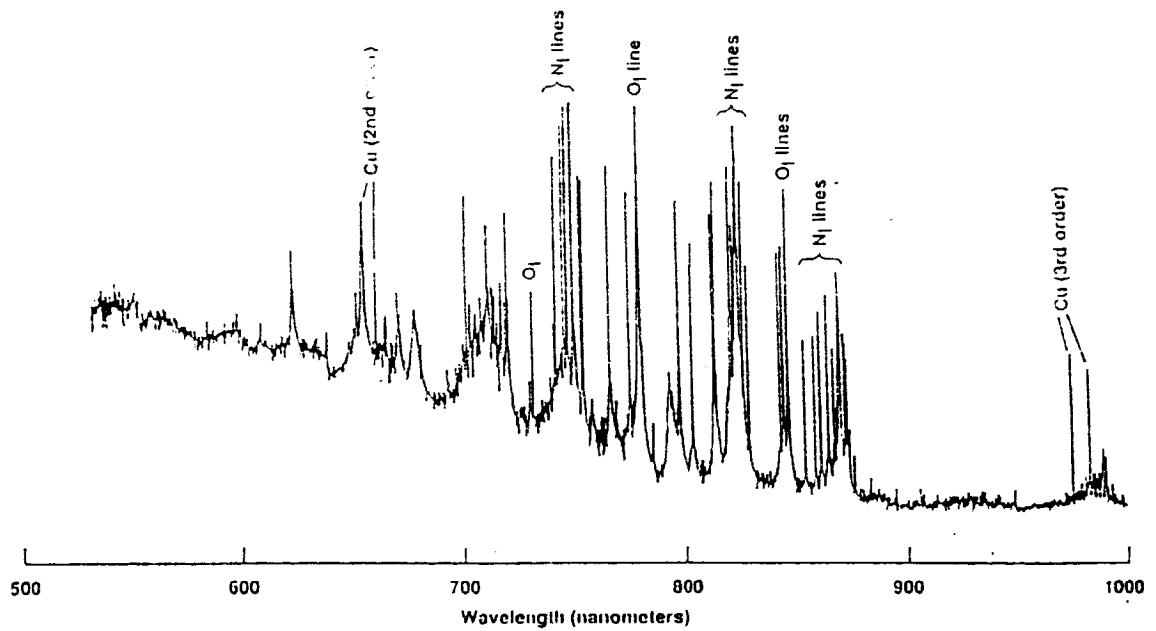
Figure 4.   Stagnation region surface flux from 500 nm to 900 nm:
Densitometer trace of photographic record with spectrometer used in
film spectrograph mode.
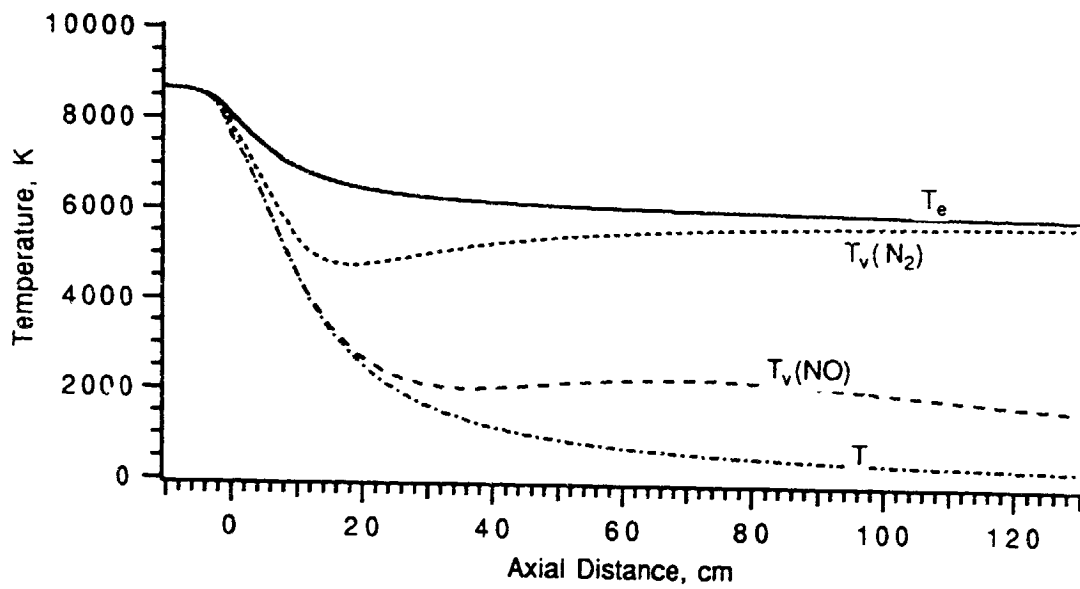
Figure 5.   Calculated temperature profiles along the nozzle.
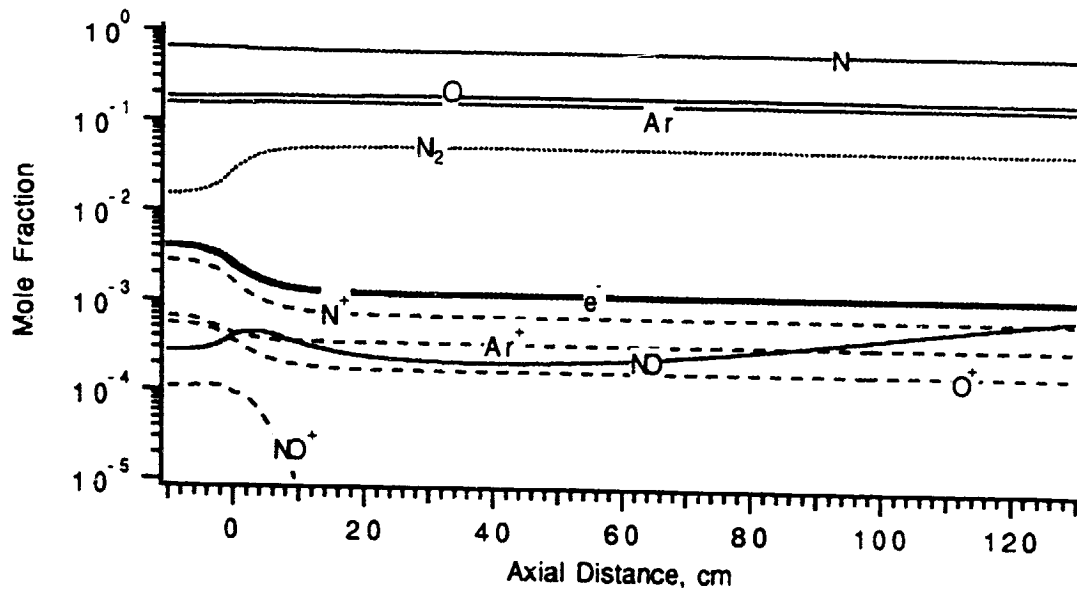
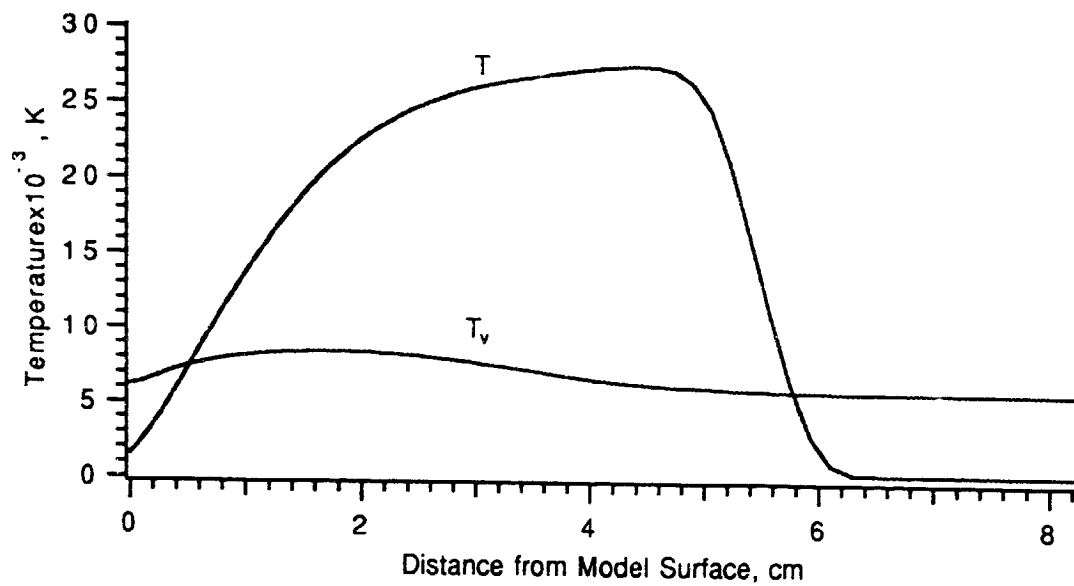Figure 6.   Calculated mole fractions along the nozzle.
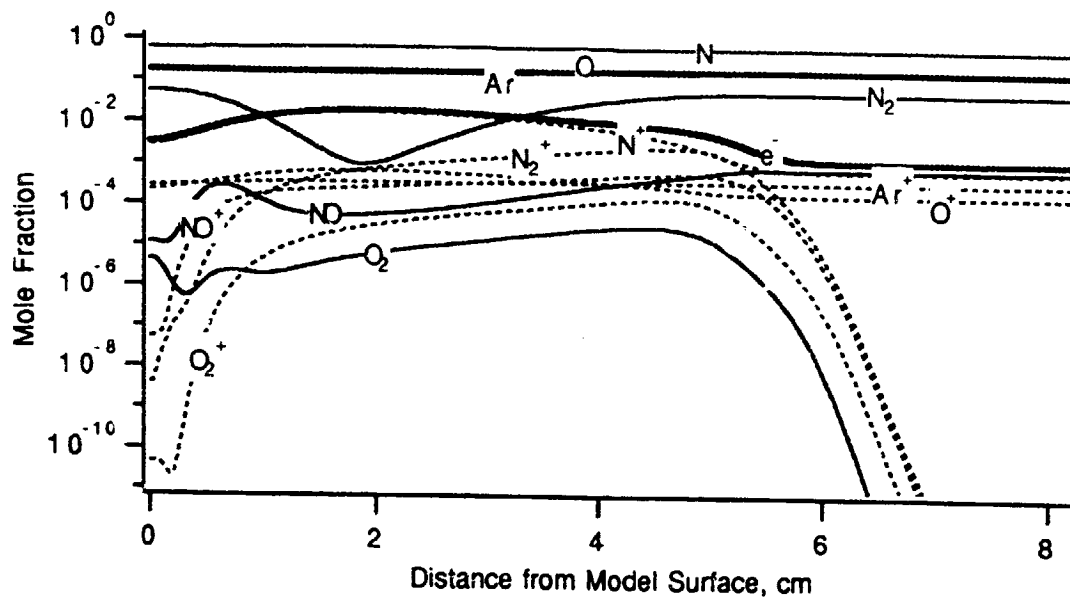
Figure 7.   Calculated temperature profiles along the stagnation streamline.

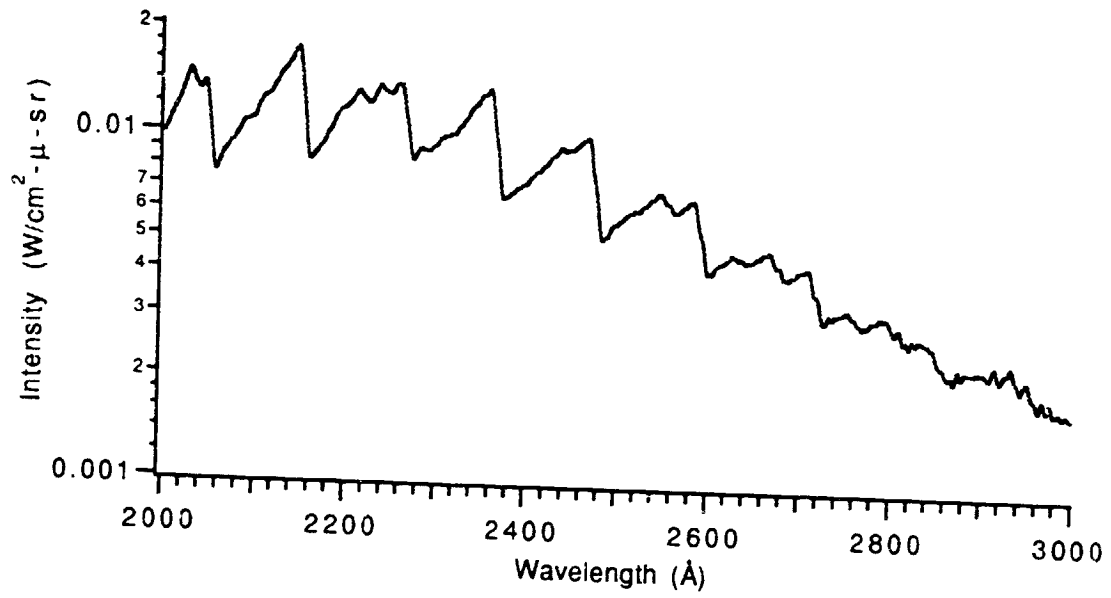Figure 8.   Calculated mole fractions along the stagnation streamline.

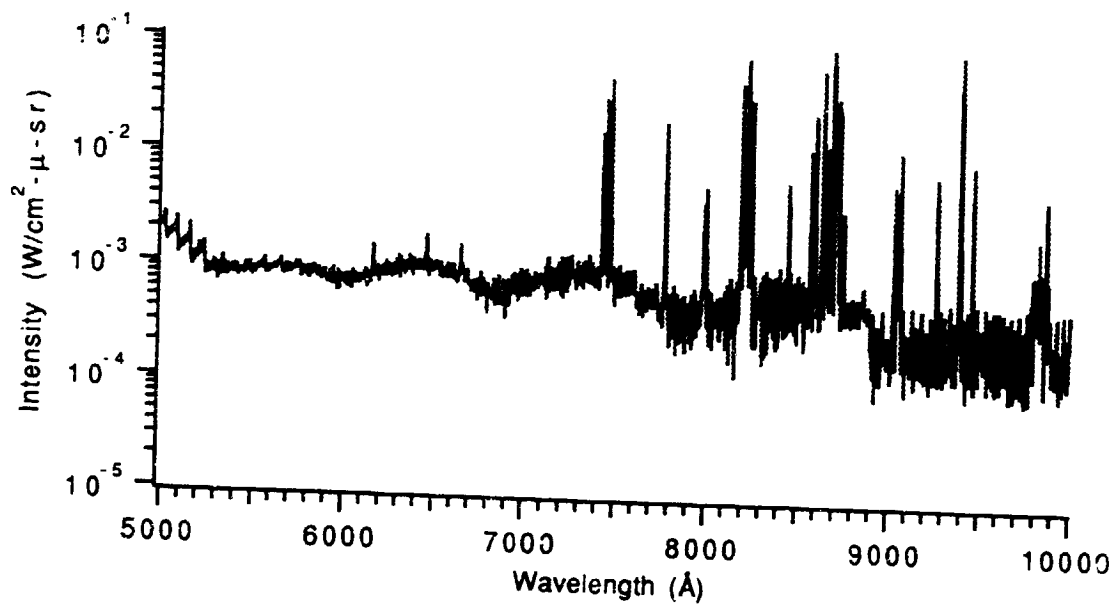Figure 9.   Preliminary calculated spectrum from 200nm to 300nm.

Figure 10.   Preliminary calculated spectrum from 5000nm to 10000nm.

Spectroscopic Investigation of Thermochemical Processes in a Blunt Body Shock Layer in an Arc-Jet

Dikran S. Babikian[1] and George A. Raiche[2]

Abstract

The spectral radiation from the shock layer over a 150 mm diameter flat disk model in the test section of an arc-jet wind tunnel is measured and computed. Three prominent molecular band systems, the 440-470 nm spectral range of the N_2^+ First Negative ($B^2\Sigma^+_u \rightarrow X^2\Sigma^+_g$), the 700-780 nm apectral range of the N_2 First Positive ($B^3\Pi_g \rightarrow A^3\Sigma^+_u$), and the 250-260 nm spectral range of the $NO\gamma$ ($A^2\Sigma^+ \rightarrow X^2\Pi$) are identified and analyzed. In the case of N_2^+, transitions from $v' \leq 3$ are observed; for $NO\gamma$ band system, vibrational tranitions from $v' \leq 2$ are observed. These spectra are used to extract rotational, vibrational, and electronic temperatures.

The experimental flow field is numerically simulated in three seperate steps. First the equilibrium flow field of the arc column and the nozzle entrance are computed from the known operating conditions of the arc-jet, second the nonequilibrium flow field of the nozzle and the free stream are computed, and third the nonequilibrium flow field of the flat disk shock layer is calculated. The spectra are clculated using the computed flow field properties and the nonequilibrium radiation computer code NEQAIR. The computed and the measured spectra are compared.

Experiment

The NASA Ames 20 MW Aerodynamic Heating Facility is operated with a conical nozzle. Two arc conditions are tested, 600 amps and 0.68 atm column pressure, and 1200 amps and 1.7 atm. The spectral data are resolved spatially along the stagnation stream line yielding the spatial distributions of the emitting species. A McPherson spectrometer with a photomultiplier tube is used to obtain the data. Our optical setup with f/50 and collection geometry with a demagnification factor of 6 limits the field of view to a cylinder with main axis parallel to the model face, crossing the center of the face and the jet axis. The measurement averages the radiation intensity over a cylindrical volume of 5 mm diameter. The optical system forms a real image of the shock layer at the entrance slit of the monochrometer. The spatial profiles are obtained by moving this image over the slit. Figure 1 shows the $NO\gamma$ in the 250-260 nm range at 12 mm from the model surface and at the high pressure test condition. Vibrational tranitions from $v' \leq 2$ are observed in contrast with previous

---

[1]Research Scientist. Eloret Institute, Palo Alto, California. Member AIAA.

[2]Assistant Professor. Department of Chemistry, Hamilton College, Clinton NY.

observations[1] in the freestream. Figure 2 shows the N_2^+ First Negative in the 440-470 nm range, and Fig. 3 shows the N_2 First Positive in the 700-780 nm range. These spectra are also at the same spatial location and test condition. The resulting spectral resolution is 0.2 nm. These spectra should be adequate for extracting rotational, vibrational, and electronic state distribution from the approperiate species and comparing with the computations.

Computation

The equilibrium flow field of the arc column and the nozzle entrance are calculated using the ARCFLO (Arc Heater Flowfield) computer program.[2,3,4] The inputs to the ARCFLO are the operating parameters of the $20MW$ Aerothermodynamic Heating facilities. The enthalpy at the entrance of the nozzle, an important parameter for solving the nozzle flow, is determined from the enthalpy distribution at the exit of the constrictor tube[1]. The nonequilibrium flow field of the nozzle and the upstream shock layer flow conditions are calculated using the multi-temperature nonequilibrium nozzle flow code NOZNT.[5]

The two-dimensional code, 2d2T, is used to calculate the thermochemical nonequilibrium flowfield of the model[6,7]. The full Navier-Stokes equations and 13-species chemical model with the latest reaction rates are incorporated in this code. The electron excitation energy and the vibrational energy are assumed to be characterized by one temperature, T_v. Similarly, translational and rotational energies are characterized by one temperature, T_t. Figures 4 and 5 show a typical such solution for the stagnation line temperature and mole fraction profiles respectively.

The spectrum of the emitted radiative power at a given spatial location away from the surface of the model is calculated using the modified version of the NEQAIR code developed by Park[8,9] using the computed properties.

This work is an initial effort to eventually obtain a computationally based, experimentally validated, description of the physical and chemical processes in an arc-jet wind tunnel. In the final paper, comparison of the calculations and the experimental data will be presented.

References

[1] Babikian, D.S., Goupal, N.K.J.M., and Park, C., "Measurement and Analysis of Nitric Oxide Radiation in an Arc-Jet Flow,"AIAA Paper 93-2800, Orlando, Florida, July 1993.

[2] Watson, V.R. and Pegot, E.B., "Numerical Calculations for the Characteristics of Gas Flowing Axially Through a Constricted Arc," NASA TN D-4042, 1967.

[3] Nicolet, W.E., Shepard, C.E., Clark, K.C., Balakrishnan, A., Kesselring, J.P., Suchsland, K.E., and Reese, J.J., "Methods for the Analysis of High-Pressure, high Enthalpy Arc Heaters," AIAA paper 75-704, Denver, Colorado, 1975

[4] Nicolet, W.E., Shepard, C.E., Clark, K.C., Balakrishnan, A., Kesselring, J.P., Suchsland, K.E., and Reese, J.J., "Analytical and Design Study for a High-Pressure, High-Enthalpy Constricted Arc Heater," AEDC-TR-75-47, 1975.

[5] Park, C. and Lee, S.H., "Validation of Multi-Temperature Nozzle Flow Code NOZNT," AIAA Paper 93-2862, Orlando, Florida, July 1993.

[6 Palmer, G., "Enhanced Thermochemical Nonequilibrium Computations of Flow Around the Aeroassist Flight Experiment Vehicle," AIAA Paper 90-1772, 1990.

[7] Palmer, G., "Thermochemical Nonequilibrium Flow Computations of Flow Around the Aeroassist Flight Experiment," Journal of Thermophysics and Heat Transfer, Vol. 6, No. 3, 1992, pp. 405-411.

[8] Park, C., "Nonequilibrium Air Radiation (NEQAIR) Program: User's Manual," NASA Technical Memorandum 86707, 1985.

[9] Park, C., "Calculations of Nonequilibrium Radiation in the Fight Regimes of Aeroassisted Orbital Transfer Vehicles," Thermal Design of Aeroassisted Orbital Transfer Vehicles, Progress in Astronautics and Aeronautics, Vol. 96, edited by H. F. Nelson, AIAA, New York, 1985, pp. 395-418.
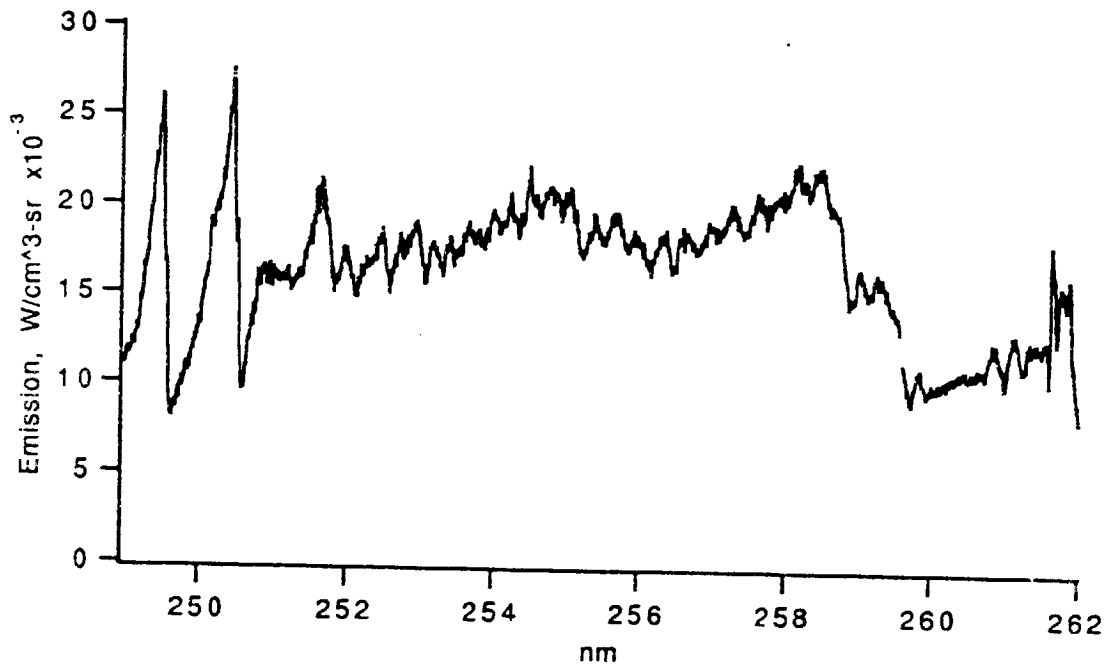
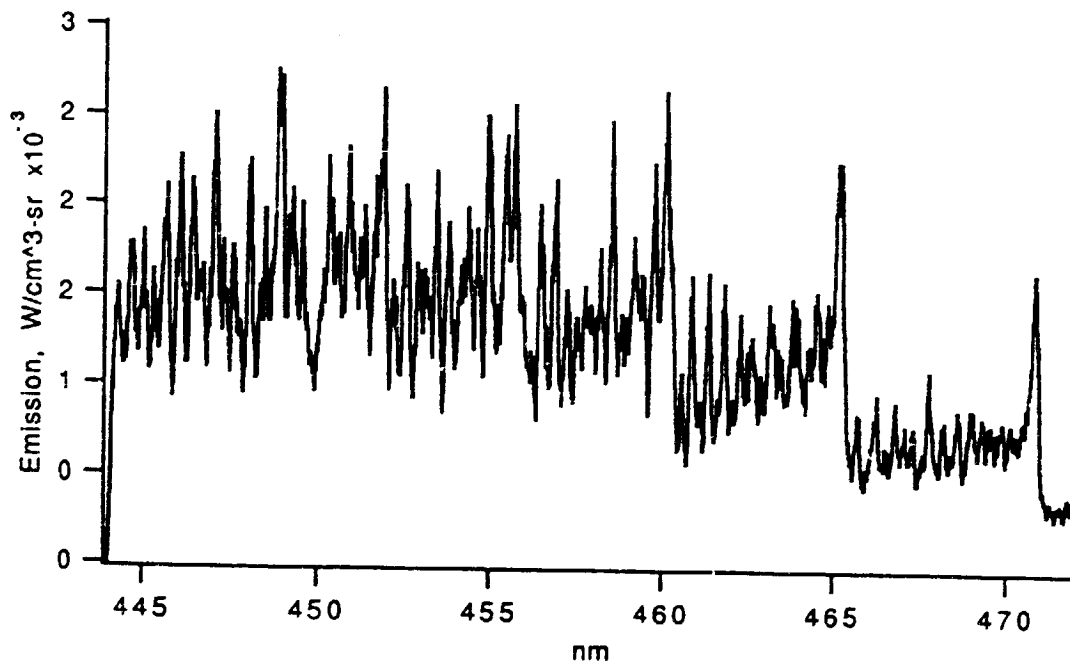**Fig. 1.** Measured emission trace from the 250 nm to 260 nm spectral range of the NO γ band system.

Fig. 2. Measured emission trace from the 440 nm to 470 nm spectral range of the N_2^+ First Negative band system.
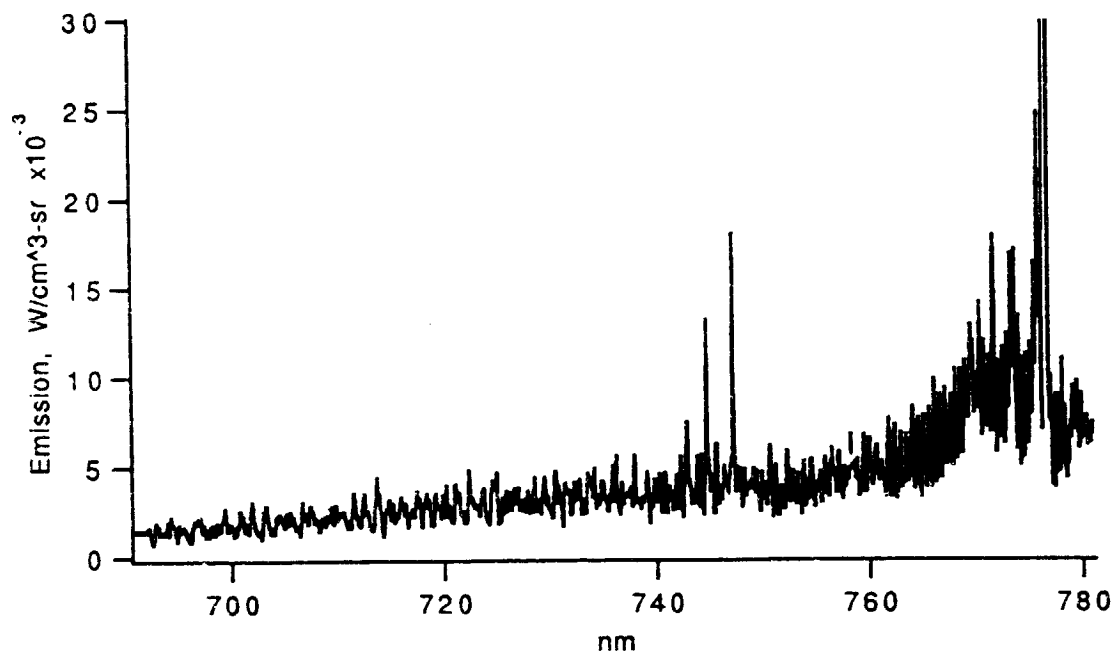
4

Fig. 3. Measured emission trace from the 700 nm to 800 nm spectral range of the N_2 First Positive band system.
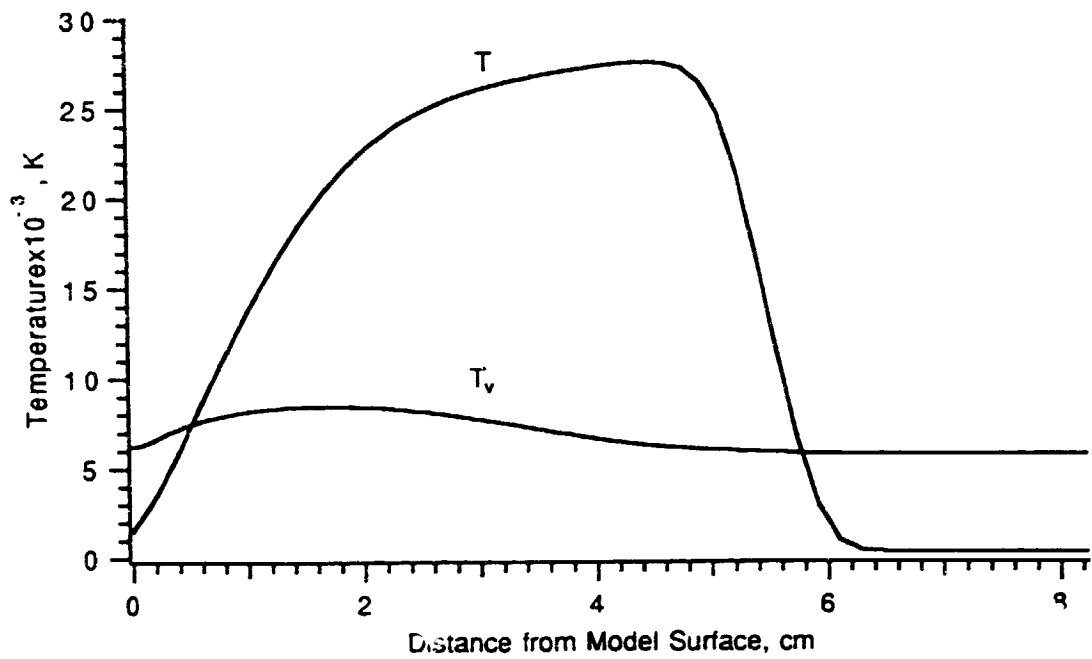

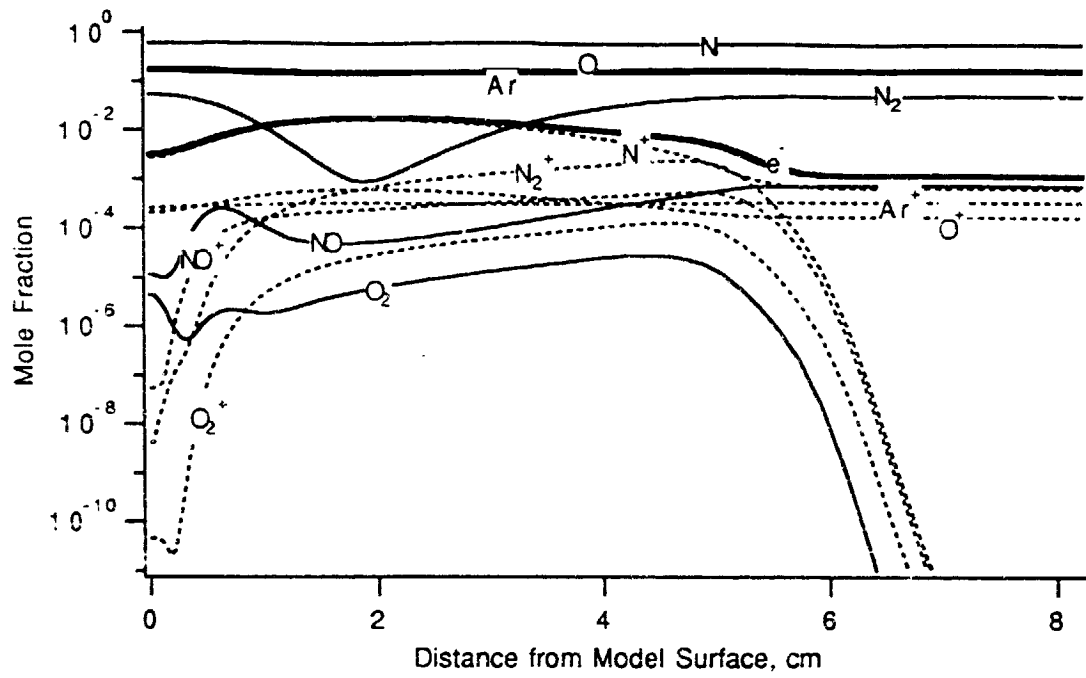**Fig. 4.** Calculated temperature profiles along the stagnation streamline.

Fig. 5. Calculated mole fractions along the stagnation streamline.

AIAA 93-2800

MEASUREMENT AND ANALYSIS OF NITRIC OXIDE RADIATION IN AN ARC-JET FLOW

Dikran S. Babikian
Eloret Institute
Palo Alto, CA 94303

Nigel K. J. M. Gopaul
Stanford University
Stanford, CA 94305

and

Chul Park
NASA Ames Research Center
Moffett Field, CA 94035

AIAA 28th Thermophysics Conference
July 6-9,1993 / Orlando, FL

MEASUREMENT AND ANALYSIS OF NITRIC OXIDE RADIATION IN AN ARC-JET FLOW

Dikran S. Babikian*
Eloret Institute, 3788 Fabian Way, Palo Alto, CA 94303
Nigel K. J. M. Gopaul**
Stanford University, Stanford, CA 94305
and
Chul Park[†]
NASA Ames Research Center, Moffett Field, CA 94035

Abstract

Radiation from the nitric oxide band systems emitted by the flow in the test section of a 20 MW arc-jet wind tunnel was measured and computed. The settling chamber pressure and enthalpy were 2.4 atm and 28 ± 10 MJ/kg, respectively. The measurements were made with a 0.3 meter McPherson spectrograph using photographic films in the wavelength region from 225 nm to 305 nm. Of the four band systems of NO (β, γ, δ, and ϵ), vibrational transitions were observed from only the upper $v' = 0$ levels. Excitation temperatures were deduced by comparing the experir ntal spectrum with those calculated using the nonequ. um radiation code NEQAIR. The rotational, vibratio l, and electronic excitation temperatures deduced from the data were: $T_r = 560 \pm 50°$ K, $T_v \leq 950 \pm 50°$ K, and $T_{ex} = 11500 \pm 520°$ K, respectively. A multi-temperature nonequilibrium nozzle flow code NOZNT was used to calculate the nozzle flow. The calculated temperatures were $T_r = 560°$ K, $T_v = 950°$ K, and electron thermal temperature $T_e = 6100°$ K, respectively at 30 MJ/kg. The sensitivity of the calculated temperatures to the uncertainty in the measured arc-jet enthalpy is examined.

Introduction

For the last three decades arc-jet wind tunnels have been used to simulate the high enthalpy environments encountered during hypervelocity atmospheric entry of space vehicles. The heat shields of all such vehicles, including those for the Apollo and the Space Shuttle vehicle, have been developed by testing in arc-jet wind tunnels. Testing of heat shield materials will become even more critical for the proposed Mars mission because the entry velocity will be higher than those for the past missions.

*Research Scientist; Member AIAA.

Mailing Address: NASA Ames Research Center, MS 230-2, Moffett Field, CA 94035.

**Graduate Research Assistant; Member AIAA.

[†]Staff Scientist; Associate Fellow. AIAA.

In spite of the importance of the arc-jet facilities, the aerothermodynamic states of the flows produced in them are not yet well understood. This is due to the complexity of the physical and chemical phenomena occurring in these facilities. The flow undergoes vibrational excitation, dissociation, and ionization. Because of the relatively low density environment produced in the facility, it is generally in nonequilibrium in both chemical composition and internal modes.

There have been some efforts to characterize the arc-jet flows by using the available experimental and computational techniques.[1,2] Despite such efforts, many uncertainties still exist. In particular there has not been a measurement of vibrational or e tronic temperatures of nitric oxide (NO). These temperatures of NO are important because NO plays an important role in the chemistry of the nozzle flows.[3]

The objectives of the present work are to experimentally characterize the behavior of NO and to explore whether it can be numerically reproduced. Radiation from NO was measured in the test section stream of a 20 MW arc-jet wind tunnel at NASA Ames Research Center. From the data, we determined its rotational, vibrational, and electronic excitation temperatures that are consistent with the limited data. The results of the measurements were compared with the theoretical calculations. These calculations included the computation of arc constrictor flow, nozzle flow, and nonequilibrium radiation. Due to the complex nature of the flow in the settling chamber, accurate prediction of the flow properties in this chamber remains uncertain and is under investigation.[4] The calculated temperatures and the synthetic radiation spectrum are generally in fair agreement with the measurements.

Experiment

Test Conditions and Experimental Setup

The arc heater of the 20 MW arc-jet wind tunnel at NASA Ames Research Center used in the present work (Aerodynamic Facility) consists of a constrictor tube that is 216 cm lon with a 6 cm internal diameter. The constrictor is followed by a settling chamber 10.4 cm in diameter and 25.6 cm in length. From the settling chamber, the flow is expanded through a convergent-divergent nozzle of throat diameter 3.81 cm, to an exit diameter of 45.72 cm with an 8° half angle and an area ratio of 130.

The arc heater was operated with a settling chamber pressure of 2.4 atm, a flow rate of 0.0864 kg/sec, electric

current of 2000 A and a voltage of 2600 V. The test gas consisted of 87% air and 13% argon by mass. The average value of the flow enthalpy based on heat balance measurements, i.e. electrical energy input minus the energy lost in the cooling water divided by the mass flow rate, was 22 MJ/kg. The flow enthalpy at the nozzle centerline based on heat transfer rate measurements to a spherical blunt body[5] was 28 MJ/kg.
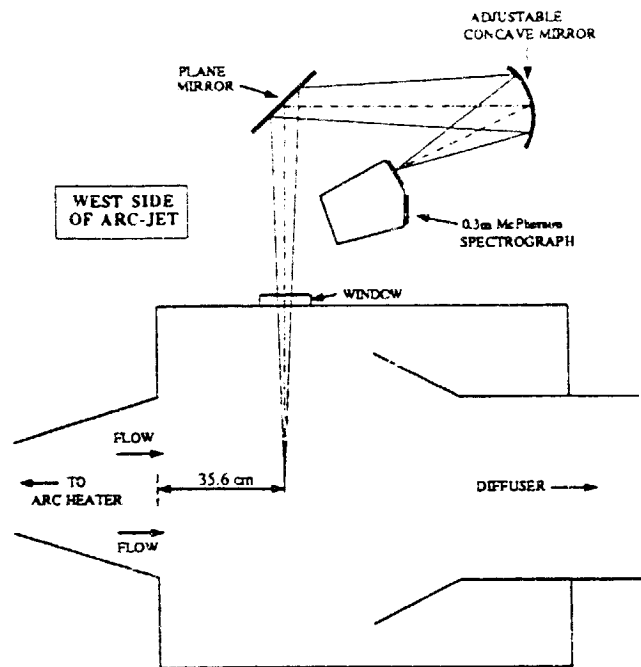

Fig. 1. Schematic drawing of the experimental set-up.

Spectral measurements were made in the freestream flow 35.6 cm downstream of the nozzle exit. Because of the low density nature of the expanding flow, the radiation emitted by the gas was very weak. Therefore in order to obtain sufficient signal, a McPherson spectrograph model 218 with a small f-number and a short focal length was used to collect the data. The spectrograph has an f-number of 5.3 and a focal length of 0.3 meters. This spectrograph is known as a criss-crossed Czerny-Turner optical system[6]. It is an unconventional mounting arrangement where the light beam from the two mirrors and the plane grating are crossed in order to obtain a low f-number. The signal was recorded on a film on this instrument by an exposure of 30 sec. A Joyce Loebel microdensitometer model MK III CS was used to measure the optical densities recorded on a High Speed Infrared Film (HIE). The microdensitometer traces were digitized and transferred to a computer to be calibrated, analyzed, and compared with the theoretical predictions.

Further description of the experimental setup, instrumentation, data collection, and data calibration, are presented in References 7 and 8. Figure 1 shows the schematic sketch of the experimental optical set-up

Experimental Spectra

As can be seen from Fig. 1, the radiation observed by the spectrograph is an integration of the intensity along the optical path across the flowfield. However since radiation power is generally strongly dependent on the controlling temperatures, and since these temperatures are the highest along the centerline of the nozzle flow, it is likely that the observed spectra are representative of those in the centerline region of the nozzle flow.

The densitometer trace of the record taken in the spectral range 450 nm to 850 nm, in the first order, is shown in Fig. 2. According to the spectrum shown in Fig. 2, the only significant radiation emanates from NOγ and δ band systems (in second order).
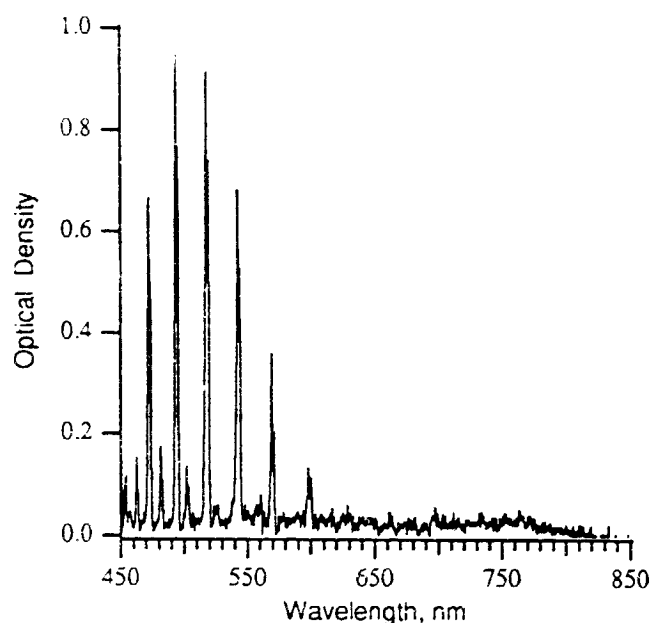

Fig. 2. Densitometer trace of the 450 nm to 850 nm (first order) spectral range.

The measured intensity was corrected for the film response in two steps using a National Bureau of Standards-certified calibrated lamp. First the film was calibrated for the relative intensity at specific wavelengths using neutral density step-wedge filters. Second the film was calibrated for the film sensitivity, the spectrograph grating, and the entire optical set-up against wavelength. Figure 3 shows the corrected intensity trace of the NO band systems adjusted to the first order in the 225 nm to 305 nm wavelength range.

As indicated in Fig. 3, the spectral bands detected by the spectrograph were identified as the NOγ and NOδ band systems in second order. The NOγ band system corresponds to the $A^2\Sigma^+ \rightarrow X^2\Pi$ transition where $A^2\Sigma^+$ is an upper electronic state and $X^2\Pi$ is the ground electronic state of the NO molecule. The NOδ band system is produced by transitions from the $C^2\Pi \rightarrow X^2\Pi$ electronic states. The NOβ band system ($B^2\Pi^+ \rightarrow X^2\Pi$), which is in the same spectral region as the NOγ band system (see

Fig. 4), was not present in the recorded spectrum. For both the γ and δ systems only the vibrational transitions from the upper, $v' = 0$, level were present: i.e. (0,1), (0,2), (0,3), etc.
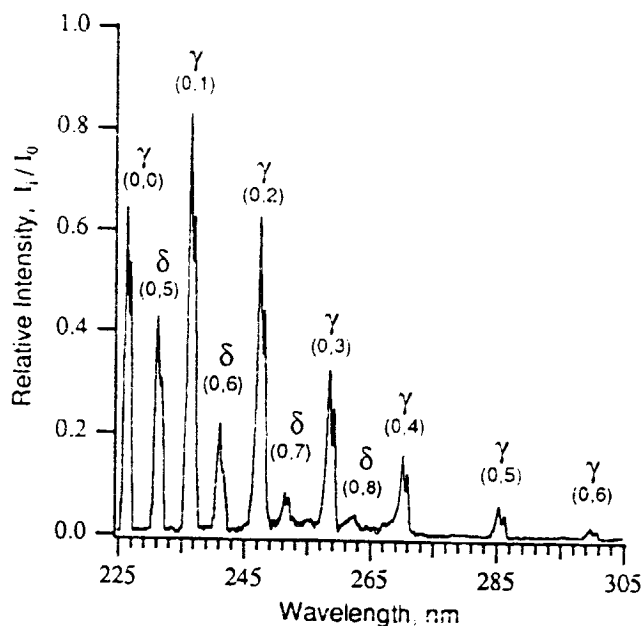

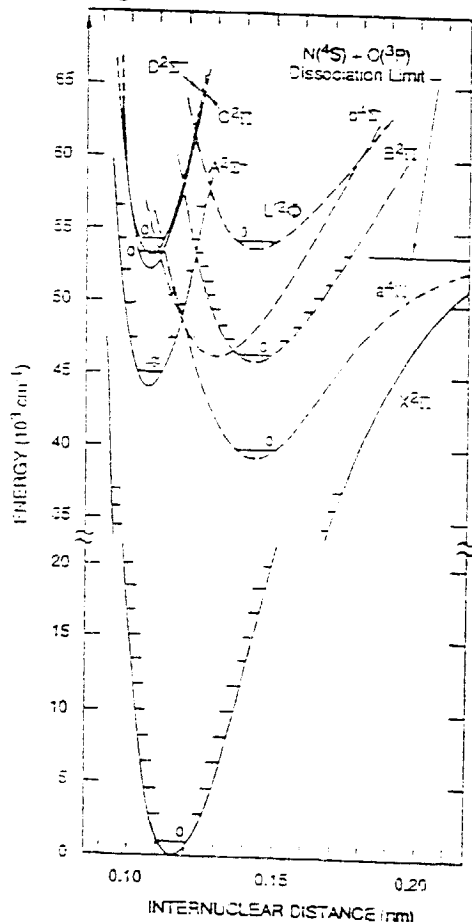Fig. 3. Corrected intensity trace of the 225 nm to 305 nm spectral range.

Fig. 4. Potential curves of the NO molecule.

Temperature Determination

The excitation temperatures of the flowfield were deduced by comparing the relative intensities in the recorded spectra with those calculated using the latest version of the nonequilibrium radiation code NEQAIR.[9,10] The code was used to calculate the emission spectra in the 225 nm to 305 nm range. The thermochemical model used in this code has been well documented in Refs. 11-14 and therefore will not be described here. The nonequilibrium excitation portion of the code was bypassed by specifying Boltzmann distributions of electronic, vibrational, and rotational excitation modes. Also, the radiation was very weak and the gas was assumed to be optically thin.

The width of a vibrational band is dictated mostly by the rotational temperature of the molecule. In the present work, the rotational temperature was determined from the (0,2) band of the γ system. The temperature was altered in the calculation until the calculated value of the band width at half its maximum intensity matched that of the experimental spectrum. The rotational temperature so determined was $T_r = 560 \pm 50°$ K. The source of the uncertainty $\pm 50°$ K is attributed to the uncertainties about film characteristics.[7,8] The ratio of the relative intensity of the δ system to that of the γ system depends on the electronic excitation temperature governing the two systems. Through a computational process similar to that used for the rotational temperature, an electronic excitation temperature of $T_{ex} = 11500 \pm 520°$ K was obtained. In Refs. 7 and 8, T_e was erroneously stated to be $7560\pm340°$ K. This error was caused by the use of the old values of intensity parameters (transition moments). To determine the vibrational temperature of NO, radiation from two vibrational levels is needed. However, only bands from $v' = 0$ state were observed in the data. From the fact that the radiation from the $v' = 1$ state of the upper electronic state of NOγ was absent in the observed spectrum, only the upper limit of the vibrational temperature of NO can be determined. In order for the radiation from the $v' = 1$ state be equal to or less than the observed noise level, the vibrational temperature was determined to be bellow $950\pm50°$ K.

Figures 5a and 5b show the calculated spectra of the radiation emitted by the NO band systems. In Fig. 5a the emission spectrum from the γ and δ systems is shown. This spectrum is in good agreement with the experimental spectrum shown in Fig. 3. The emission spectrum from the β and ϵ systems is shown in Fig. 5b. Note that the radiation from these systems is an order of magnitude weaker than that from γ and δ. Also, the β and ϵ systems are not present in the recorded spectrum shown in Fig. 3. The absence of the β band system indicates that the $B^2\Pi$ electronic state is not populated to a significant extent, although it is located at nearly the same energy level as the $A^2\Sigma^+$ state from which the γ system emanates (see Fig. 4). The $B^2\Pi$ state has a larger internuclear distance than the $A^2\Sigma^+$ state. The electronic states of the NO molecule may be populated through a selective populating process

according to internuclear distance under nonequilibrium.

The upper state of the NOϵ band system ($D^2\Sigma^+$) lies very close to the the upper state of the NOγ band system as shown in the energy potential curves in Fig. 4. However, the strong bands of NOϵ lie in the vacuum ultra-violet and only a few of the weaker bands are in the spectral region of our experiment. These weak vibrational bands (0,5), (0,6), and (0,7) lie under the much stronger vibrational bands (0,0),(0,1), and (0,2) of the NOγ system and their contribution to the measured radiation is insignificant. To verify the existence of NOϵ in the free stream flow, further emission measurements are needed in the vacuum ultra-violet spectral region where NOγ band system does not exist.

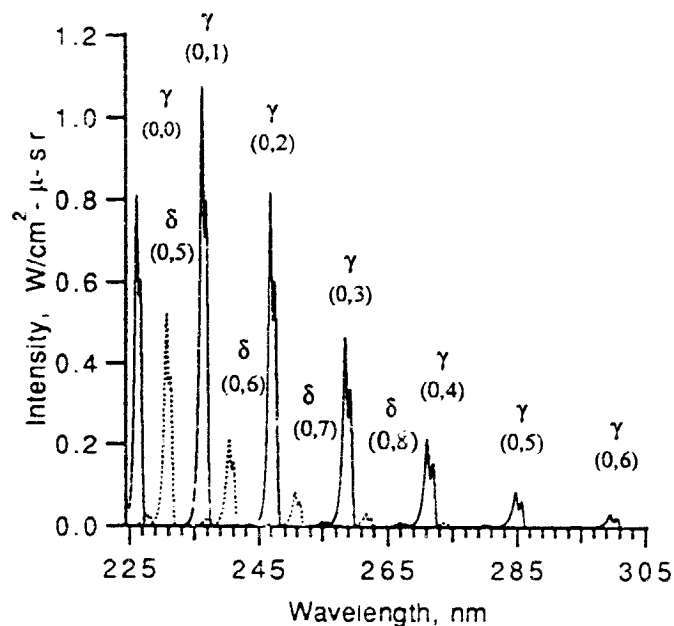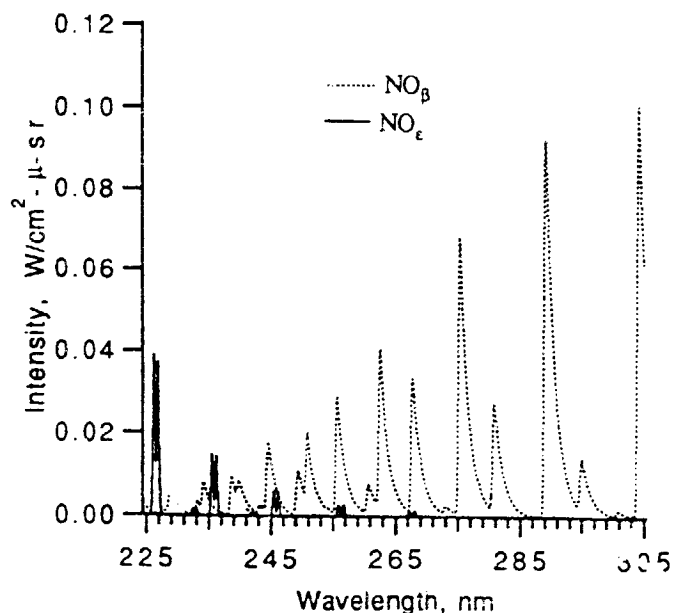Fig. 5. Calculated spectrum of NO; a) δ and γ band

Fig. 5. b) β and ϵ band systems.

Flowfield Calculations

Nozzle Inlet Conditions

In order to carry out the nozzle flow calculations, one must know the conditions at the nozzle entrance. The entrance condition is dictated by the flow processes in the settling chamber. Since the settling chamber receives its flow from the arc constrictor, one must first calculate the constrictor flowfield. The flow conditions at the exit of the constrictor were calculated using the arc heated flowfield code ARCFLO.[16,17] The code assumes the flow to be in thermochemical equilibrium and uses real gas properties.[16,18]
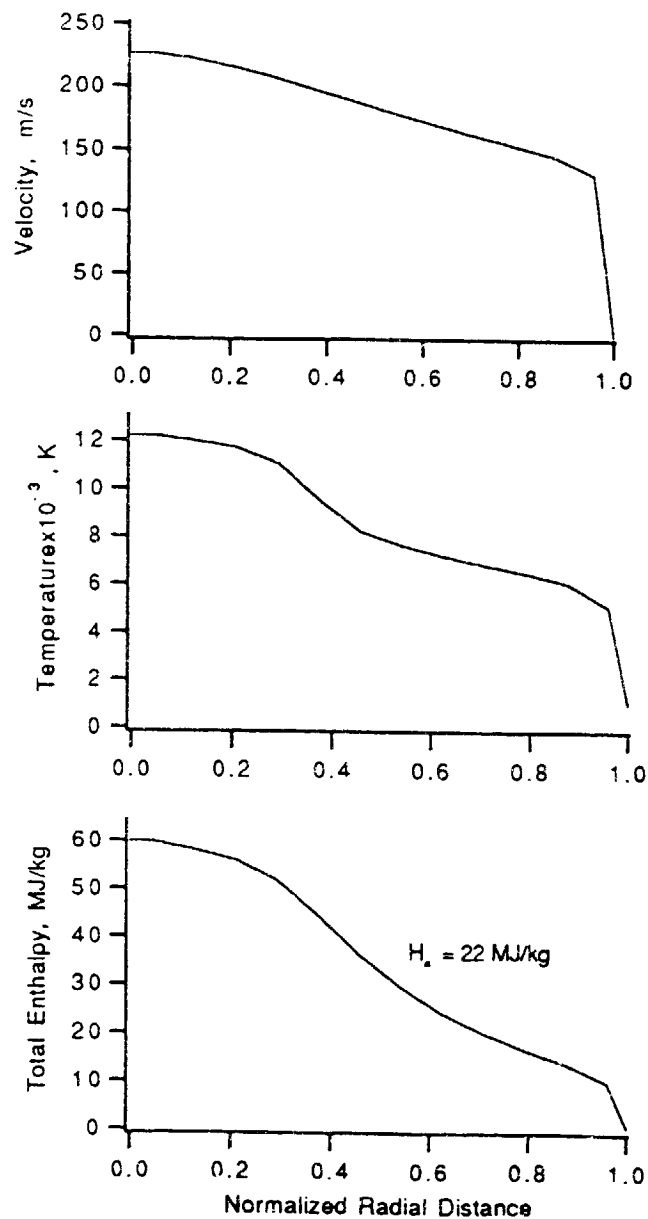

Fig. 6. Radial distribution of velocity, temperature, and enthalpy profiles.

Figure 6 shows radial distributions of velocity, temperature, and enthalpy at the exit of the constrictor. The

centerline values were 225 m/sec, 12200° K, and 60 MJ/kg respectively. The calculated mass averaged total enthalpy at the exit of the constrictor was 22 MJ/kg. The calculated averaged enthalpy value agrees with the value determined from heat balance. However, the calculated centerline enthalpy value is much greater than the value based on heat transfer rate.

The discrepancy between the two centerline enthalpy values is believed to be due to the circulation and mixing between the hot gas in the centerline region and the cold gas in the peripheral region. The resulting distribution of these properties in the settling chamber is difficult to predict, although an effort is presently being made to analyze it.[4] However. because of this phenomenon, it is expected that the distribution of temperature and enthalpy at its exit will be more uniform than that shown in Fig. 6. Therefore it is reasonable to assume the centerline enthalpy to be in the range of 28±10 MJ/kg.

In the present work, calculations were carried out for enthalpy values between 20 and 60 MJ/kg in an increment of 5 MJ/kg. The value of 30 MJ/kg, which is close to the 28 MJ/kg value deduced from heat transfer measurement, was used as the inlet enthalpy for the nozzle flow calculation.
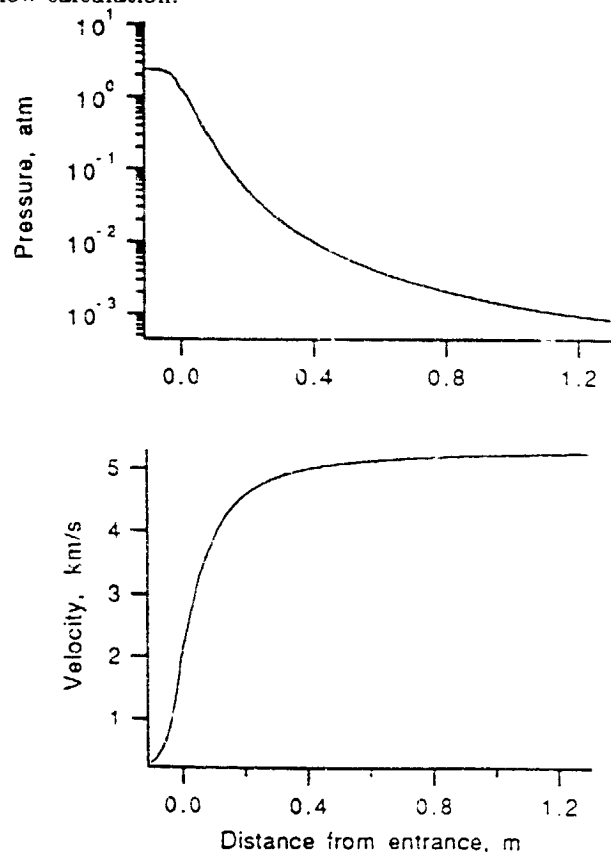

Fig. 7. Calculated velocity and pressure variation along the nozzle axis.

Nozzle Flowfield

The computer code NOZNT[2,15] was used to calculate the flow along the centerline of the nozzle of the arc-jet wind tunnel. The code solves a one-dimensional steady flow through a convergent-divergent nozzle in the dissociated and ionized regime. In the nozzle flow calculations. the nozzle geometry was assumed to be hyperbolic, that is, conical with a smooth transition at the throat, of the form $A/A^* = 1 + cx^2$. It assumes the entrance and the beginning section of the nozzle to be at equilibrium. The rest of the nozzle is solved assuming multi-temperature nonequilibrium flow. The equilibrium portion of the flow is solved with the pressure-specified method.[19]

The nonequilibrium calculations of the flow are started in the converging portion of the nozzle upstream of the throat. The nonequilibrium calculation also uses the pressure-specified method up to the point where the frozen Mach number is 1.8. From this point the area-specified method is used.[2] In this region of the flow the equations of conservation of species, vibrational energy, and electron-electronic energy are solved numerically.

Figure 7 shows the calculated pressure and velocity along the axis of the nozzle. The code assumes that the translational temperature T and rotational temperature T_r are the same. Likewise, the electron translation temperature T_e and electronic excitation temperature T_{ex} are taken to be the same. However, molecular species i are allowed to have different vibrational temperatures T_{v_i}.
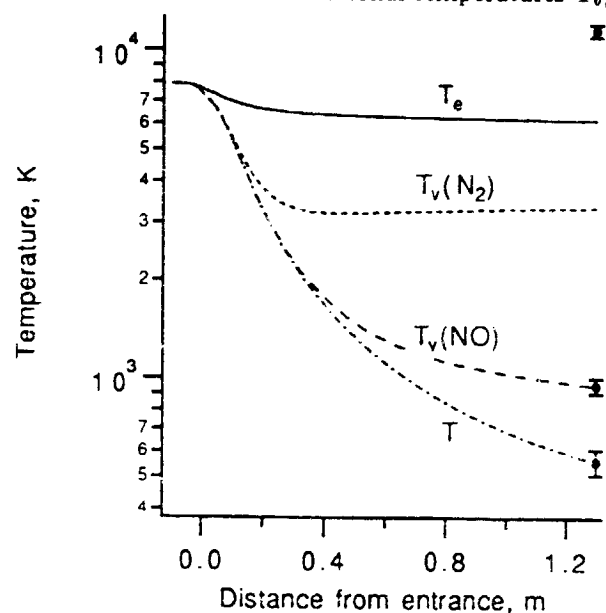

Fig. 8. Calculated excitation temperatures along the nozzle axis.

The reactions and excitation rates used in the code and solution procedure are discussed in Ref. 15. Those rate parameters were used in the present work except for those for ionic recombination of N^+ and O^+. Numerical difficulties were encountered for some calculations where enthalpy was higher than 45 MJ/kg. These difficulties disappeared when the ionic recombination rates were multiplied by 10. For the cases where there were no numerical difficulties, the change of the rate constants resulted in negligible differences. Since these rate constants are un-

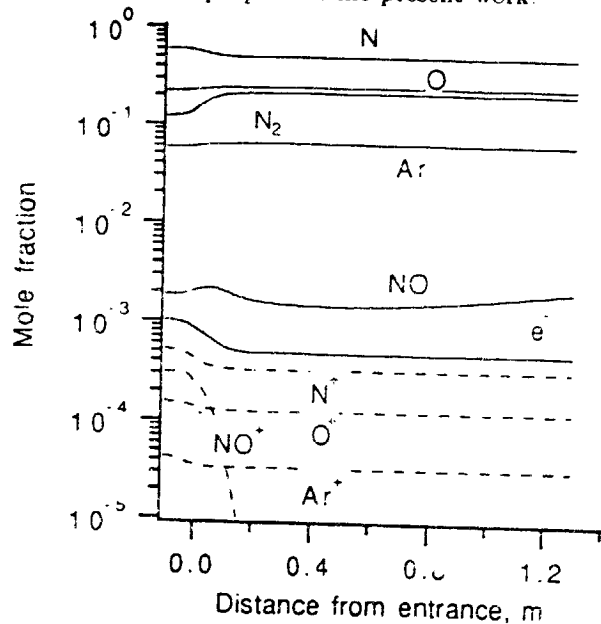certain by about an order of magnitude the changes are acceptable for the purpose of the present work.

Fig. 9. Calculated mole fractions along the nozzle axis.

Molecular oxygen was excluded from the calculations because it is almost entirely dissociated at the test conditions and its concentration is extremely small. Figures 8 and 9 show the temperature and mole fraction profiles along the nozzle axis. At the point where the experimental measurements were made, the calculated temperatures were $T_r = 560°$ K, $T_v(NO)=950°$ K, and $T_e = 6100°$ K at the enthalpy value of 30 MJ/kg.

Discussion

The excitation temperatures deduced from the experimental spectrum are shown in Fig. 8 by the circle symbols with error bars and are compared with the NOZNT calculation. The figure shows that the calculated translational-rotational and the NO vibrational temperatures are in good agreement with the corresponding experimentally deduced values. The difference between the measured T_{ex} and the calculated T_e may be due to the breakdown of the assumption that the two temperatures are equal. However both these temperatures, T_e and T_{ex}, are much higher than $T_v(NO)$. and thereby it underscores the need for a multi-temperature description of the flow. The vibrational temperature of N_2 was not measured in this experiment. However, the accuracy in the calculated value of $T_v(N_2)$ was verified in Ref. 2 by comparing it with experiments where N_2 vibrational temperature was measured.

In order to examine the sensitivity of calculated temperatures to the uncertainty in the measured arc-jet enthalpy, the foregoing calculations were repeated for different values of nozzle entrance enthalpies. The results are shown in Figure 10. It can be seen from the figure that, as the enthalpy increased from 20 MJ/kg to 60 MJ/kg, the

translational-rotational temperature increased from 550° K to 1500° K. However, the electron temperature reached a maximum value of 6200° K at H=35 MJ/kg and decreased thereafter as the enthalpy increased further. At enthalpies greater than 45 MJ/kg the electronic temperature and all vibrational temperatures are in equilibrium, whereas at enthalpies below 25 MJ/kg the translational temperature and the NO vibrational temperature are in equilibrium.
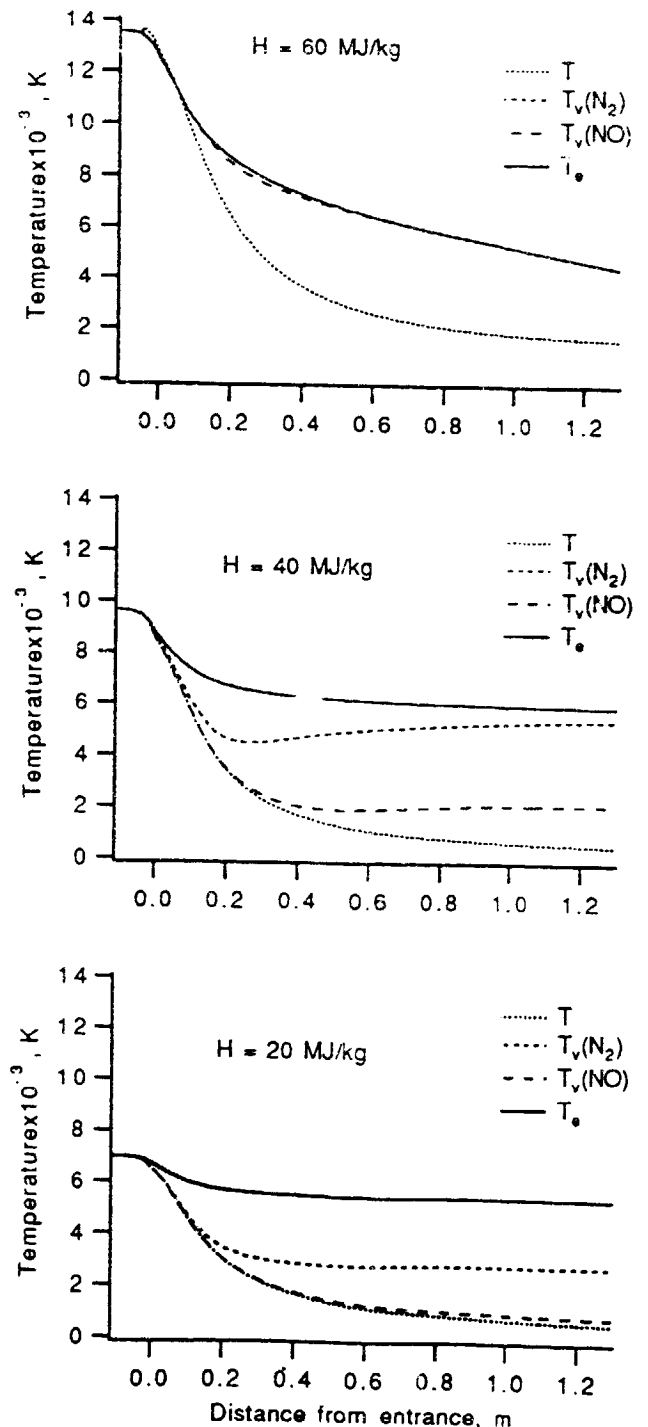

Fig. 10. Effect of inlet enthalpy on nozzle flowfield.

The value of $T_v(NO)$ found in the present experiment

indicates that the the enthalpy is below 35 MJ/kg. A previous work[20] indicates that the enthalpy value deduced from the heat transfer measurement tends to underestimate the enthalpy in typical arc-jet conditions. Therefore, the enthalpy is most likely between 28 MJ/kg, the value determined from the heat transfer measurement, and 35 MJ/kg. It is to be noted that at the enthalpy of 60 MJ/kg, which is the value of the enthalpy at the constrictor centerline, the concentration of NO is very small and it is unlikely that its radiation could be observed experimentally.

As shown in Ref. 20, enthalpy can be best determined spectroscopically by observing radiation emitted from the shock layer formed in front of a blunt body. Such effort is currently in progress. Measurements of the spectral radiation (120 nm to 900 nm) incident on the stagnation region surface of a blunt body in the test section have been made[21,22] and the analysis described in this paper is being extended to include the shock layer modeling. Preliminary predictions of the incident radiation spectrum have been made and are being compared with the experimental data.[23,24] Results of this analysis will be used to define future arc-jet tests to continue development of arc-jet wind tunnel modeling. A validated model of these facilities will help design advanced arc-jet and extend their usefulness as aerothermodynamic testing facilities.

Conclusions

The presented results show that by using the centerline enthalpy value deduced from heat transfer measurement and the NOZNT code, one can predict the free stream conditions in an arc-jet wind tunnel flow fairly well. The translational-rotational temperature and the vibrational temperature of NO can be closely reproduced by NOZNT. The calculated electron-electronic temperature T_e is appreciably lower than the measured electronic excitation temperature T_{ex} of NO. Compared with the electron and electronic temperatures, the vibrational temperature of N_2 and NO are significantly lower at enthalpies less than 45 MJ/kg. In the same enthalpy range, the vibrational temperature of NO is significantly lower than that of N_2. The enthalpy deduced from the spectroscopic measurements agrees approximately with that deduced from heat transfer measurement.

Acknowledgment

References

[1]Scott, D. C., "Survey of Measurements of Flow Properties in Arcjets," *Journal of Thermophysics and Heat Transfer*, Vol. 7, No. 1, January-March 1993, pp. 9-23.

[2]Park, C., and Lee, S. H., "Validation of Three-Temperature Nozzle Flo Code NOZ3T," AIAA Paper 93-2862, Orlando, FL, 1993.

[3]Olenberg, R., Chinitz, W., Friedman, M., Jaffe, R., Jachimowski, C., Rabinowit M., and Scott. G., "Hypersonic Combustion Kinetics Status Report of the Rate Constant Committee, NASP High Speed Propulsion Technology Team," NASP Rate Constant Committee, NASP TM-1107, 1990.

[4]Durgapal, P., and Palmer, G., "Strongly Coupled Radiative Transfer and Joule Heating in the Cathode of an Arc Heater," AIAA Paper 93-2801, Orlando, FL, 1993.

[5]Winovich, W., Balboni, J., and Balakrishnan, A., "Application of Numerical Simulation to Enhance Arc-Jet Performance Simulation," AIAA Paper 85-1006 Williamsburg, VA, 1985.

[6]Mcpherson Instruments, "Instruction Manual for Model 218, 0.3 Meter Combination Scanning Monochromator and Spectrograph," Acton, MA. USA.

[7]Gopaul, N. K. J. M., Spectral Measurement of Nonequilibrium Nitric Oxide in the Free-Stream of an Arc-Jet Flow," Degree of Engineer Thesis, Stanford University, 1992.

[8]Gopaul, N. K. J. M., "Spectral Measurement of Nonequilibrium Arc-Jet Free-Stream Flow," ISA Paper 93-144, Albuquerque, NM 1993.

[9]Park, C., "Nonequilibrium Air Radiation (NEQAIR) Program: User's Manual," NASA TM 86707, 1985.

[10]Moreau, S., Laux, C., Chapman, D. R., and MacCormack, R. W., "A More Accurate Nonequilibrium Air Radiation Code: NEQAIR Second Generation," AIAA Paper 92-2968, Nashville, TN, 1992.

[11]Park, C. "Calculation of Nonequilibrium Radiation in the Flight Regimes of Aeroassisted Orbital Transfer Vehicles," *Thermal Design of Aeroassisted Orbital Transfer Vehicles:* Progress in Astronautics and Aeronautics, Vol. 96, edited by H. F. Nelson, AIAA, New York, NY, 1985, pp. 395-418.

[12]Park, C., "Assessment of Two-Temperature Kinetic Model for Dissociating and Weakly-Ionizing Nitrogen," *Journal of Thermophysics and Heat Transfer*, Vol. 2, No. 1, January 1988, pp. 8-16.

[13]Park, C., "Assessment of Two-Temperature Kinetic Model for Ionizing Air," *Journal of Thermophysics and Heat Transfer*, Vol. 3, No. 3, July 1989, pp. 233-244.

[14]Whiting, E. E., and Park, C., "Radiative Heating at the Stagnation Point of the Aeroassisted Flight Experiment Vehicle," NASA TM 102829, 1990.

[15]Park, C., "Users Manual for NOZ3T, The Three-Temperature Nonequilibrium Nozzle Flow Code." NASA Ames Research Center, 1992.

[16]Watson, V. R., and Pegot, E. B., "Numerical Calculations for the Characteristics of Gas Flowing Axially Through a Constricted Arc," NASA TN D-4042, 1967.

[17]Nicolet, W. E., Shepard, C. E., Clark, K. C., Balakrishnan, A., Kesselring, J. P., Suchsland, K.E., and Reese, J.J., "Methods for the Analysis of High-Pressure, High-Enthalpy Arc Heaters," AIAA paper 75-704, Denver, CO, 1975.
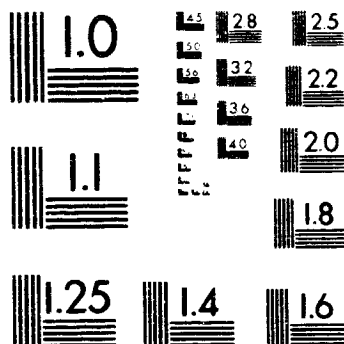
94-35498 UNCLAS

MICROCOPY RESOLUTION TEST CHART
NATIONAL BUREAU OF STANDARDS
STANDARD REFERENCE MATERIAL 1010a
(ANSI and ISO TEST CHART No. 2)

[18]Stine, H. A., and Watson, V. R., "The Theoretical Enthalpy Distribution of Air in Steady Flow Along the Axis of a Direct-Current Electric Arc," NASA TN D-1331, 1962.

[19]Lordi, J. A., Mates, R. E., and Moselle, J. R., "Computer Program for the Numerical Solution of Nonequilibrium Expansions of Reacting Gas Mixture," NASACR-172, 1972.

[20]Okuno, A. F., and Park, C., "Stagnation-Point Heat-Transfer Rate in Nitrogen Plasma Flows: Theory and Experiment," *Journal of Heat Transfer*, Vol. 92, Ser. C, NO. 3, August 1970, pp. 372-384.

[21]Palumbo, G., Craig, R., and Carrasco, A., "Spectral Measurements of Shock Layer Radiation in an Arc-Jet Wind Tunnel," ISA Paper 93-145, Albuquerque, 1993.

[22]Craig, R., Palumbo, G., and Carrasco A., "VUV Shock Layer Radiation in an Arc-Jet Wind Tunnel Experiment," Will be submitted for the 18th Aerospace Ground Testing Conference, Colorado Springs, CO, 1994.

[23]Babikian D. S., Craig, R., Palumbo, G., and Palmer, G., "Measured and Calculated Spectral Radiation from a Blunt Body Shock Layer in an Arc-Jet Wind Tunnel." Proposed Paper for the AIAA 32th Aerospace Sciences Meeting, Reno, NV, 1994.

[24]Babikian, D. S., Craig, R., Palumbo, G., and Palmer, G., "Predictions and Measurements of VUV Radiation from a Blunt Body Shock Layer in an Arc-Jet Wind Tunnel," Will be submitted for the 18th Aerospace Ground Testing Conference, Colorado Springs, CO, 1994.

C-2

AIAA-92-2973

NUMERICAL SIMULATIONS OF NONEQUILIBRIUM SHOCK LAYERS WITH HIGHLY EFFICIENT IMPLICIT SCHEMES

Jean-Luc Cambier and Dinesh K. Prabhu
Eloret Institute
Palo Alto, CA

AIAA 23rd
Plasmadynamics & Lasers Conference
July 6-8, 1992 / Nashville, TN

NUMERICAL SIMULATIONS OF NON-EQUILIBRIUM SHOCK LAYERS WITH EFFICIENT IMPLICIT SCHEMES

Jean-Luc Cambier * Dinesh K. Prabhu †

Eloret Institute, 3788 Fabian Way, Palo Alto, California 94303

Abstract

Current and future calculations of nonequilibrium shock layers require the use of a very large number of equations, due to a multiplicity of chemical species, excited states, and internal energy modes. The computational cost associated with the use of standard implicit methods becomes prohibitive; it is, therefore, desirable to examine the potential of several methods and determine if any can be projected to be more efficient and accurate for large systems of equations. In this paper we examine the performance of several implicit schemes on some simple practical examples of reacting flows. The Euler equations are solved by three different implicit methods, and two methods of coupling between the fluid dynamics and the chemistry are studied. Several cases of stiffness are considered, and both one and two-dimensional examples are computed. We conclude on with some remarks on the accuracy, stability and efficiency of these various methods.

I. Introduction

The modern Computational Fluid Dynamics (CFD) tools are becoming increasingly useful in computing complex flow conditions, which generally include non-equilibrium phenomena. There is a general need for increasingly complex modeling of the thermo-chemical properties of the gas, and for the modeling of larger systems. For example, the modeling of shock layers around ablating bodies requires a very large set of chemical species and chemical reactions. Although some approximate formulations can be used in the preliminary design phase of space vehicles or experiments, the modeling of the complete kinetics is desirable or even required when the non-equilibrium effects become dominant: this happens for example as the flow expands around the shoulder of a vehicle, or when the object is reduced in

size for insertion into an experimental facility. The situation can be further complicated due to the fact that most flows realized in ground-based experimental facilities are themselves not in chemical or thermal equilibrium. Another example concerns highly ionized and radiating flows, which are likely to be found at high re-entry velocities, or their equivalent. It may be required, for these cases of plasma conditions, to account for non-Boltzmann distribution of the excited states. This problem may also require us to model the plasma with a complete collisional-radiative model of the plasma, and convect all the excited states, forcing us to use a large number of equivalent species. In addition, the internal relaxation processes will be locally stiff and difficult to model. These upcoming challenges in CFD technology will require the development of efficient methods for a very large number of species, and for possibly stiff couplings to complex internal processes. Since we want a method that allows us to reach the steady state with minimal computational effort, it seems desirable to use an implicit method. On the other hand, since we may need to couple the hydrodynamics to several other physical processes (collisional-radiative processes, radiation transport, electro-magnetic couplings, etc..), we may favor the use of the Operator-Splitting (OS) method. The latter must be contrasted with the Fully-Coupled (FC) approach, which attempts to provide a more accurate and more stable way to couple the different processes. It is not clear a priori which method is more accurate, stable, efficient, or practical; the use of one method versus the other may depend on the type of flows being computed, the type of computer architecture used, or even the personal preferences of the modeler. During the course of the present work, we will compare the FC and OS methods (for chemistry) and therefore add fuel to the debate. Our search for an efficient numerical method, extendable to large systems, will also include the effect of required grid accuracy on the solution, and its impact on the efficiency of the numerical approaches used.

*Senior Research Scientist, member AIAA. Mailing address: NASA Ames Research Center, MS 230-2, Moffett Field, California 94035.

†Research Scientist, member AIAA

II. Numerical Methods

II-A: The $N \times N$ Block-Tridiagonal method

The Euler equations describe the convective process, and are written (in 1D) as:

$$\frac{\partial}{\partial t} \begin{pmatrix} \rho_1 \\ \vdots \\ \rho_n \\ \rho u \\ E \end{pmatrix} + \frac{\partial}{\partial x} \begin{pmatrix} u\rho_1 \\ \vdots \\ u\rho_n \\ P + \rho u^2 \\ uH \end{pmatrix} = 0 \qquad (1)$$

where E, H are respectively the total energy and total enthalpy, per unit volume. The internal energy is $E_i = \sum_s \rho_s \int^T dT' C_{v,s}(T')$, and the gas mixture follows the ideal equation of state:

$$P = NkT = (\gamma - 1)E_i = (\gamma - 1)(E - \frac{1}{2}\rho u^2)$$

The individual species densities are denoted by ρ_s, and $\rho = \sum_s \rho_s$. This formulation is for a single fluid (one mass-averaged velocity), in thermal equilibrium (one temperature). This equation is discretized over a finite size mesh to yield the form:

$$\frac{\Delta Q_i}{\Delta t} = F_{i-\frac{1}{2}} - F_{i+\frac{1}{2}} \qquad (2)$$

where

$$Q = \begin{pmatrix} \rho_1 \\ \vdots \\ \rho_n \\ \rho u \\ E \end{pmatrix} \cdot \mathcal{V} \qquad F = \begin{pmatrix} u\rho_1 \\ \vdots \\ u\rho_n \\ P + \rho u^2 \\ uH \end{pmatrix} \cdot \mathcal{S}$$

The subscripts $i, i \pm \frac{1}{2}$ indicate that the variables are evaluated at computational cells (center) i, and cell interfaces $i \pm \frac{1}{2}$. $\mathcal{V}$ and $\mathcal{S}$ are respectively the cell volumes and surfaces. This finite-volume formulation will be used throughout the paper. The equation has been discretized in time as well, and the expression ΔQ describes the difference between the flow variable evaluated at two time levels, n and $n + 1$. The expression on the RHS of equation (2) must be further specified: the fluxes are a function of Q, and can be evaluated at time level $n + \theta$ through the linearization approximation:

$$F_{i+\frac{1}{2}}^{(n+\theta)} \simeq F_{i+\frac{1}{2}}^{(n)} + \theta A(Q)(\Delta Q)_{i+\frac{1}{2}} \qquad (3)$$

where $A = \frac{\partial F}{\partial Q}$ is the Jacobian matrix. The explicit Euler system of equations is obtained for $\theta = 0$, the implicit system for $\theta = 1$, while second-order time accuracy is obtained for $\theta = 1/2$. Second-order spatial accuracy is achieved by evaluating the fluxes at the cell interfaces $i \pm \frac{1}{2}$:

$$F_{i \pm \frac{1}{2}} = \frac{1}{2}(F_i + F_{i \pm 1})$$

A final modification to the fluxes is made to assure monotonicity. The Euler system is a hyperbolic system, and has a set of real eigenvalues (characteristic speeds). The Jacobian can then be written in the form:

$$A = T^{-1} \cdot \Lambda \cdot T \qquad (4)$$

where the matrix of eigenvalues

$$\Lambda = \begin{pmatrix} u & & & & \\ & \ddots & & & \\ & & u & & \\ & & & u + c & \\ & & & & u - c \end{pmatrix} \qquad (5)$$

is diagonal and real only, T, T^{-1} are transfer matrices between the space of primitive variables Q and 'characteristic' variables, and c is the speed of sound. The spectrum of eigenvalues can be split into and positive and negative values, which indicate the direction of flow of the characteristic variables at the cell interface. The flux at an interface can now be written as:

$$F_{i+\frac{1}{2}}^{(n+\theta)} \simeq F_{i+\frac{1}{2}}^{(n)} + \theta A^+(Q)\Delta Q_i + \theta A^-(Q)\Delta Q_{i+1} \qquad (6)$$

where

$$A^\pm = T^{-1} \cdot \Lambda^\pm \cdot T$$

and $A^\pm$ is the set of eigenvalues which are respectively positive (negative), zero otherwise. Using this formulation, the discretized version of the Euler equations becomes:

$$[-\theta \Delta t A_{i-\frac{1}{2}}^+] \Delta Q_{i-1}$$
$$+[1 + \theta \Delta t A_{i+\frac{1}{2}}^+ - \theta \Delta t A_{i-\frac{1}{2}}^-] \Delta Q_i \qquad (7)$$
$$+[\theta \Delta t A_{i+\frac{1}{2}}^-] \Delta Q_{i+1} = F_{i-\frac{1}{2}}^{(n)} - F_{i+\frac{1}{2}}^{(n)}$$

The RHS of equation (7) can be modifed for monotonicity, while conserving its second-order accuracy in space. The technique used throughout this work follows closely the TVD method of Harten [1]. Greater stability is generally obtained if the implicit LHS of equation (7) has its spatial accuracy reduced to first order. This consists in evaluating the Jacobian matrices at the cell centers, according to the

characteristic flow direction. The final version of the system is obtained for the fully implicit case ($\theta = 1$):

$$[-\mathbf{A}^+_{i-1}\Delta t]\Delta\mathbf{Q}_{i-1}$$
$$+[1 + \mathbf{A}^+_i\Delta t - \mathbf{A}^-_i\Delta t]\Delta\mathbf{Q}_i \qquad (8)$$
$$+[\mathbf{A}^-_{i+1}\Delta t]\Delta\mathbf{Q}_{i+1} = RHS^{(n)}$$

This is a tridiagonal system of $N \times N$ block matrices, where $N = N_s + D + 1$, N_s is the number of species, D is the spatial dimensionality. Solving this system can be done by the standard technique of gaussian elimination and back substitution, with LU decomposition of the block matrices (see for example [2]). This requires that the matrices that compose the diagonal band be inverted twice for each grid point. It turns out that the corresponding algorithm has a number of operations that scales as N^3. This technique is called the $N \times N$ Block-Tridiagonal solve, and will be used in this paper.

A similar approach can be used for 2-dimensional flow, leading to a pentadiagonal system of $N \times N$ bock matrices. Another approach, which consumes less memory and has a lower number of operations, uses the technique of dimensional splitting [3]: we effectively solve the tridiagonal system twice, once for each direction[†]. This is the approach used here.

II-B: The Scalar Tridiagonal method

It is clear that as the number of species grows, the N^3 dependence of the computational load will rapidly make this technique impractical. It is desirable then to search for a method that scales less rapidly with the number of species. One such method can be easily obtained by considerable simplification of the matrix structure. Note that the split Jacobians are bounded respectively from below and above:

$$\mathbf{A}^+ = \mathbf{T}^{-1}.\mathbf{A}^+.\mathbf{T} < \max\{\lambda\}\cdot\mathbf{1} \qquad (9)$$

$$\mathbf{A}^- = \mathbf{T}^{-1}.\mathbf{A}^-.\mathbf{T} > \min\{\lambda\}\cdot\mathbf{1} \qquad (10)$$

where we have used the (signed) maximum and minimum eigenvalue present in $\mathbf{A}$. The Jacobian matrices, thus replaced into equation (8) are proportional to the unit matrix. There is only a scalar operation to perform, instead of a full block matrix inversion. The number of operations now scales as N: this scheme is called the Scalar-Tridiagonal solver, and will be compared to the previous one.

There are several disadvantages to the scalar technique: the first, loss of time accuracy, is not of immediate relevance, since we are mostly concerned with the achievement of steady-state. The second is a loss of accuracy: this is specially of concern in subsonic regions, where the spectrum of eigenvalues is originally very different from the maximum (minimum) value. In supersonic or hypersonic regions, this is not a problem, since $u >> c$, and $\Lambda \simeq u1$, i.e the spectrum is nearly scalar. We may expect therefore some loss of accuracy, or even stability, when using the scalar method.

II-C: The N_s-Split Tridiagonal method

We will also investigate another method, based on the formulation of a multi-fluid system of equations. Let us consider the following system of equations:

$$\frac{\partial}{\partial t}\left(\begin{array}{c}\rho_s\\\rho_s u\\E_s\end{array}\right) + \frac{\partial}{\partial x}\left(\begin{array}{c}u\rho_s\\P_s + \rho_s u^2\\uH_s\end{array}\right) = 0 \qquad (11)$$

and similar systems for other species. In this formulation, each species is attributed its own momentum density and energy density. In the limit of very strong coupling between the momentum and energy densities of each fluid component, we can enforce a unique velocity and unique temperature for this multi-fluid description. If we were to solve each subsystem by the block tridiagonal method, we would require the inversion of a 3×3 (4×4 in 2 dimensions) matrix. We repeat the method for each species, and the overall cost now scales as N_s. For a large number of species, we expect a cross-over between this method and the $N \times N$ block method, by comparing the costs; for example, $4^3 N_s$ versus $(N_s + 3)^3$. However, a further reduction in cost can be achieved with the following approximation. Assuming that all species have nearly equal molecular masses, and that their individual specific heats are nearly equal, we can replace the partial pressure:

$$p_s = n_s \dot{R}T \simeq \frac{\rho_s}{\rho}P$$

and use a constant average $\bar{\gamma}$ in the formulation of the derivatives which compose the Jacobians. These Jacobian matrices become then identical. This has a rather drastic effect: the block matrix inversions need to be performed once, instead of once for each species. This lowers considerably the overall CPU requirement. This formulation of the solver will be called N_s-Split Tridiagonal solver, and will compared with the two previous ones.

[†]This splitting is a form of Operator-Splitting.

II-D: Hydrodynamics-Chemistry Coupling

In the equations considered so far, the source terms on the RHS are non existent; for a reacting gas, there will be a source term $\dot{\mathbf{W}}$ which operates on the species densities only. The total energy now includes the energies of formation:

$$E = E_i + \frac{1}{2}\rho u^2 + \sum_s e_s^{\circ}$$

and is not not affected by the chemical reactions the internal energy is obtained from the conserved total energy, after subtracting the kinetic and formation energies. The change in formation energy of the mixture, due to chemical reactions, will thus be converted into a change of temperature.

The chemical source term can be treated implicitly as well: if Ω is the corresponding Jacobian for the source term ($\Omega = \frac{\partial \mathbf{W}}{\partial \mathbf{Q}}$), solving for the chemistry alone would read as:

$$[1 + \Omega_i \Delta t]\Delta_{ch}\mathbf{Q} = \dot{\mathbf{W}}_i^{(n)}\Delta t \qquad (12)$$

By solving separately for the convective and chemical terms, one obtains two variations at the end of the computational step: the global variation will then be a direct sum of the the contribution from each process.

$$\Delta\mathbf{Q} = \Delta_{cv}\mathbf{Q} + \Delta_{ch}\mathbf{Q} \qquad (13)$$

This procedure is called[†] the Explicit-Coupling method (EC).

We see that in effect, we have split the computation in two parts, for each physical process. For that reason, this method is also called the Operator-Splitting (OS) method (see for example [3]). Another form of operator splitting consists in using the change induced by one process as a starting point for the other process: a temporary solution $\mathbf{Q}$ is used, such that:

$$\tilde{\mathbf{Q}} = \mathbf{Q}^{(n)} + \Delta_{cv}\mathbf{Q} \qquad (14)$$

$$\mathbf{Q}^{(n+1)} = \tilde{\mathbf{Q}} + \Delta_{ch}\tilde{\mathbf{Q}} \qquad (15)$$

where now the change induced by chemistry is obtained by using the modified solution $\tilde{\mathbf{Q}}$ in the expression of the source term and Jacobian, $\dot{\mathbf{W}}, \Omega$ in eq. (12). This formulation of the Operator-Splitting method is based on fractional steps, and is best described in [4]. Since we will examine both methods, we will reserve the term Explicit-Coupling (EC)

---

† Also called the Loosely-Coupled approach.

for the method described in eq. (13), and the term Operator-Splitting (OS) when using the method described by eqs. (14) and (15).

Another approach is to solve for both the convective and chemical processes simultaneously. The chemical Jacobians can be brought into the LHS, and equation (8) is modified to:

$$[-\mathbf{A}_{i-1}^{+}\Delta t]\Delta\mathbf{Q}_{i-1}$$
$$+[1 + \mathbf{A}_i^{+}\Delta t - \mathbf{A}_i^{-}\Delta t + \Omega_i \Delta t]\Delta\mathbf{Q}_i \qquad (16)$$
$$+[\mathbf{A}_{i+1}^{-}\Delta t]\Delta\mathbf{Q}_{i+1} = RHS^{(n)}$$

where now the RHS includes the evaluation of the chemical source terms at time level (n). This method is called the Implicit, or Fully-Coupled (FC) approach. The Ω matrix is dense, and the FC approach described above is possible only when combined with the $N \times N$ Block-Tridiagonal solver. Including it in the N_s-Split solver would require serious modifications, and has not been attempted here. Similarly, by approximating the Jacobian Ω by a scalar (using again the maximum eigenvalue), one could use the FC approach with the Scalar Tridiagonal solver. We found that in many cases this approximation usually leads to very poor results for the chemistry, and will not be used here.

II-E: Chemistry Sub-Cycling

There are additional modifications one can make when using the OS or EC approaches: since the fluid dynamics and chemistry are computed separately for a global time step Δt, one has considerable flexibility in the methods used for each process. Notably, the accuracy of the chemistry can potentially be improved by sub-iterating (more precisely subcycling) the chemistry by using smaller time steps δt. This may be required to improve the accuracy, because the chemical reactions are non-linear processes: linearization errors become important in some highly non-equilibrium situations. The coupling of the chemistry to the temperature can also be estimated at each sub-step, by looking at the change induced in the average formation energy of the mixture. When the chemistry is sub-iterated (SI), the global variation is obtained by using eq. (13), but when the global change due to chemistry is obtained as follows, using sub-iterations ($m = 1, 2, \ldots$) of the chemistry:

$$\Delta_{ch}\mathbf{Q}^{(m+1)} = \Delta_{ch}\mathbf{Q}^{(m)} + [1 + \Omega\delta t]^{-1}\dot{\mathbf{W}}\delta t \quad (17)$$

Finally, the coupling of the chemistry to the convection can also be computed at each sub-step. For

example, after computing the variation $\Delta_{cv}Q$ using one of the Tridiagonal solver listed above, one can linearize it during the global time interval. The global variation (for both processes) is then obtained as follows:

$$\Delta Q^{(m+1)} = \Delta Q^{(m)} + [1 + \Omega \delta t]^{-1} \dot{W} \delta t \qquad (18)$$
$$+ \frac{\Delta_{cv}Q}{\Delta t} \delta t$$

This formulation replaces equation (13). We will reserve the term Sub-Iterated Coupling (SIC) to describe this particular form of the splitting method between chemistry and convection.

II-F: Performance

The methods used can be classified, according to the treatment of the convective process and the method of coupling with the chemistry: the designation of the methods which will be studied are listed in Table 1.

The relative performance of all schemes is demonstrated in Figure 1. Figure 1-a (top) shows the CPU spent (per iteration and per grid point) by an implicit method, normalized by the same quantity for the explicit method. Since the explicit method scales almost exactly as the number of equations, both the Scalar and the N_s-Split method will show a nearly flat behavior when plotted versus the number of species. This is confirmed in Figure 1-a. Notice also that the relative cost of the Scalar method is very small, while the $N \times N$ Block method climbs very rapidly: the latter is still quite expensive, even for a small number of species. The leftmost data point at $N_s = 5$, for example, shows that the $N \times N$ Block method is 10 times more expensive than the explicit method. Although this number is not an absolute, and can be reduced after a strong effort in code writing (by 'hard-wiring' the operations, for example). At best, this time may be reduced by a factor of two. Still, the conclusion is inevitable: as the number of species grows, the implicit scheme is efficient only if it can be operated at large CFL numbers. Practically speaking, stability limitations will limit the CFL to the neighborhood of 4-5. These stability problems arise from transient phenomena, dimensional split errors and/or coupling errors with the chemistry or other internal relaxation processes. Higher values of CFL number can potentially be achieved when the flow is very close to the steady state and when the flow is non-stiff. Since we are mostly interested into reaching the steady state (and having to go through the transients) and into stiff problems, this is of lit-

tle interest to us. These limitations will be demonstrated on some practical sample cases in the next sections.

III. One-Dimensional Shock

As a first test case, we will model the propagation of a 1-dimensional shock, from an impulsive start. This case will mimic the establishement of a two-dimensional shock layer around a blunt body. We use a grid of 200 cells, evenly spaced, with a perfectly reflecting wall on the right hand side. The flow is incoming from the left at high velocity, and impinges on the wall. A shock is created at the reflection and propagates back upstream into the hypersonic flow. Although strictly speaking this flow is unsteady, the profiles become steady in a frame attached to the shock. The gas is air, composed of 5 species (N, O, N_2, O_2, NO), the free stream Mach number is $M_\infty = 15$, the free-stream temperature is $T_\infty = 300^\circ K$. Three cases of free-stream pressure will be considered, leading to three stiffness conditions:

$$
\begin{aligned}
\text{case 1}: \quad & P_\infty = 10^{-5} \text{atm} \\
\text{case 2}: \quad & P_\infty = 10^{-4} \text{atm} \\
\text{case 3}: \quad & P_\infty = 10^{-2} \text{atm}
\end{aligned}
$$

The stiffness is defined as the ratio of the largest time scale (here presumably the convective one) to the smallest (chemistry). The convective time scale is obtained from the choice of Courant (CFL) number we choose to run the simulation at. The chemistry time scale can be defined in two ways:

- an intrinsic time scale, obtained from the maximum rate of change of any chemical specie. For example, the chemical time scale will be the time required for a specie molar fraction to change by more than 10%, provided it is not close to zero initially.

- a coupling time scale, defined as the time required for the chemistry to modify any flow variable by (say) more than 5%. Since the chemistry affects mostly the temperature, this is the variable used in that case.

The second time scale provides a global limitation on the time step to be used: if the chemical effects dramatically change the formation energy of the mixture during the time step, and if this δe° is large compared to the internal energy, the numerical solution becomes rapidly unstable. This has a profound effect on the choice of numerical methods to be used, for example, in combustion. In the remainder of this

paper, we always limit the global time step such that the estimated relative change in temperature, induced by chemical reactions, is smaller or equal to 5%. We allow the use of large (CFL> 1) global time steps provided this condition is satisfied. Let us emphasize that this restriction still allows us to consider stiff problems, where the stiffness is defined by using the intrinsic chemical time scale. Chemical equilibrium can be reached rapidly, without significantly modifying the temperature; the flow conditions simply must be such that the equilibrium values are not very different from the initial values, or that the energies of formation are relatively small compared to the internal energy.

The results presented in this section are obtained using the following methods[t]:

1 FC/Block tridiagonal
2 OS/Block tridiagonal
3 EC/Block tridiagonal
4 EC/Scalar tridiagonal
5 EC/N_s − Split tridiagonal

The chemistry is always computed with a single iteration.

Let us look first at case 1, for $P_\infty = 10^{-5}$ atm. The profiles of temperature are shown (left scale on the plots) as well as the mole fractions of N and O atoms (right scale on the plots). Figure 2 shows these profiles for a calculation at CFL=2 and 4. Figure 2-a shows only the results for the FC/Block, EC/Scalar and EC/N_s-Split methods: the remaining cases of EC/Block and OS/Block would show profiles exactly identical to the FC/Block method. The agreement between the other methods is also quite good. This is also true for the CFL=4 case (Figure 2-b, bottom), although to a lesser extent: in this figure, the curves for the EC/Block case are omitted, since they are identical to the FC/Block results. It appears therefore for this case that the EC and OS methods are as accurate as the FC method. The N_s-Split method shows slight errors in species concentrations near the shock, in the region of highest concentration gradients, which worsen as the CFL number grows. The Scalar method has an overshoot at CFL=2, and cannot be operated at larger CFL numbers. All methods fail for larger CFL values.

Figure 3 shows the same profiles (obtained when the shock reaches the same position) for a slightly

[t]The notation used has been mentioned in the previous section, and is summarized in Table 1.

stiffer problem (case 2). Again, we had perfect agreement between ∴ OS/Block, EC/Block and FC/Block methods, and the EC/Block profiles were omitted for clarity. The overshoots in mole fraction near the shock, for the N_s-Split method, are worse for this stiffer case. Again, the Scalar method works reasonably well for CFL=2, but fails for larger values. These calculations were done using the standard *minmod* limiter in the convective fluxes, as described by Harten [3], with an entropy fix $\epsilon \simeq 0.1$. When using a more compressive flux-limiter, such as the 'Superbee' limiter, the calculation could proceed as well, although with very slight oscillations. Reducing the entropy parameter to $\epsilon \simeq 0.01$ would lead to more severe oscillations. Therefore the rapid elimination of the transients can be best achieved by ensuring that sufficient numerical diffusion is present. The final flow solution therefore would need to be further sharpened, when the steady state is nearly achieved.

Figure 4 shows the stiffest case for CFL=2. All methods failed for larger CFL values. It is remarkable that the FC/Block method failed for this case, while the EC/Block method gives the best results. The OS/Block method (which uses the fractional step approach) gives very similar results, and can be considered as accurate. Surprisingly, the EC/Scalar method is stable, although the species profiles show an unphysical kink in the relaxation region. In order to better determine which method is more accurate, we computed the same case on a larger grid (2000 points) using the FC/Block method. By increasing the grid density, we achieved a ten-fold reduction of the stiffness of the problem. The FC/Block was then run successfully, and gave a very short relaxation zone (see Figure 4b). We also attempted to better reproduce this relaxation on the coarse (200 points) grid by either 1) sub-cycling the chemistry or 2) reducing the time step. Figure 4b shows the comparison, for example between the FC/Block results computed on the high-density grid, with the EC/Scalar with 10 sub-iterations of the chemistry and an explicit calculation (CFL=0.2). The two latter cases are not very different from the results of Figure 4a, i.e., neither the sub-iterations nor the time step reduction greatly improve the solution. It seems that all methods tend to overestimate the length of the chemical relaxation zone in stiff cases, although the final equilibrium result is accurate. We must conclude also that the EC or OS methods are more stable than the FC method in stiff cases: we also observed this feature on other stiff cases. The mixing of non-diagonal elements in the global Jacobians, between convective and chemical terms, may make the

matrices more prone to ill-conditionality, and reduce the stability.

It seems therefore that only relatively small values of the CFL number can be effectively used for t.. transients, and therefore only the Scalar me'hod, so far, is efficient. However, it is not accurate enough when the chemistry is very stiff. It also appears that the N_s-Split method, in its current form, suffers from unphysical numerical species diffusion in the region of strong gradients, and for large time steps (this error is inexistent in the explicit regime). Since there are other cases where implicit methods can have a significant impact, we will look also at expanding flows in the next section.

IV. One-Dimensional Nozzle

We will model a converging/diverging nozzle, with 150 grid points in the axial direction: the calculations were performed using two-dimensional codes, and the grid used 10 points in the radial direction. Since we were interested only into axial profiles, this was considered sufficient for our purposes. Notice that now there will be an additional error due to the dimensional split in the implicit methods. The left boundary condition and initial state considered a gas at a pressure of 4.205 atm and 1000°K. However, the gas composition was arbitrarily set to non equilibrium values by increasing the amount of dissociation: this had the effect of stiffening the chemistry in the subsonic region of the nozzle. The calculations were always started impulsively, and run at CFL< 1 (explicit) until the shock exits the nozzle, before the implicit models were tried. We used this case to evaluate the effect of sub-iterations and sub-coupling in the chemistry.

Figure 5 shows the comparison of residual history for the 4 implicit methods used, i.e. FC/Block, EC/Block, EC/Scalar and EC/N_s-Split, and without any sub-iterations or sub-coupling. The residual of the subsonic zone (solid line) and supersonic zone (dotted line) have been shown separately. A first break point in the curves shows the end of the explicit pre-calculation, used for elimination of the shock from the nozzle. The implicit scheme is then used, with a constant CFL=1.5, until a time of 5 milliseconds. At that point, the calculation is pursued further for the supersonic region only, the subsonic region remaining frozen. The residual shown is for the total energy, and is averaged over the entire volume of the region considered.

Figure 5-a shows the results for the FC/Block method, Figure 5-b for the EC/Block method. Both show good convergence properties, with a slight improvement for the EC/Block method. The N_s-Split method (Figure 5-c) has even better convergence properties, but the Scalar method (Figure 5-d) shows a non-vanishing residual for the subsonic region. All methods converge rapidly in the supersonic region when computed separately, indicating that most of the problems (if any) are located in the subsonic region.

The solutions obtained at 5 milliseconds are plotted in Figure 6, for the atomic oxygen mole fraction. The solution for the scalar method is slightly in error in the subsonic region, but quickly recovers during the expansion and leads to the correct final value. The N_s-Split method has the opposite behavior, i.e. has an error increasing with the distance along the nozzle: it seems that the species convection suffers from some unphysical diffusion of species, also noticed in the results of the previous section: there is a phase error between each species convection, which is irreversible. By contrast, the Scalar method correctly propagates the species, but does not accurately couple the convection with the momentum and energy equations. This may lead to fluctuations in pressure or temperature, which quickly disappear when the flow becomes near supersonic.

The use of sub-iterations in the chemistry did not change the results for this case. Increasing the stagnation pressure and the stiffness slowly lead to noticeable effects. The most dramatic differences between the cases of sub-iterated and non-iterated chemistry were observed for very stiff systems, at the limit of stability. In order to demonstrate the effect of sub-iterations, or sub-cycling of the chemistry, we consider a high pressure (400 atmospheres) case, with an initial temperature of 6000 °K, and a highly non-equilibrium initial composition (non-dissociated air). A constant time step of 5×10^{-8} seconds was assumed. Figure 7 shows the results of the chemistry integration (no fluid dynamics) for both non-iterated and sub-iterated (20 cycles) cases. It is clear that a single step of the chemical integration, with $\Delta t = 5 \times 10^{-8}$ sec, leads to very large changes in species concentrations and temperature. This will significantly affect the remainder of the history of the chemical integration. If the time step is not too large, the correct equilibrium values may be obtained in the final steady state: if the time step is large enough, unphysical values (i.e. negative concentrations) may be obtained during the first step,

and the correct solution cannot be recovered. By using a smaller time step (10^{-8} sec), both methods give essentially the same history, and the same final values, which agree with the values obtained in Figure 7 for the sub-iterated case. It is clear then that in some severe cases, the sub-iteration of the chemistry can yield a higher stability and a higher accuracy: these cases may be found for example in high-pressure shocks, detonations, or strong ionizing shocks, when the grid used is coarse.

The method of sub-coupling was also tested on some other stiff cases. It was found that the stability was slightly reduced when the sub-coupling was incorporated. When the chemistry is sub-iterated and sub-coupled, the convection of species during the sub-step δt is estimated and included in the variation. While this process accounts for the effect of the convection on the chemistry, it fails to account for the reverse process, and it fails to account for the influence of other convective terms, specifically the pressure waves. The coupling of the chemistry is not 'in phase' with all the convective equations. In subsonic regions and behind shock waves, the pressure waves are a dominant process, and a significant error is made. We therefore recommend that no sub-coupling (SIC) be used if the chemistry is sub-iterated.

V: Two-Dimensional Shock Layer

The final test will be done for a 2-dimensional, axi-symmetric flow around a blunt body. This is a typical flow configuration of interest. The flow is modeled with a 144×80 grid, the free stream Mach number is $M_\infty = 25$, the free stream temperature and pressure are $T_\infty = 241.75°K$ and $P_\infty = 1.65\ 10^{-4}$ atm; the free stream is air, modeled using 11 species $N, O, N_2, O_2, NO, N^+, O^+, N_2^+, O_2^+, NO^+, e^-$ and a 15 reaction set from Dunn & Kang [5]. The blunt body shape is taken from the Apollo spacecraft.

The calculations were proceeded with the FC/Block method and the OS/Scalar method. Since the chemical charges were quite important in the shock layer, our restriction in time step due to the temperature changes (relative change < 5%, see section III) prevented us to compute the flow implicitly. Any attempt to increase the time step, and therefore to allow a larger change in temperature due to chemical effects led very quickly to flow instabilities. The comparison presented below is therefore between a FC/Block implicit method run at small time steps,

and an Operator-Split method where the fluid dynamics are computed explicitely. The pressure behind the shock is close to 0.5 atmospheres, with a temperature between 8,000 and 12,000 °K, and the chemistry is rather stiff, especially due to the reactions involving electrons. Figure 8 shows the comparison between the two methods along the stagnation line, and the agreement is very satisfactory.

There is a lack of resolution of the shock front, and we proceeded to improve the results by adapting the grid in the neighborhood of the shock. Several adaptions were performed, first on the temperature gradients, then on the chemical gradients (N_2). After each adaption, the flow was computed further until convergence. The adaption procedure used the SAGE code [6] developed at Ames, and affected grid points in a direction normal to the blunt surface only. Figure 9 shows the comparison between the original, non-adapted solution and the results from the final adaption. Since the results from the FC/Block and OS/Scalar methods were found to be agreement, and since the latter method is considerably more efficient, only the OS/Scalar method was used for the adapted cases. We see in Figure 9 that the peak temperature has changed significantly (15 %), and so has the shock location. Although the flow variables relax to the same values in the midst of the shock layer, the unresolved relaxation zone may still affect some important engineering variables, such as the radiative heating at the wall. The radiative emission power behind the shock will depend strongly on the temperature and species densities, both varying rapidly in that region, and being very sensitive to the grid resolution. Therefore, a radiation code was used to compute the intensity along the line-of-sight in the stagnation region, and the heat flux at the wall: this computation was performed after the flow steady state was obtained, i.e. the flow and radiation were not coupled. After each adaption, the change in radiative heat flux was computed and compared: the results are shown in Table 2, for both the optically thin case and the optically thick case. In the former case, the relative changes are quite large, and the values converge slowly. In the thick case, the absorption by the core of the shock layer tends to damp the perturbations: for that case, we see that the heat flux converges more rapidly towards a final value. Since the relative change is small (-1.8%) after the 3rd adaption, we considered that the resolution was now sufficient. The comparison in radiative spectrum at the wall between the unadapted and final solution is shown in Figure 10. Most of the changes occur in the UV region.

8

It is important to remark that the computed radiation did not include the continuous spectrum, and therefore the variations in radiative heating at the wall may be under-estimated. Additionally, the density is sufficiently large in this example that equilibrium radiation can be assumed: this considerably reduces the uncertainty in the computation of the radiative flux. For lower density and higher velocity cases, one must include thermal non-equilibrium effects. The relaxation zone becomes then even more important to resolve accurately.

It appears from this example that in practice it will be very difficult to compute a flow using an implicit method with a large CFL number, and that hydrodynamics-chemistry coupling effects will sometimes limit the time step to CFL values below 1. Additionally, we may be required in practice to transform the grid, according to the solution obtained, in order to reach the desired accuracy: these adaptions need to be performed several times. It would seem therefore that a more efficient approach would combine the flow computation with the grid refinement. Indeed, there is a technique that can potentially lead to more efficient computations: using unstructured grids, the computational cells can be subdivided at will to give better accuracy in the regions that need it. Similarly, the subdivided cells can be regrouped in regions of low gradients, in order to keep the total number of cells within reasonable limits. Such a technique would use a small number of cells to start with, and progressively refine them: most of the transients would then be computed using a small number of cells, leading to a more efficient procedure.

VI: Conclusions and Recommendations

We have not used here all the possible variations on the implicit schemes, neither have we exhausted the methods of coupling the chemistry and the fluid dynamics. We have however used techniques which are commonly used, and, we hope, demonstrated the trends for practical problems. We can draw several conclusions from this study:

1. It is clear that on many problems of interest, the calculations cannot proceed with very large CFL numbers during the approach to steady state. Inevitably, for large numbers of species, the Block Tridiagonal methods cease to be efficient in that regime. Only Scalar Tridiagonal methods, or even explicit methods remain efficient.

2. It is clear that the Operator-Splitting approach, including the Explicit-Coupling between chemistry and hydrodynamics, is at least as accurate as the Fully Coupled, and apparently more stable for very stiff problems. Sub-iterations of the chemistry can further improve the accuracy and stability in the most severe cases of stiffness

3. The N_s-Split method, at least in its present formulation, is too inaccurate for large time steps or strong concentration gradients. This disapointing result is not completely understood at the moment. It does not affect our conclusions, since the method is less performant than the Scalar method. This results should however be investigated further, since it may have implications on other systems, such as a two- or three-fluid plasma, where the implicit treatment of the electron component gas dynamics is mandatory.

4. Calculations of shock layers on fixed grids may not be sufficiently accurate if radiative phenomena or thermal non-equilibrium effects must be considered. In the example shown, several iterations at grid adaption were necessary. Other calculations on similar problems were also performed, that supported this conclusion. It appears then that dynamical grid adapting should be performed during the course of the calculation, for higher efficiency.

Dynamic grid refinement could lead to even higher efficiencies if both the distribution and the overall number of grid points are allowed to vary. This can be done on structured as well as unstructured grids. The construction of implicit schemes on unstructured grids would be quite complex. However, we have concluded that this may not be a restriction for many cases. An explicit algorithm will therefore be sufficient, and the technique is reduced to a sophisticated book-keeping problem. In addition, the use of explicit, Operator-Split techniques allows us to take advantage of massively parallel (or mixed) computer architectures. This method will be investigated in the future.

We have not mentioned another technique applicable for Operator-Split methods, when the chemistry is very stiff. The chemistry (or other internal process) can be rescaled, or 'slowed-down' artificially: this may have the effect of increasing the relaxation distances. However, we have made preliminary calculations that seem to indicate that in the very severe cases of stiffness, the changes are not perceptible. In addition, this procedure can be used

during the elimination of the transients, then the rescaling is progressively eliminated until a steady state with the proper time scale is obtained. If the rescaling is not eliminated, a false steady solution is obtained. The influence of the numerical procedure on the steady solution is also a serious question, discussed recently by Lafon & Yee [7]. They show that for flows coupled with non-linear source terms, the steady state reached may depend on the path used to reach it. It is clear therefore that the errors induced by the numerical procedures can never be under-estimated, and that all users of CFD should proceed with extreme caution.

VII. References

[1] A. Harten, *J. Comp. Phys.*, vol 49 (1983), pp. 357-393.

[2] G. Sod, *Numerical Methods in Fluid Dynamics*, Cambridge University Press, 1985.

[3] E. Oran & J. Boris, *Numerical Simulation of Reactive Flow*, page 130, Elsevier Publ., 1987.

[4] N. Yanenko, *The Method of Fractional Steps*, Springer-Verlag, 1971.

[5] M. Dunn & S-W. Kang, 'Theoretical and Experimental Studies of Reentry Plasmas', NASA-CR-2232.

[6] C. Davies & E. Venkatapathy, 'Application of a Solution Adaptive Grid Scheme, SAGE, to Complex Three-Dimensional Flows', AIAA 10th CFD Conference, Honolulu, Hawaii 1991. AIAA paper 91-1594.

[7] A. Lafon & H. C. Yee, 'On the Numerical Treatment of Nonlinear Source Terms in Reaction-Convection Equations', AIAA paper 92-0419.

designation	Treatment of hydrodynamics	Chemistry/Convection coupling method
FC/Block	$N \times N$ Block Tridiagonal (section II-A)	Implicit (or Fully-) coupled
EC/Block	$N \times N$ Block Tridiagonal (section II-A)	Explicit (or Loosely-) coupled
OS/Block	$N \times N$ Block Tridiagonal (section II-A)	Operator-Split (or Fractional Step)
EC/Scalar	Scalar Tridiagonal (section II-B)	Explicit coupling
EC/N_s-Split	N_s-split method (section II-C)	Explicit coupling
EC-SI/Block	$N \times N$ Block Tridiagonal	Explicit with Sub-Iterations (or Sub-Cycling)
EC-SIC/Block	$N \times N$ Block Tridiagonal	Explicit. Sub-Iterations *and* Sub-Coupling

Table 1: Designation of numerical methods and coupling methods used in this study.

Grid Cycle	Relative Change in Surface Flux Optically Thin Gas [2000-8000 Å]	Relative Change in Surface Flux Optically Thick Gas [1740-1750 Å]
Non-adapted Grid - Adaption 1	-25.1 %	-11.0 %
Adaption 1 - Adaption 2	+27.1 %	+5.2 %
Adaption 2 - Adaption 3	-3.5 %	-1.8 %

Table 2: Axisymmetric blunt body calculations - results of grid adap·n study.
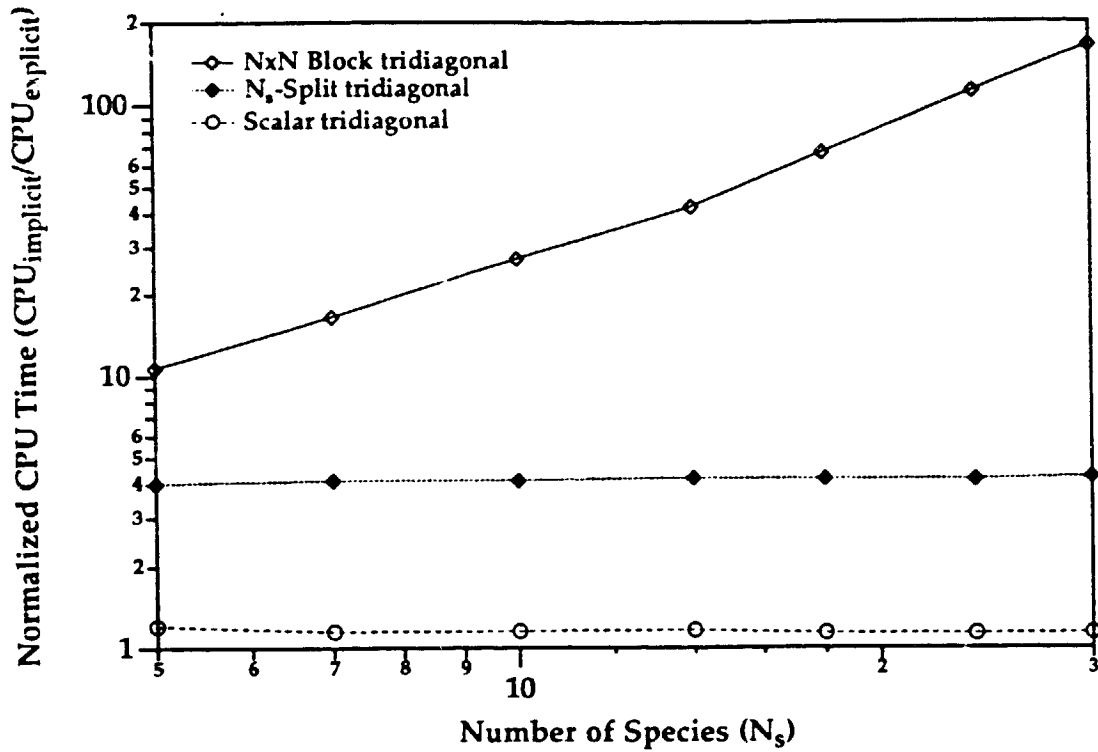
Figure 1-a. Normalized CPU requirement for Block, Scalar and N_s-Split methods (nonreacting). CPU is obtained as time per iteration per grid point, and normalized to CPU requirement for explicit method.
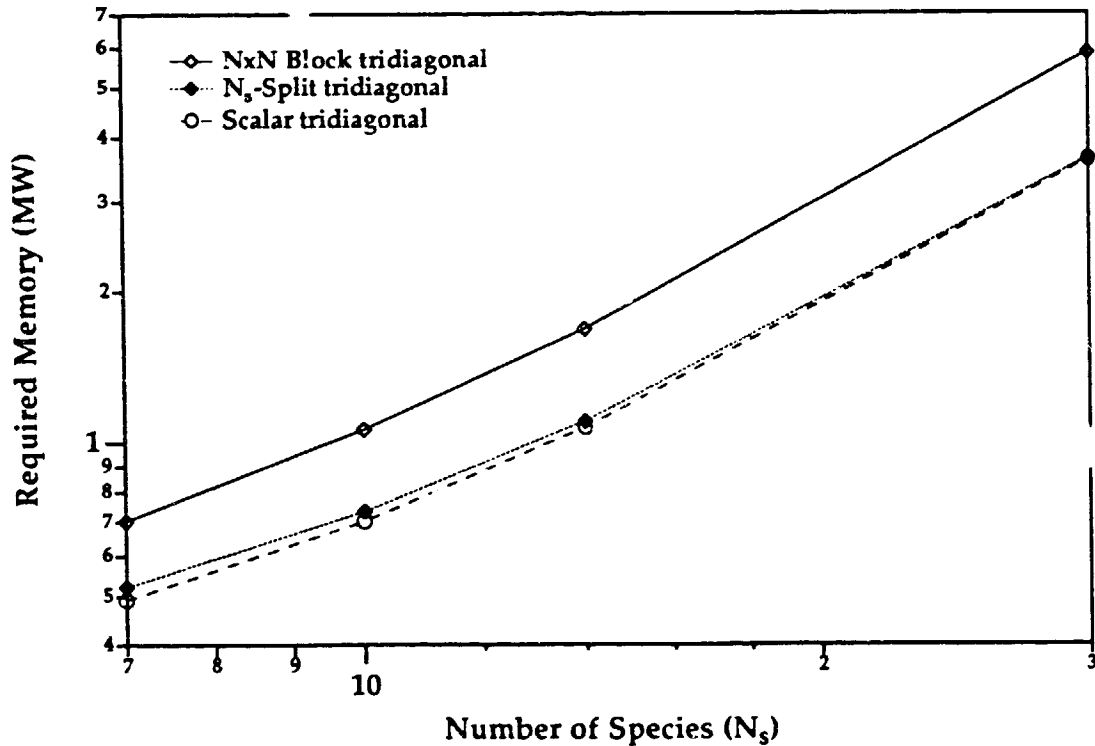
Figure 1-b. Memory requirement versus number of species for same methods

Figure 2-a. 1-D Shock (Case 1, $P_\infty = 10^{-5}$ atm). Results for CFL=2. Results for EC/Block and OS/Block methods were indistinguishable from FC/Block method and hence, are not shown.
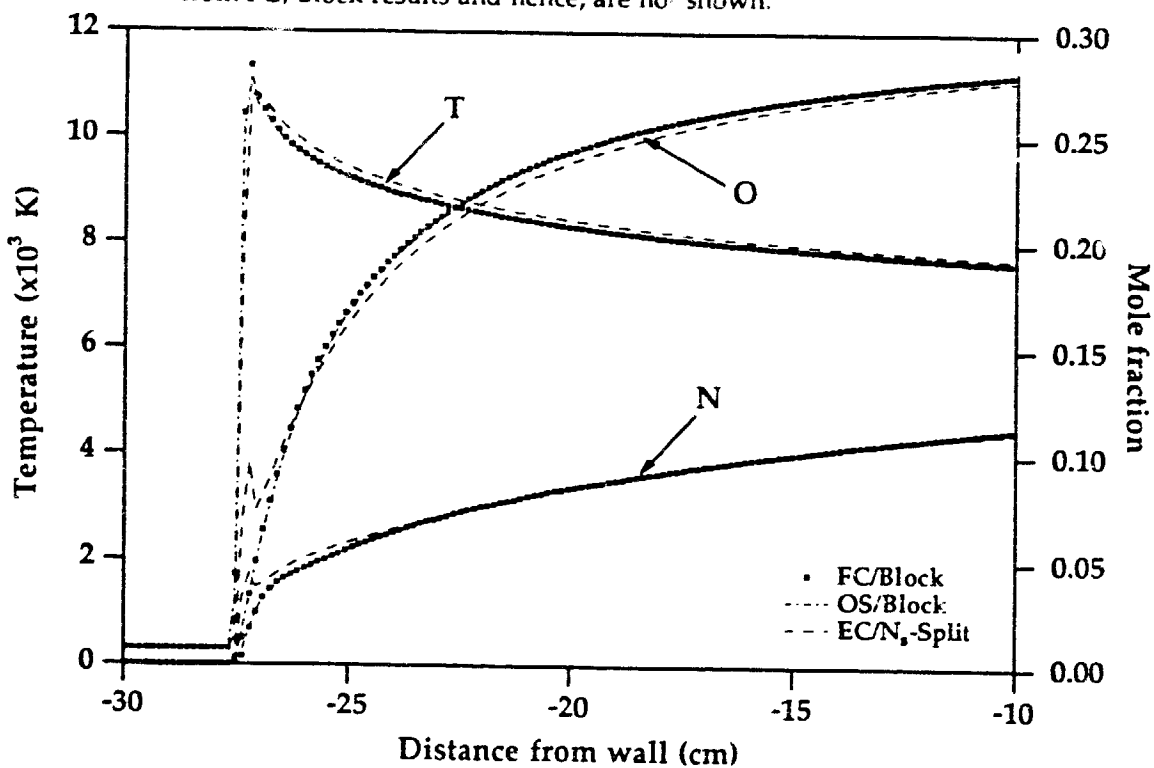

Figure 2-b. 1-D Shock (Case 1, $P_\infty = 10^{-5}$ atm.). Results for CFL=4. The EC/Scalar method failed for this CFL number.
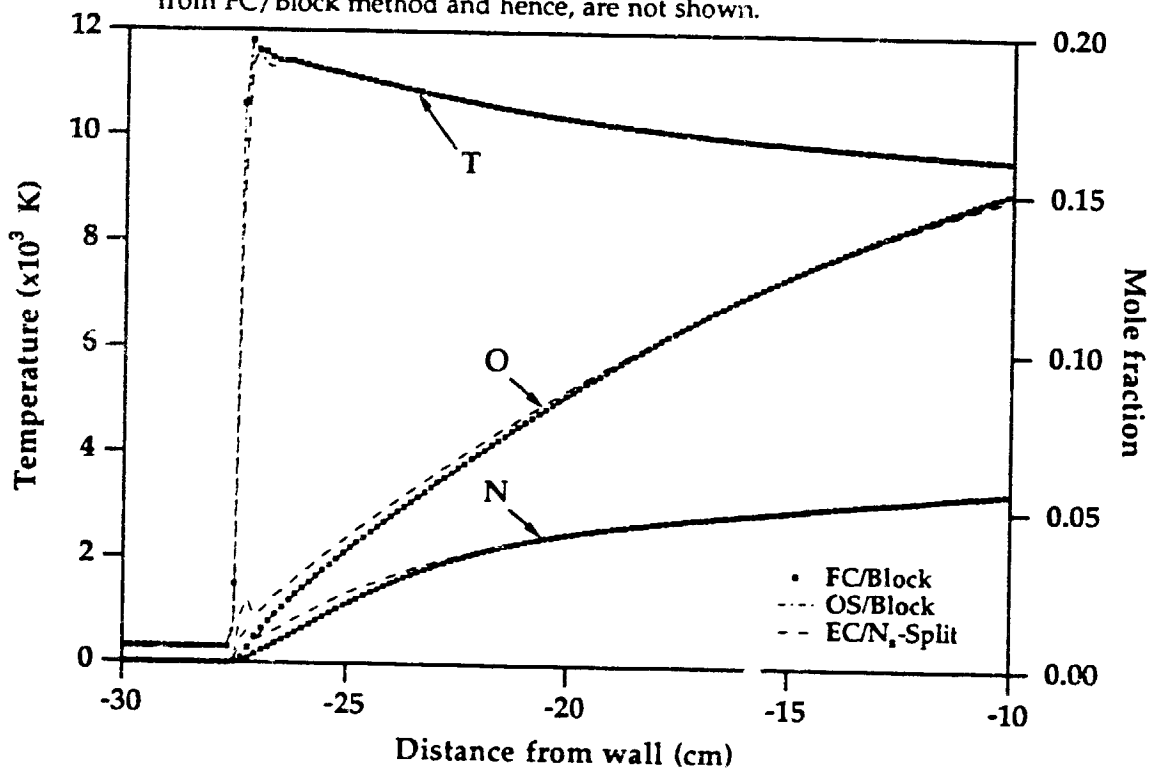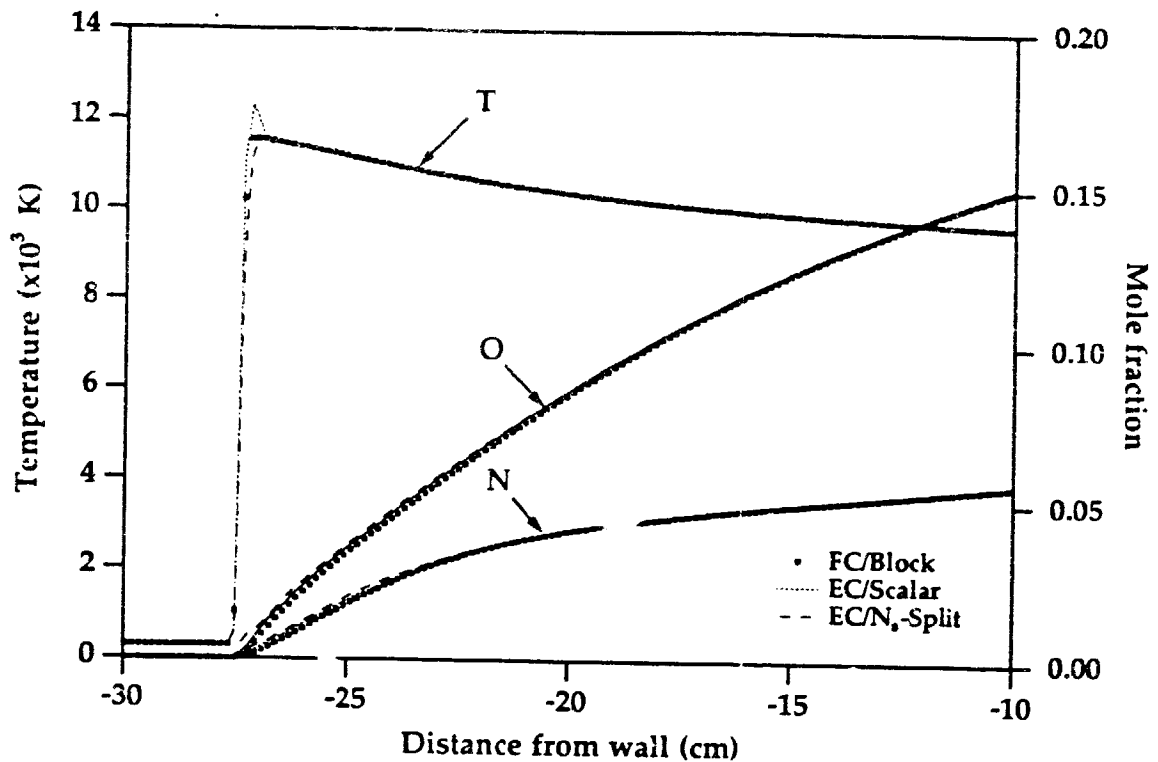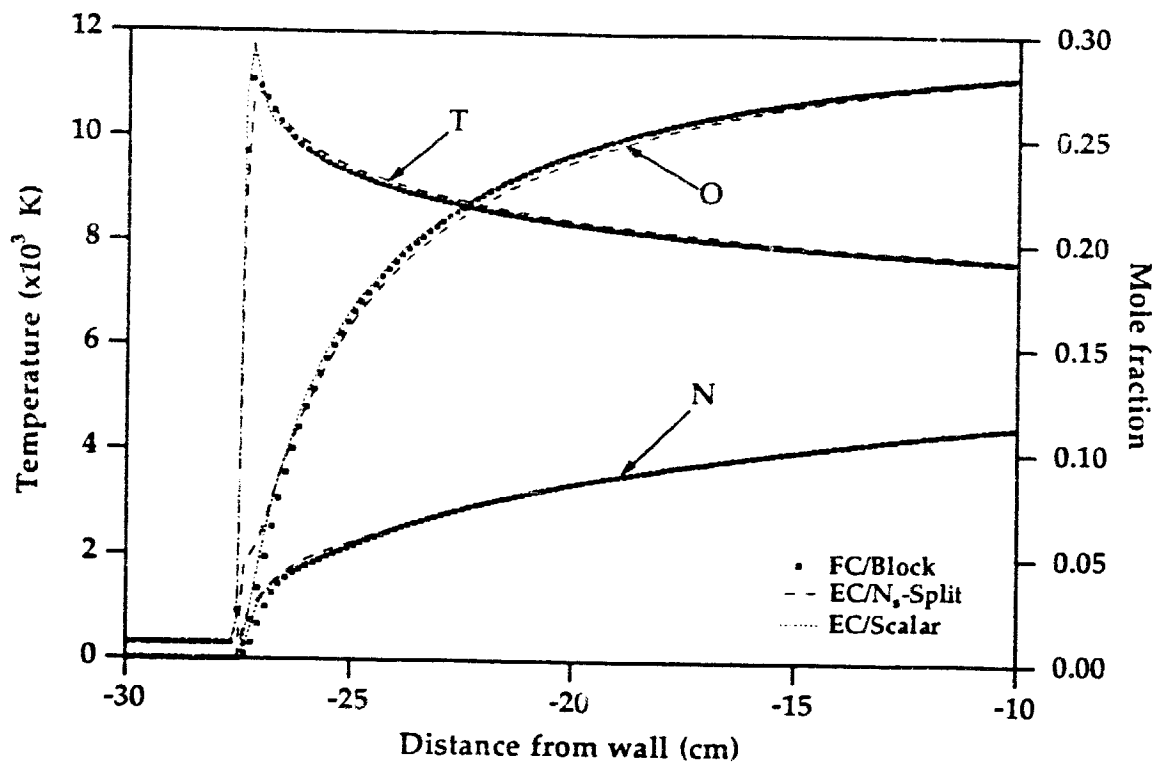
Figure 3-a. 1-D Shock (Case 2, $P_\infty=10^{-4}$ atm.). Results for CFL=2. Results of EC/Block and OS/Block methods are indistinguishable from FC/Block results and hence, are not shown.

Figure 3-b. 1-D Shock (Case 2, $P_\infty=10^{-4}$ atm.). Results for CFL=4. The EC/Scalar method failed for this case.

13
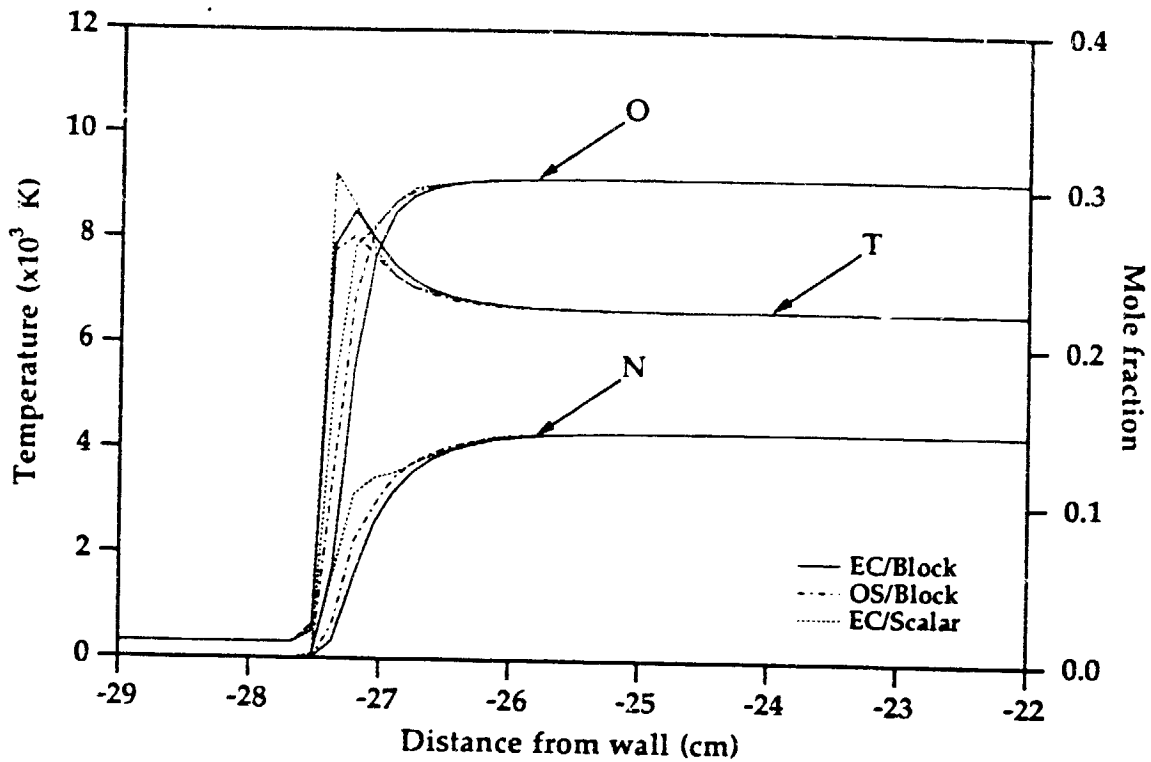
Figure 4-a. 1-D Shock (Case 3, $P_\infty=10^{-2}$ atm.). Results for CFL=2. The FC/Block method failed and the EC/N_s-Split method gave nonphysical, oscillatory solution.
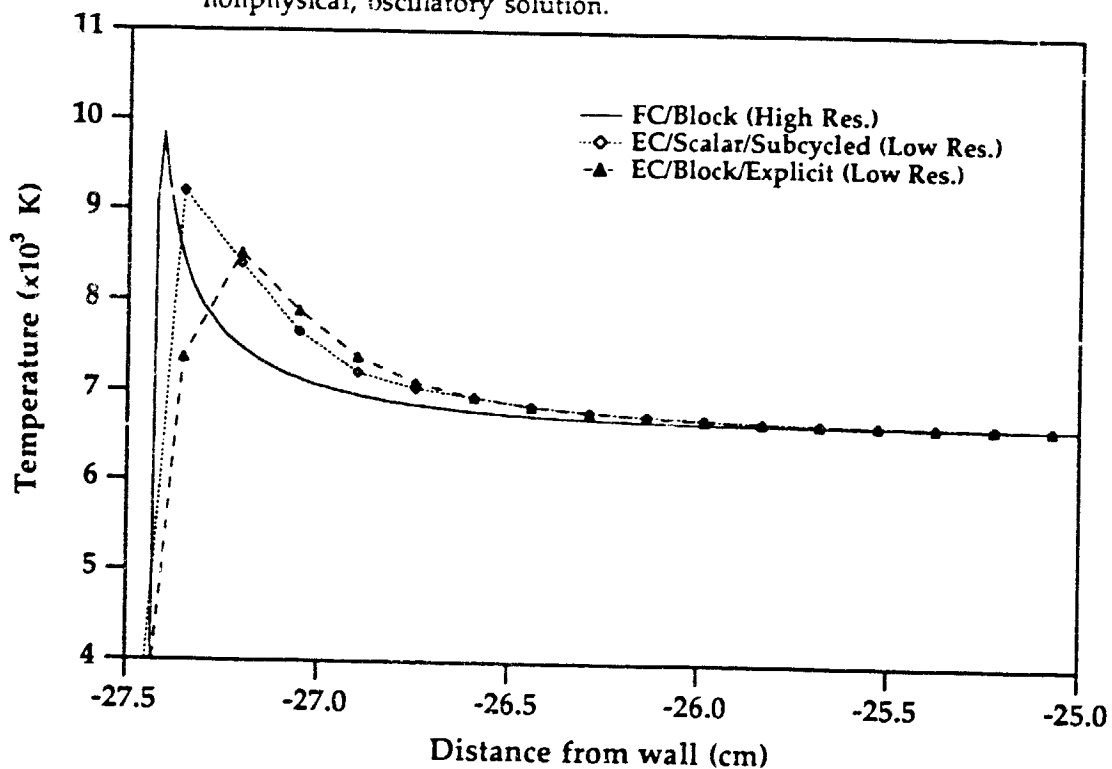
Figure 4-b. Details of Case 3. FC/Block solution is obtained for a higher density (x 10) grid. Other solutions shown are for the standard grid but with subcycled chemistry or smaller time steps (CFL=0.2)

14
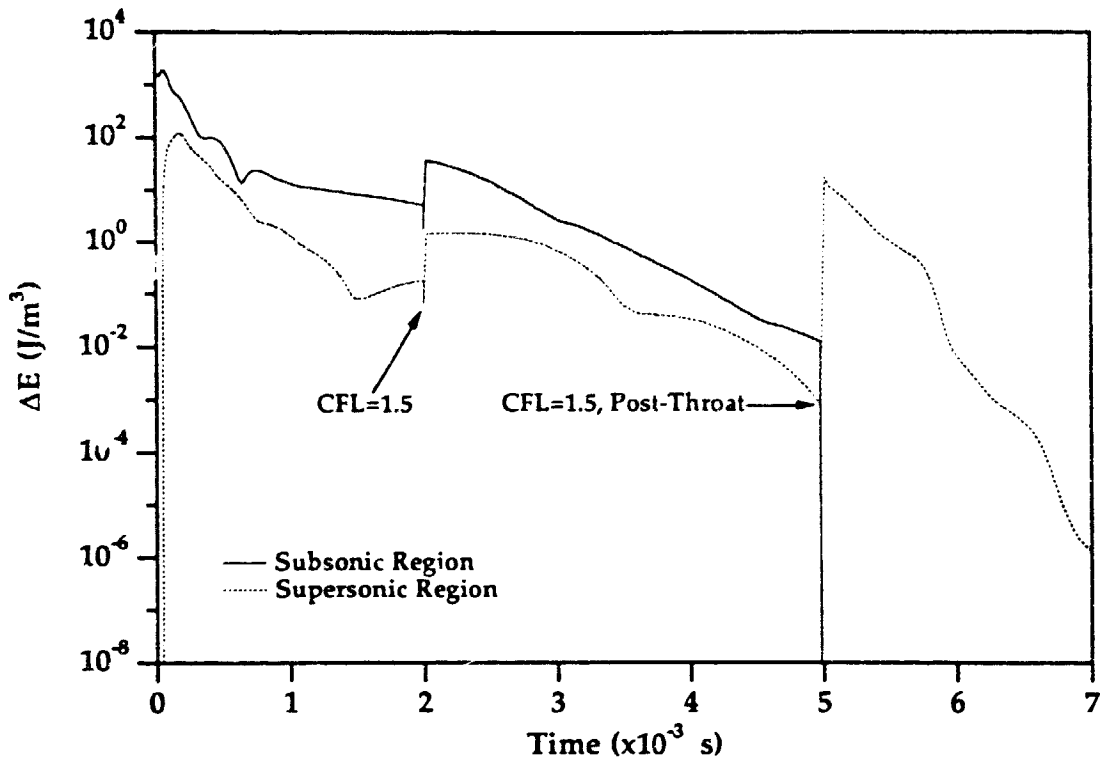
Figure 5-a. Quasi-1D Nozzle - energy residual history for the FC/Block method.
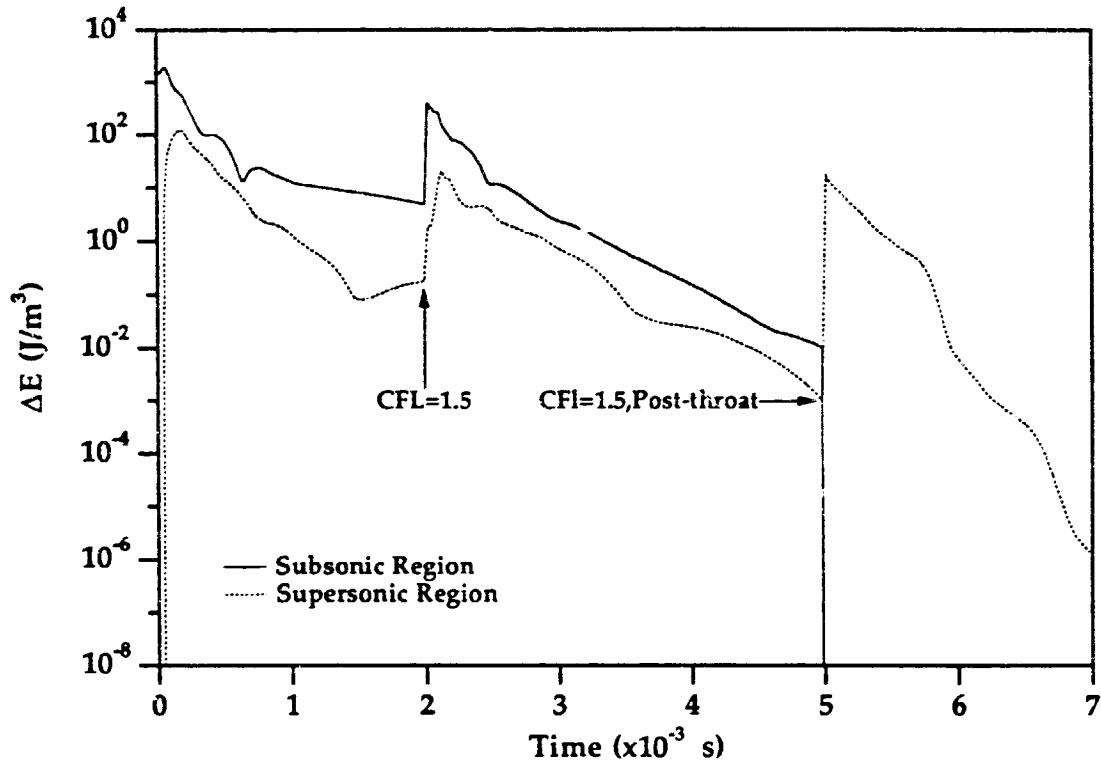
Figure 5-b. Quasi-1D Nozzle - energy residual history for the EC/Block method.

15
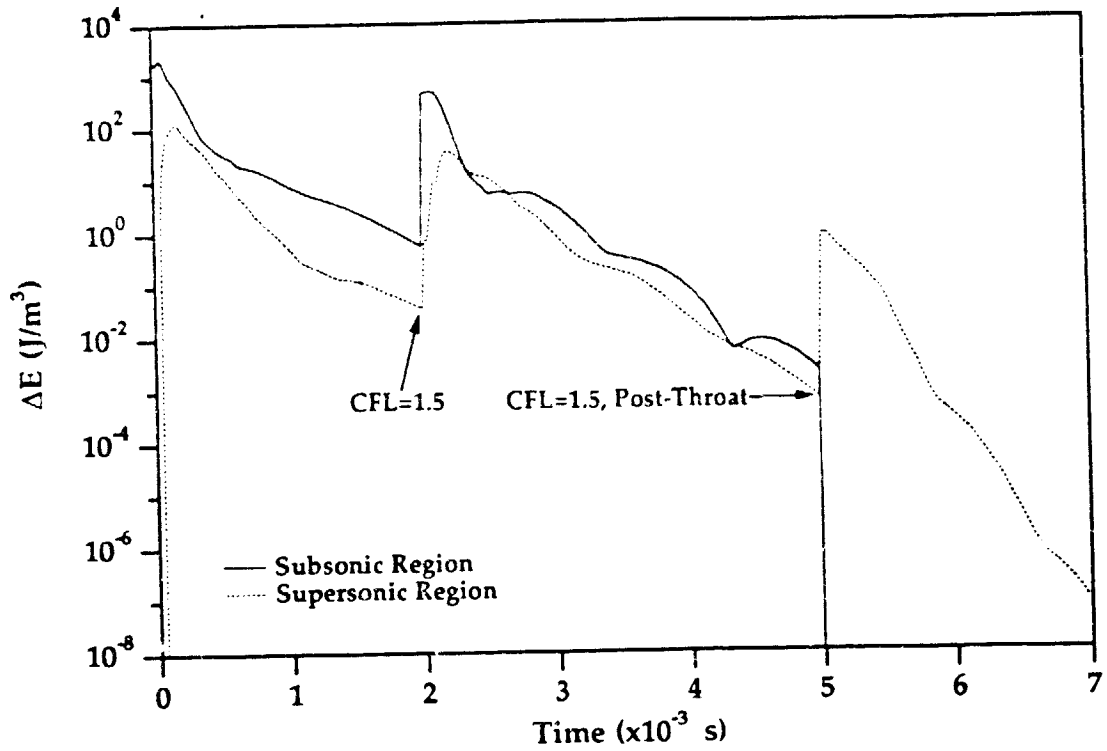
Figure 5-c. Quasi-1D Nozzle - energy residual history for EC/N_s-Split method.
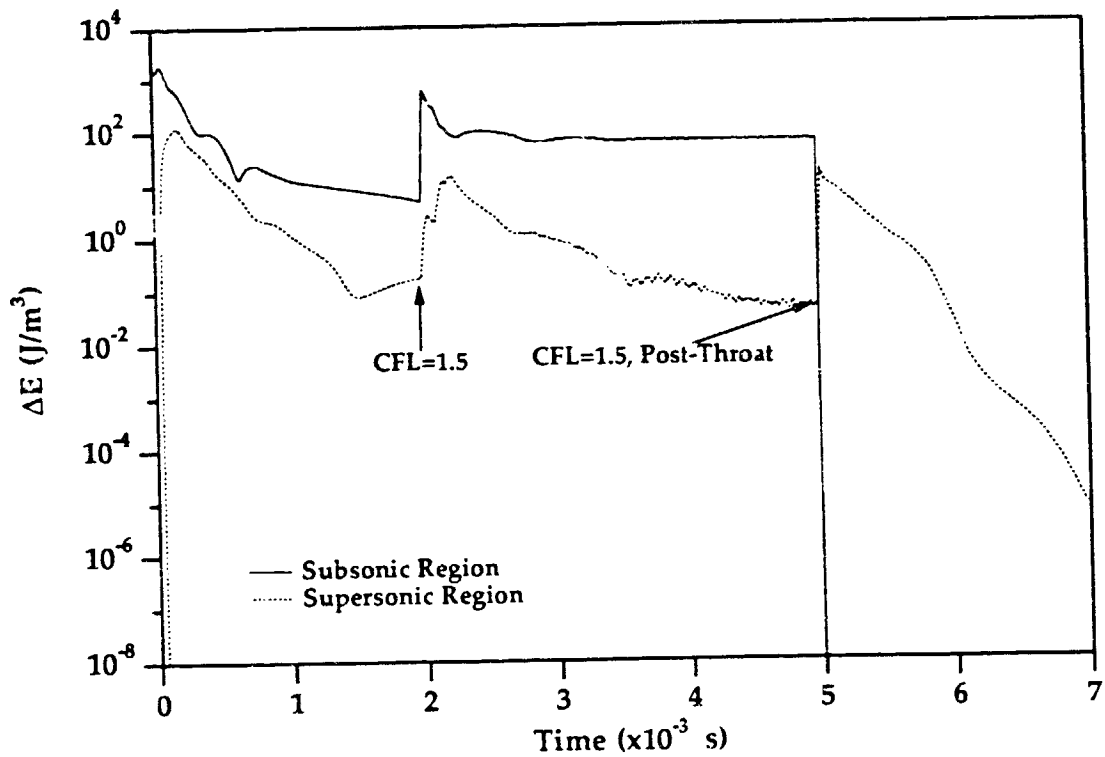
Figure 5-d. Quasi-1D Nozzle - energy residual history for EC/Scalar method.

16
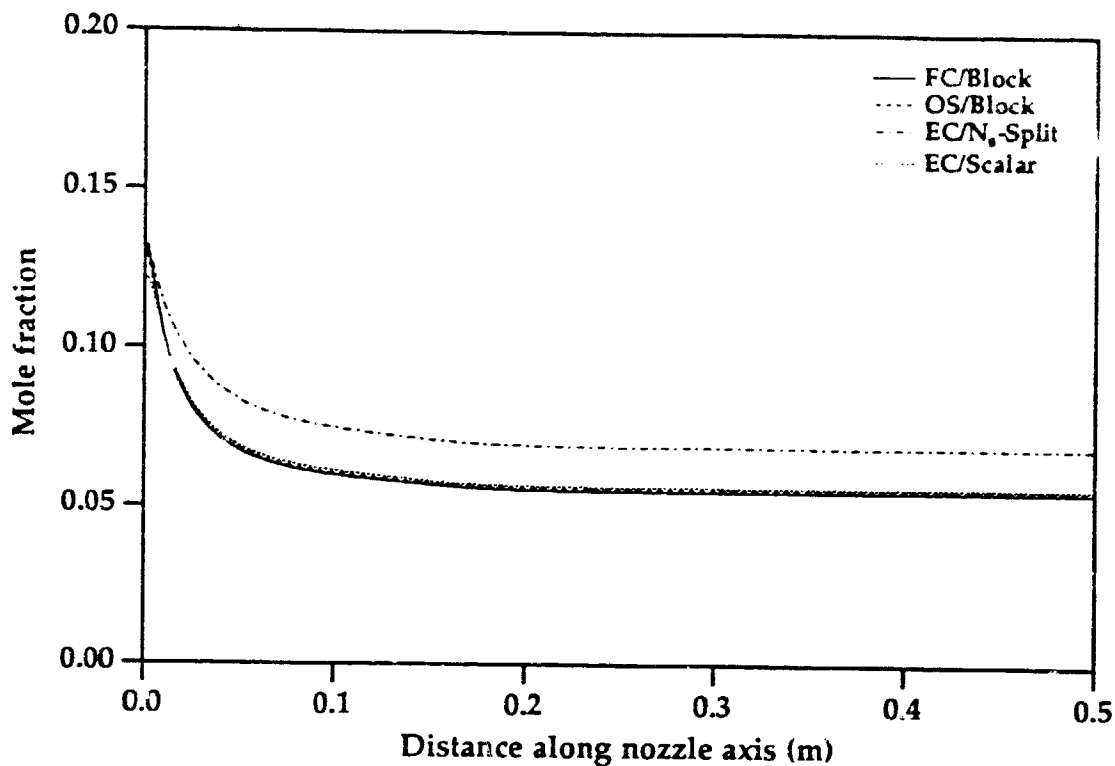
Figure 6. Quasi-1D Nozzle - steady state axial distribution of atomic oxygen.
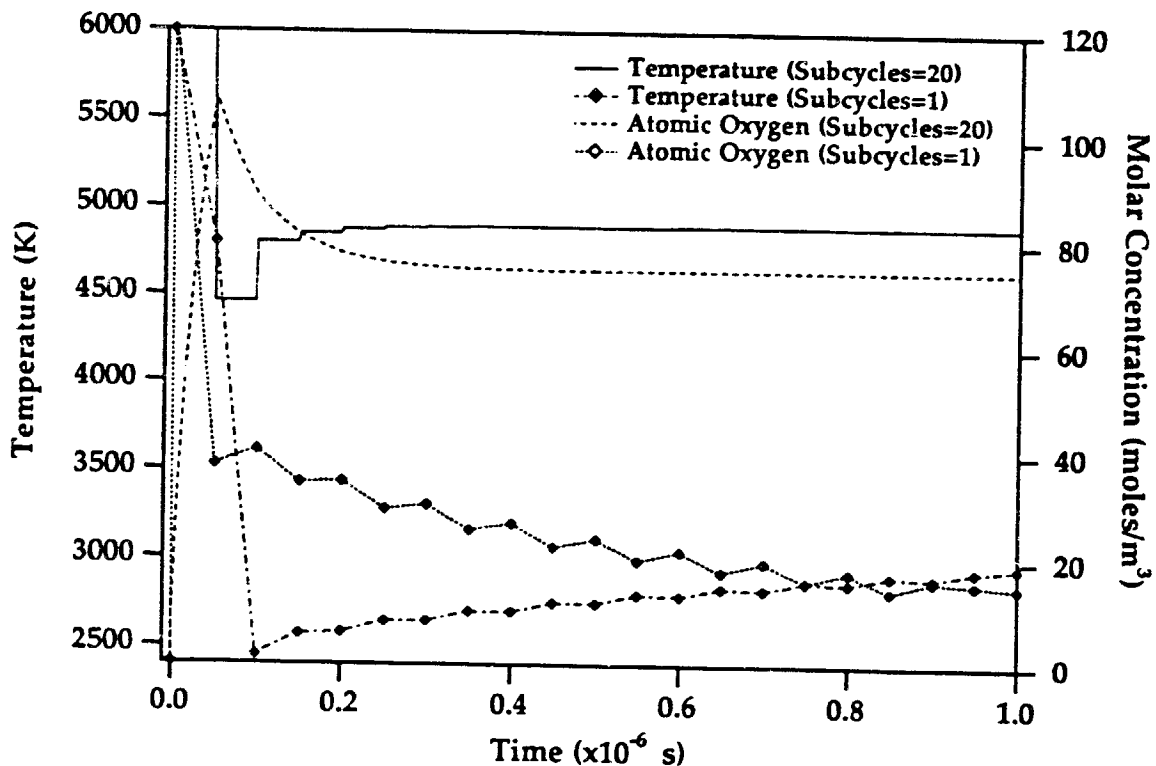
Figure 7. Quasi-1D Nozzle - Test of subiterated chemistry (EC/Block method). Initial state far from equilibrium and global time step (Δt) is 50 ns. Subcycled case (20 cycles) has an effective time step (δt) of 2.5 ns. The temperature is recomputed only at the end of the integration over the global time step 50 ns.

17
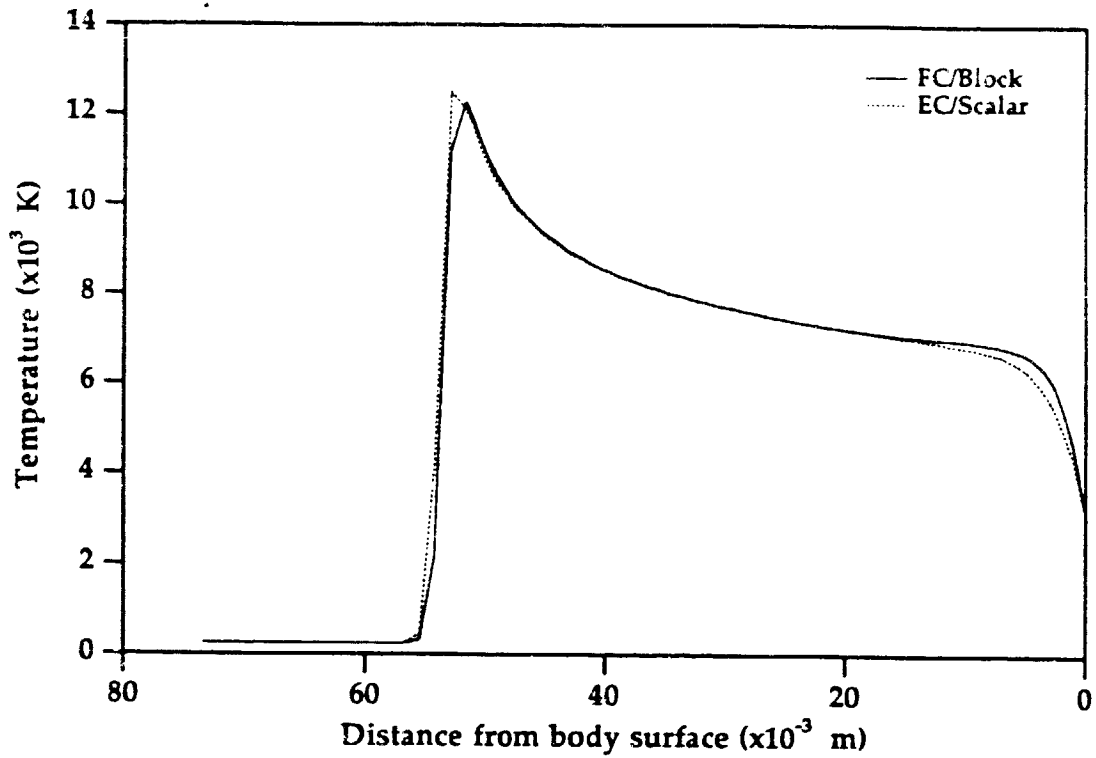
Figure 8-a. Axisymmetric Blunt Body - Temperature profile along the stagnation line (non-adapted grid)
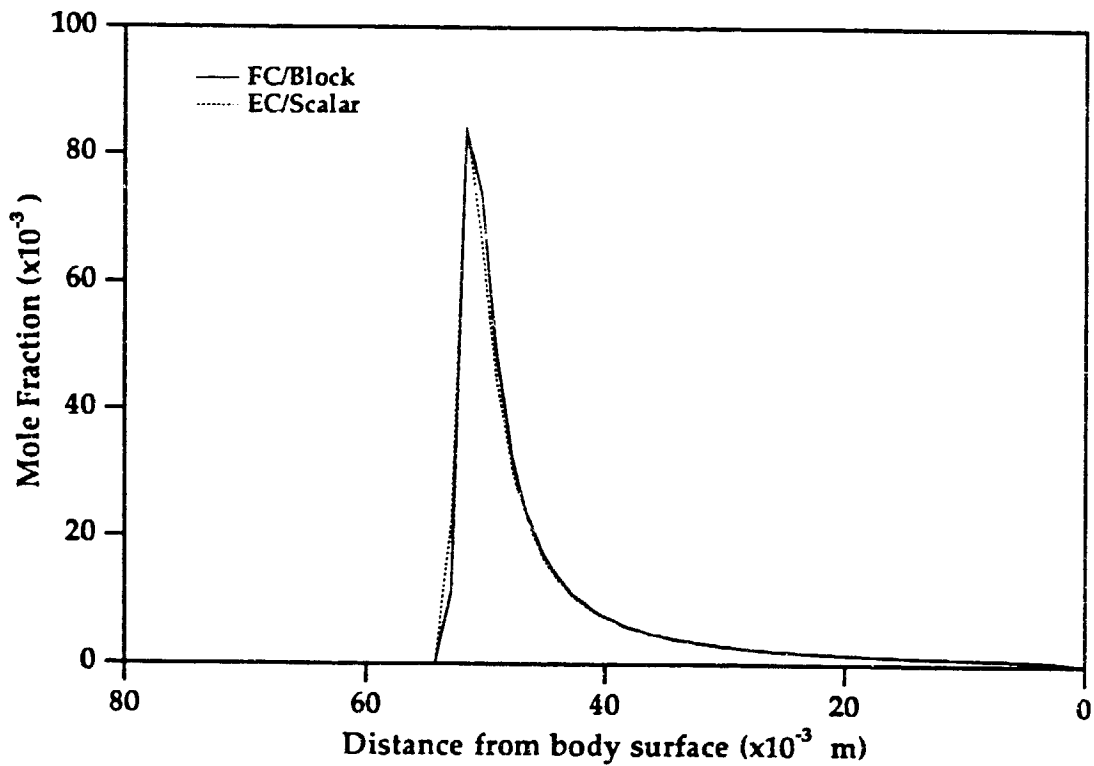
Figure 8-b. Axisymmetric Blunt Body - Electron mole fraction profile along the stagnation line (non-adapted grid).

18
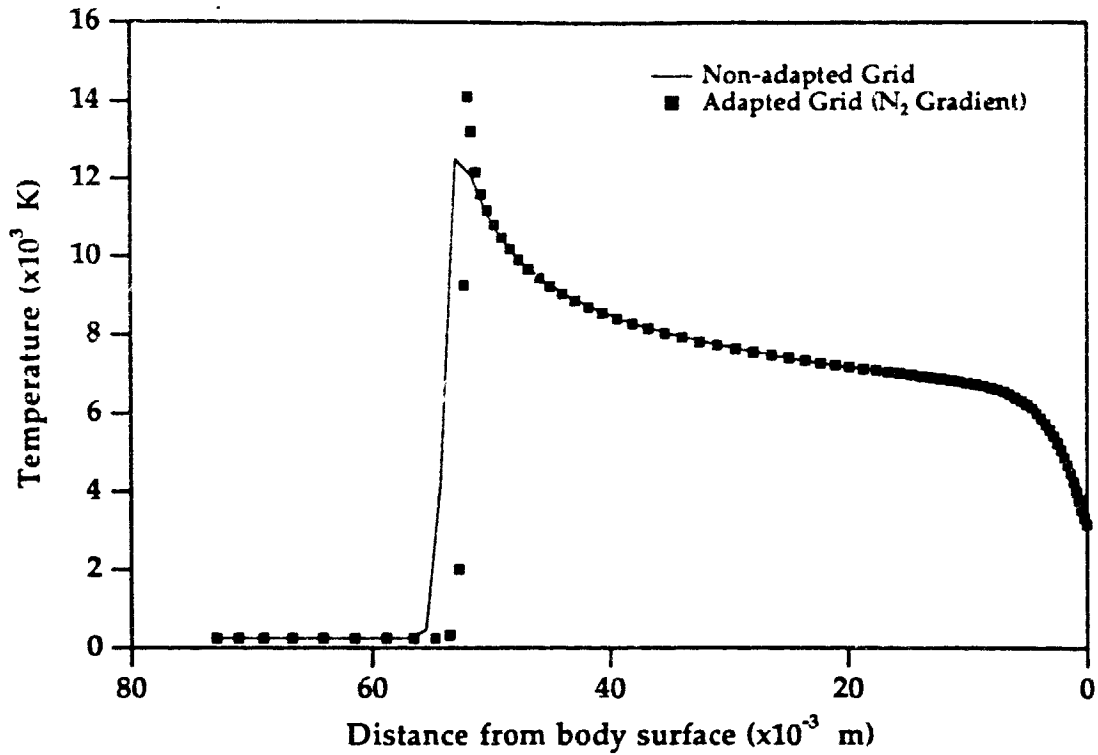
Figure 9-a. Axisymmetric Blunt Body - Temperature profile along the stagnation line for non-adapted and adapted (final pass) grid. Note the significant change in shock location and peak temperature.
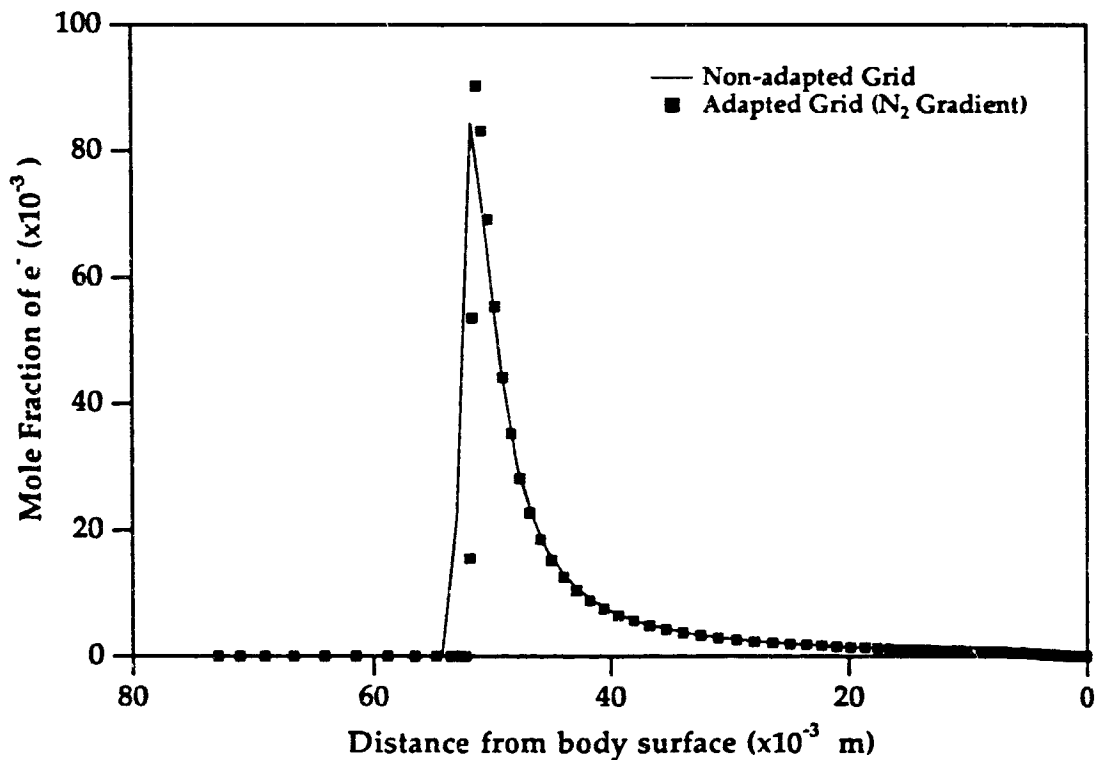
Figure 9-b. Axisymmetric Blunt Body - Electron mole fraction profile along stagnation line for non-adapted and adapted (final pass) grids.
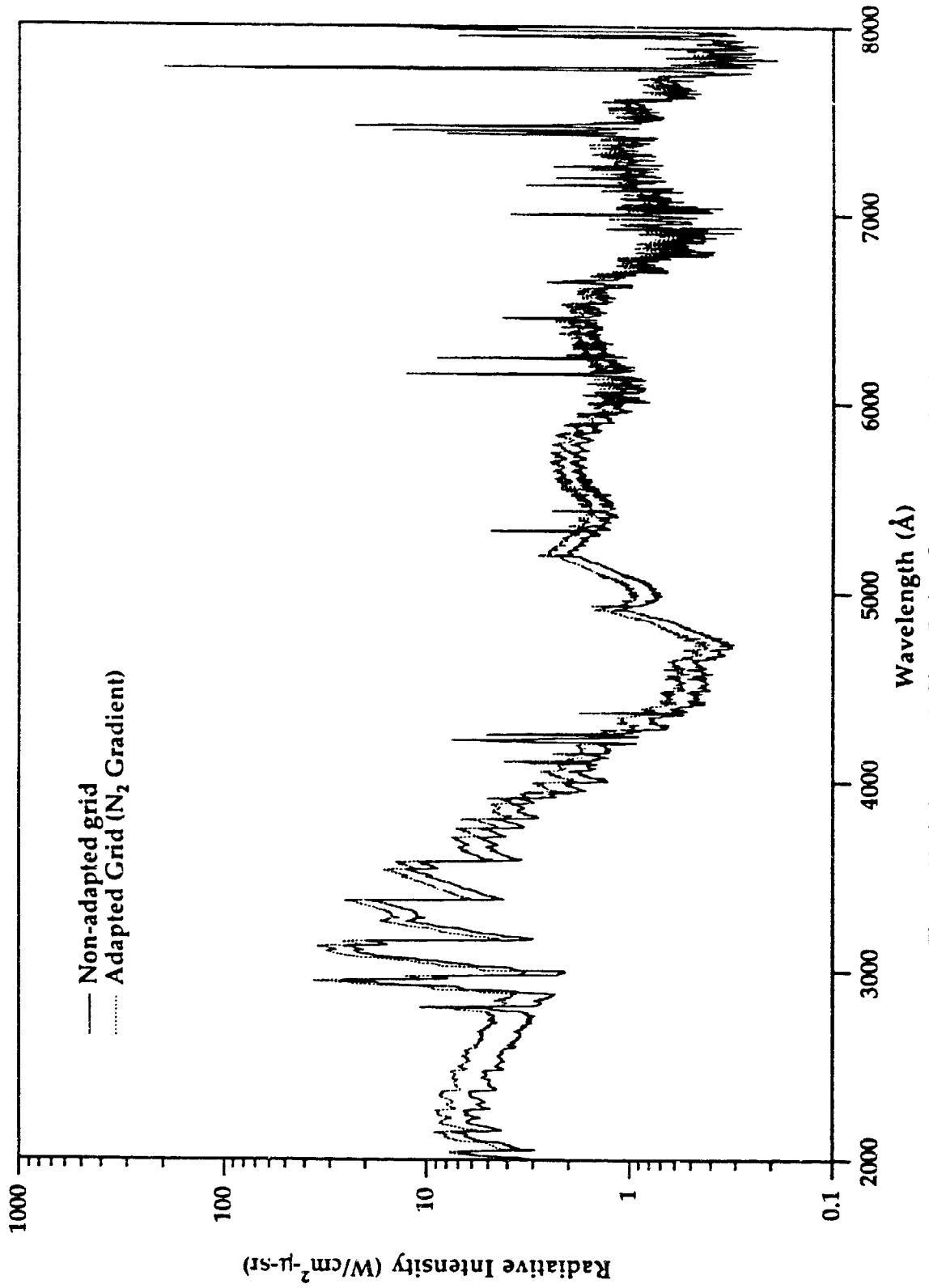
Figure 10. Axisymmetric Blunt Body - Comparison of radiation spectra incident on the wall (stagnation line of sight). The change is ≈ 35% in the UV(2500 Å) region.

COMPUTATION OF NONEQUILIBRIUM VISCOUS FLOWS IN ARC-JET WIND TUNNEL NOZZLES

by

Tahir Gökçen †

Eloret Institute, 3788 Fabian Way, Palo Alto, CA 94303

Arc-jet hypersonic wind tunnels are the means for studying aerodynamic heating and ablation associated with hypersonic flight. In these tunnels a high enthalpy gas produced in the arc chamber, vibrationally excited and dissociated, is expanded through a nozzle into the test section. Analysis of the nozzle flow is necessary for calibration of the wind tunnel flow. Typically these nozzle flows can be characterized as follows: an equilibrium flow in the converging section of the nozzle; a nonequilibrium flow near the throat; and a frozen flow downstream in the diverging section. Therefore, a nonequilibrium formulation is required for the analysis of entire flow. Such a formulation needs to be validated against experimental data in the equilibrium as well as in the nonequilibrium flow regime. The nonequilibrium formulation using Park's two-temperature thermochemical model has produced very satisfactory results in dissociation dominated flows. [1] However, it has not been evaluated in the expanding nozzle flows where recombination and vibrational de-excitation are the dominant nonequilibrium processes.

Objectives of the proposed paper are to present an analysis of two dimensional or axisymmetric arc-heated wind tunnel nozzle flows, and assess the accuracy of the nonequilibrium formulation by comparing the computed flow quantities with existing experimental data. The comprehensive experimental data set of Folk and Smith [2] taken at a direct connect arc-heated wind tunnel nozzle of Air Force Flight Dynamics Laboratory is suitable for this purpose.

In the present formulation, two dimensional/axisymmetric nonequilibrium viscous flows of air are considered. The governing Navier-Stokes equations are augmented with the equations accounting for thermochemical nonequilibrium processes. The equation set consists of fifteen partial differential equations: eleven mass conservation equations for species, two momentum equations for two dimensional flows, and two energy equations. The present nonequilibrium gas model for air consists of eleven chemical species, (N_2, O_2, NO, N, O, N_2^+, O_2^+, NO^+, N^+, O^+, e^-), and the thermal state of the gas is described

---

† Research Scientist, Member AIAA

Mailing Address: NASA Ames Research Center, MS 230-2, Moffett Field, CA 94035

1

by two temperatures: translational-rotational and vibrational-electronic. The chemical reaction rates are prescribed by Park's two-temperature model where the basic dissociation rate is assumed to be governed by the geometric average of translational and vibrational temperatures.[3] The paper will give a more detailed description of the model. The governing equations are discretized using a finite volume approach and the resulting difference equations are solved using an implicit Gauss-Seidel relaxation method. The method is fully implicit for fluid dynamics and thermochemistry and uses flux vector splitting for convective fluxes. Details of the method can be found in Refs. 4-6.

In the proposed paper, evaluation of the nonequilibrium formulation will be made through comparisons of the computed flow quantities at the nozzle exit with the experimental data of Folk and Smith.[2] For a wide range of reservoir conditions, exit surveys and centerline measurements of Pitot pressure, mass flux, stagnation point heat transfer rate, and wall static pressure of a 2-ft-diameter conical nozzle are available. Since the wall pressure and radial mass flux measurements at the nozzle exit cover the nonequilibrium as well as the equilibrium regimes, assessment of nonequilibrium thermochemical models will be possible by comparing the computed results with the experiment. Although the wall pressure and mass flux measurements can be compared directly with computations, comparison of the parameters such as Pitot pressure and stagnation point heat transfer requires a correlation between flow quantities and these parameters. This will be achieved by computational simulation of the flow at the stagnation point of a sphere (or the probe itself) or by using expressions such as the one by Fay and Riddell.[7] The computed total enthalpy profiles will be compared with the experiment using the stagnation point heat transfer data. These comparisons are needed for the calibration of arc-jet nozzle flows.

As a representative case, an axisymmetric nonequilibrium flow in a converging-diverging conical nozzle is computed. The initial conditions at the nozzle entrance are specified as air at temperature of $T_0 = T_{v0} = 5000\,°K$ and pressure of $p_0 = 35\,atm$. The exit pressure is specified such that shockless supersonic flow is sustained in the diverging section of the nozzle. The nozzle wall is assumed to be at a constant temperature of $T_w = 500\,°K$ and non-catalytic to recombination. The nozzle has conical angles of 30° for converging and 16° for diverging section, and its entrance, throat and exit diameters are 20, 2.54, and 63.5 cm, respectively. This particular geometry is taken from Ref. 2. Figure 1 depicts the nozzle geometry and computational grid. For the reservoir conditions chosen, the flow remains in thermochemical equilibrium in converging section and goes through a nonequilibrium expansion downstream of the nozzle throat. Recombination and vibrational de-excitation of air are principal nonequilibrium processes in the nozzle expansion. Figures 2 and 3 show the flowfield contours of atomic oxygen and vibrational-electronic temperature. In Fig. 2, recombination of oxygen downstream of the throat and in the viscous boundary layer is clearly observed. Also it is interesting to note that in Fig. 3, the vibrational temperature rise in the diverging section of the nozzle after dropping near the

2

throat. This is mainly due to atomic recombination. In Fig. 4, variation of the computed temperatures along the nozzle centerline is presented. Figure 5 shows radial variation of computed temperature profiles at the nozzle exit where the temperatures are normalized by corresponding centerline values.

Since the computed results are preliminary, no comparisons with experimental data is presented. The proposed paper will make detailed comparisons and assess the accuracy of thermochemical nonequilibrium models.

References

[1] Park, C., *Nonequilibrium Hypersonic Aerothermodynamics*, John Wiley and Sons, Inc., New York, 1989.

[2] Folck, J. L. and Smith, R. T., "Hypersonic Flow Diagnostic Studies in a Large Arc-Heated Wind Tunnel," *AIAA Journal*, Vol. 8, No. 8, 1970, pp. 1470-1476.

[3] Park, C., Howe, T. H., Jaffe, L. R., and Candler, G. V., "Chemical-Kinetic Problems of Future NASA Missions," *AIAA paper 91-0464*, 1991.

[4] MacCormack, R. W., "Current Status of the Numerical Solutions of the Navier-Stokes Equations," *AIAA paper 85-0032*, 1985.

[5] Candler, G.V., "The Computation of Weakly Ionized Hypersonic Flows in Thermo-Chemical Nonequilibrium," *Ph. D. Thesis*, Stanford University, 1988.

[6] Gökçen, T., "Computation of Hypersonic Low Density Flows with Thermochemical Nonequilibrium," *Ph. D Thesis*, Stanford University, 1989.

[7] Fay, J. A. and Riddell, F. R., "Theory of Stagnation Point Heat Transfer in Dissociated Air," *Journal of the Aerospace Sciences*, Vol. 25, No. 2, 1958, pp 73-85.
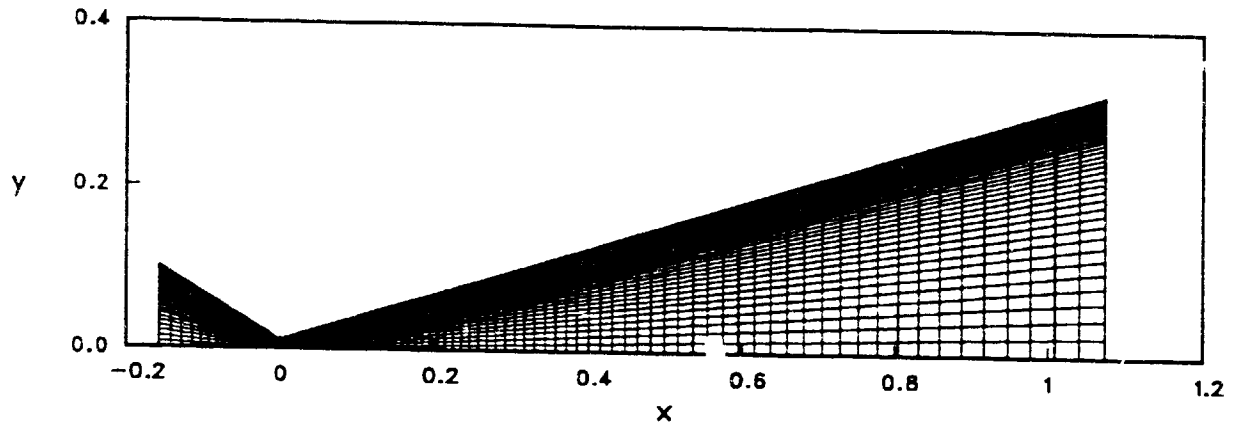
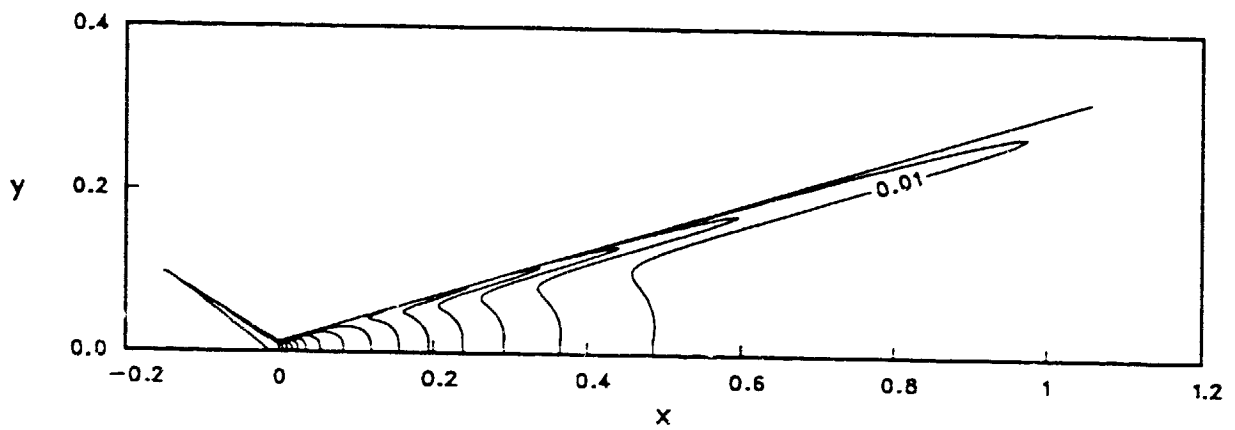**Fig. 1.** Nozzle geometry and computational grid (100 × 50).

Fig. 2. Computed flowfield contours of atomic oxygen mass fraction.
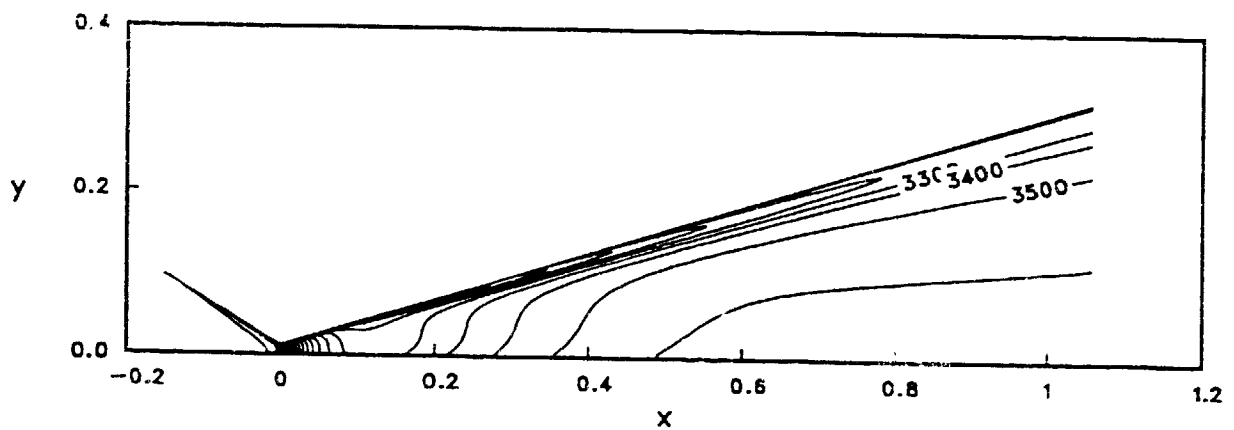

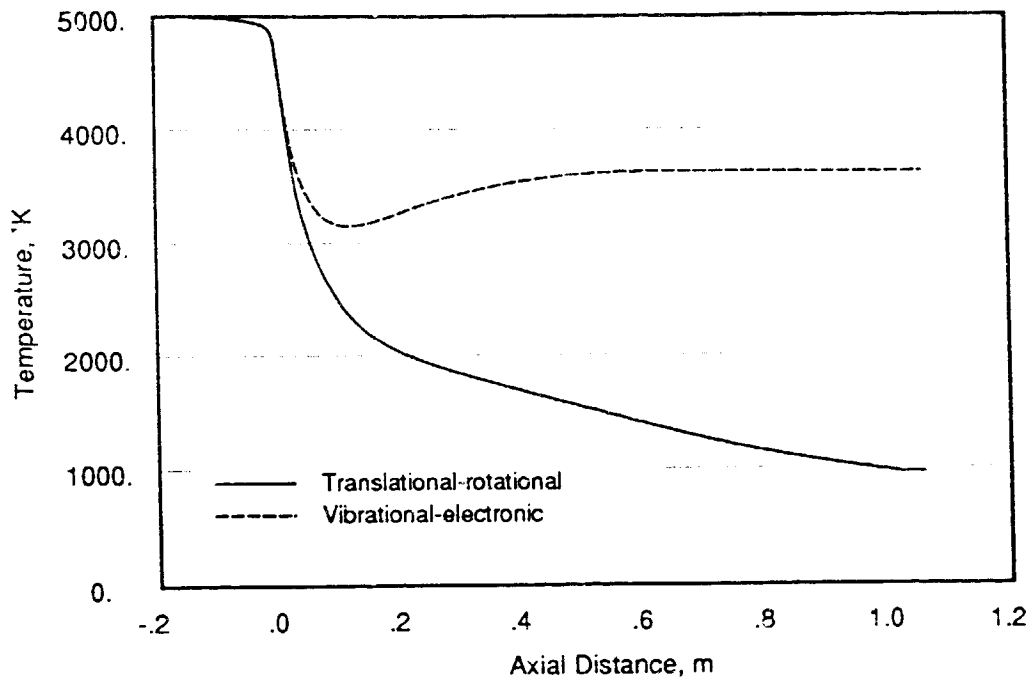**Fig. 3.** Computed flowfield contours of vibrational-electronic temperature.

4

Fig. 4. Variation of computed temperatures along the nozzle centerline.
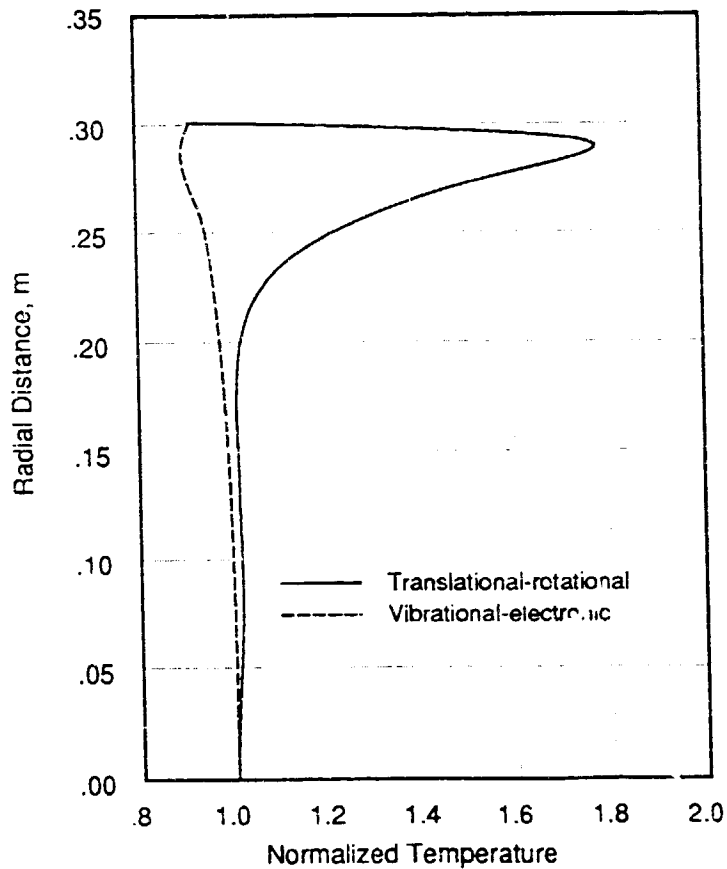

Fig. 5. Computed temperature profiles at the exit: normalized by the centerline values.
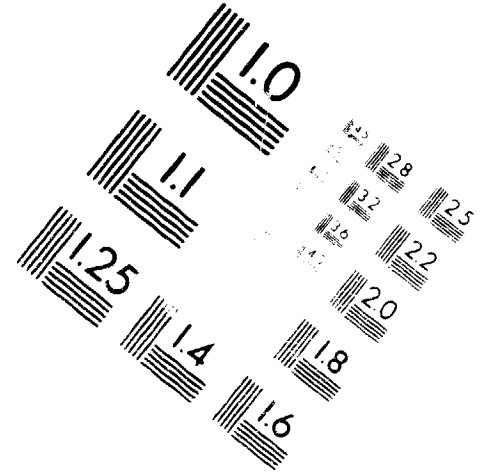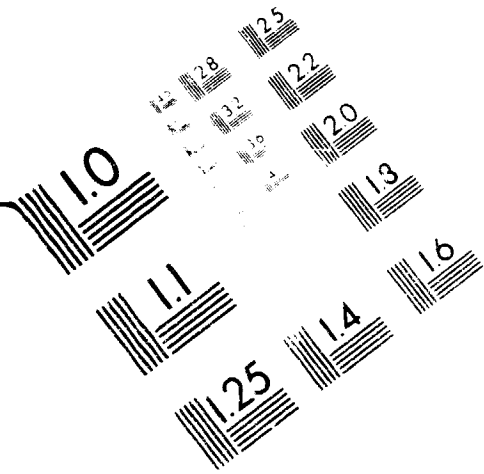
END

DATE

FILMED

AUG 10 1994

Centimeter

1 2 3 4 5 6 7 8 9 10 11 12 13 14 15 mm

Inches

1.0

1.1

1.25 1.4 1.6

2.8 2.5

3.2 2.2

3.6

4.0 2.0

1.8
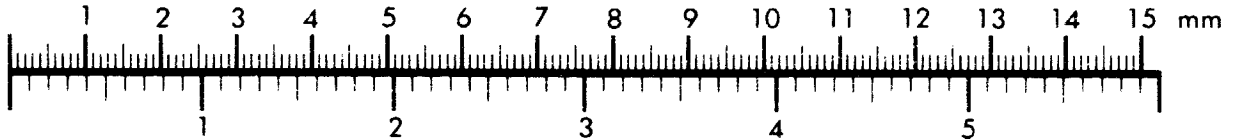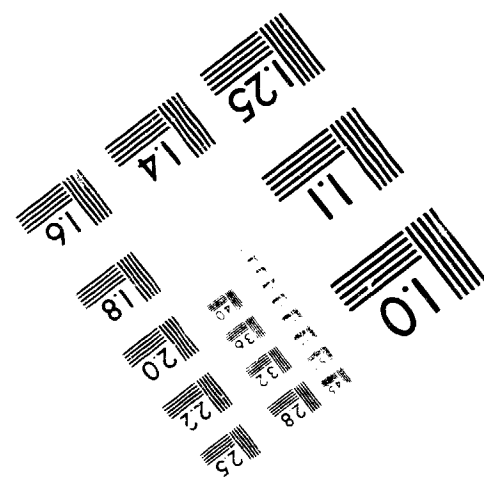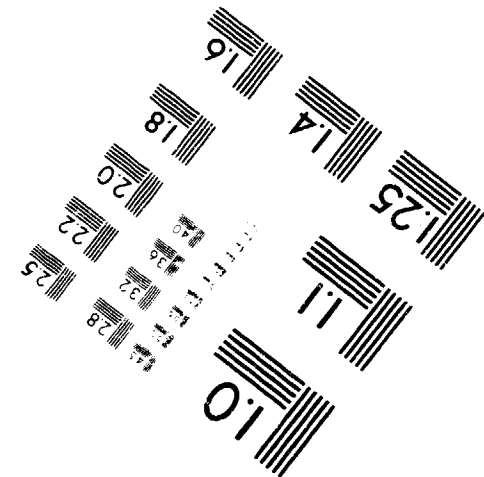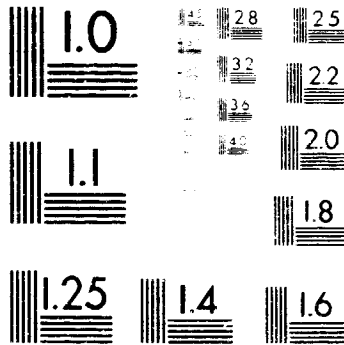
MANUFACTURED TO AIIM STANDARDS
BY APPLIED IMAGE, INC.